

AALBORG UNIVERSITY

THERMAL ENERGY AND PROCESS ENGINEERING

DEPARTMENT OF ENERGY TECHNOLOGY

GROUP: TEPE4-901

**A Generic Gas Radiative Model
Applicable to CFD Simulations of all
Combustion Processes**

Authors:

Sergio Sanchez ROMERO

Shashank SINGH

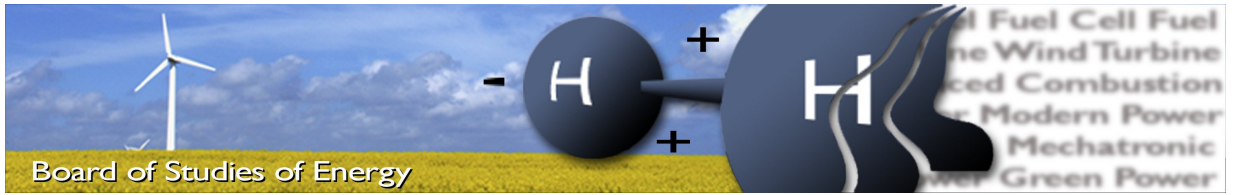
Supervisor:

Chungen YIN

May 2016



AALBORG UNIVERSITY
STUDENT REPORT



Title: A Generic Gas Radiative Property Model Applicable to CFD Simulations
Semester: 9-10 th
Project period: 01.09.2015 to 25.05.2016
ECTS: 50
Supervisor: Chungen Yin
Project group: TEPE4-901

Sergio Sanchez Romero

Shashank Singh

SYNOPSIS:

This report is about the work done in developing and demonstrating the applicability of a generic gas radiative property model for all CFD simulations. A computationally Efficient Exponential Wide Band Model (E-EWBM) has been developed in C++ to calculate emissivity for gas mixtures. The code has been well validated. CFD simulations in Fluent have been performed for air-fuel and oxy-fuel conditions. In air-fuel conditions, the effect of radiative property models has been studied along with the effect of reaction mechanisms. The E-EWBM has significant effect on the absorption coefficient. For temperature, axial velocity and species the model has little impact. Remarkable effect of reaction mechanisms has been found. A 3D mesh has been created in ICEM CFD for oxy-fuel simulations. Effect on the absorption coefficient is quite remarkable.

Pages, total: 130

Appendix: 51

By signing this document, each member of the group confirms that all group members have participated in the project work, and thereby all members are collectively liable for the contents of the report. Furthermore, all group members confirm that the report does not include plagiarism.

Preface

The work described in this report was carried out during the 9-10th semesters of Master's studies at Aalborg University, Department of Energy Technology. The project group (TEPE4-901) follows the programme "Thermal Energy and Process Engineering", whereas the project title is "A generic gas radiative property model applicable to CFD simulations of all combustion processes".

The generic gas radiative property model was developed using the computer language C++. In order to demonstrate its applicability in air-fuel and oxy-fuel combustion CFD, 12 simulations were run in Fluent V15.

The report itself consists of five chapters and supplementing appendices:

- Introduction: a brief introduction to why gas radiation property model is of interest, the background of the weighted-sum-of gray-gas-model, the background of the EWBM and work done in this thesis are discussed.
- The computationally efficient Exponential Wide Band Model (E-EWBM): the formulation of the E-EWBM is explained along with its validation. Other gas radiative property models used in this thesis for comparison are also described.
- Implementation and impact of the E-EWBM in air-fuel combustion CFD: furnace, operational conditions, different models, effect of mesh, effect of four different radiation models and four different global reaction mechanisms are discussed.
- Implementation and impact of the E-EWBM in oxy-fuel combustion CFD: furnace, operational conditions, in-flame measurement, 3D-meshing and effect of two radiation models have been discussed.
- Conclusion and future work: discussion about the project output and future work prospects.

Contents

Contents	ii
List of Figures	v
List of Tables	vii
Abbreviations	ix
Symbols	x
1 Introduction	1
1.1 Why is gas radiation property model of interest?	1
1.2 The background of weighted-sum-of-gray-gas-model	2
1.3 The background of the EWBM	3
1.4 Work done in this thesis	4
2 The computationally efficient Exponential Wide Band Model: formulation and verification	6
2.1 Introduction	6
2.2 Fundamental characteristics of gas thermal radiation	6
2.3 Exponential Wide Band Model (EWBM)	7
2.4 The computationally Efficient Exponential Wide Band Model (E-EWBM) formulated in this thesis	9
2.4.1 E-EWBM C++ code: validation with IFRF example	20
2.5 Other gas radiative property models used for comparison in this thesis	22
2.5.1 Smith et al. (1982) air-fuel WSGGM	22
2.5.2 Yin (2013) air-fuel WSGGM	23
2.5.3 Yan et al. (2015) E-EWBM	24
2.6 Emissivity as a function of temperature and beam length: Comparison of the 4 models	25
2.7 Conclusion	27
3 Implementation and impact of the E-EWBM in air-fuel combustion CFD	28
3.1 Furnace	28
3.1.1 Geometry	29
3.1.2 Fuel and air composition	29
3.1.3 Boundary conditions	30
3.1.4 Experimental data available	32

3.2	Computational cases: an overview	32
3.3	Turbulence modelling	33
3.3.1	Realizable k- ϵ model	34
3.3.2	Near wall modelling	35
3.4	Radiative heat transfer modelling	36
3.4.1	RTE and DO model	36
3.4.2	The four gas radiative property models used and compared	36
3.5	Reaction modelling	37
3.5.1	Species modelling	37
3.5.2	The four global combustion mechanisms used and compared	38
3.5.3	Turbulence-chemistry interaction modelling	40
3.6	Properties and solution methods/control	41
3.6.1	Material properties	41
3.6.2	Solution methods	42
3.6.3	Solution controls	43
3.7	Results and discussion	43
3.7.1	Effect of mesh	44
3.7.2	Effect of gas radiative property models	46
3.7.3	Effect of global combustion mechanisms	53
3.8	Conclusion	57
4	Implementation and impact of the E-EWBM in oxy-fuel combustion CFD	59
4.1	Furnace	59
4.1.1	Geometry	60
4.1.2	Oxygen and fuel composition	61
4.1.3	Boundary conditions	62
4.1.4	In-flame measurement	64
4.2	Mesh for the OXYFLAME furnace	65
4.2.1	Mesh quality	65
4.3	Computational cases: an overview	67
4.4	Reaction mechanism	68
4.5	Properties and solution methods/control	68
4.5.1	Material properties	68
4.5.2	Solution method	69
4.6	Effect of radiation property models: results and discussion	70
4.7	Conclusion	74
5	Conclusion and future work	75
5.1	Conclusion	75
5.2	Future work	76
A	Appendix: WSGGM coefficients for emissivity	78
B	Appendix: Look up table for polynomial coefficients for E-EWBM Yan et al. (2015)	80

C Appendix: Exponential wide band parameters	85
D Appendix: C++ Source code for E-EWBM	87
Bibliography	129

List of Figures

2.1	Low resolution spectrum of absorption band for CO ₂ at 830 K, 10 atm and for path length through gas of 0.388 m [1]	7
2.2	Band Shapes for Exponential Wide Band [1]	8
2.3	Gray treatment of CO ₂ -4.3μm [1]	17
2.4	Treatment of Bands overlapping in EWBM [2]	18
2.5	Result obtained from C++	21
2.6	Emissivity as a function of temperature and beam length at condition $P_w/P_c=2$ ($P_c=0.1$ atm) and $x_{H_2O}=0.2$, $x_{CO_2}=0.1$, $x_{CO}=0.0$ and $x_{CH_4}=0.0$	25
2.7	Emissivity as a function of temperature and beam length at condition $P_w/P_c=2$ ($P_c=0.1$ atm) and $x_{H_2O}=0.2$, $x_{CO_2}=0.1$, $x_{CO}=0.020$ and $x_{CH_4}=0.005$	26
3.1	To the left is a 2D axi-symmetric furnace for air-fuel combustion and to the right is the close-up view of the burner	29
3.2	Boundaries used of furnace for air-fuel case	30
3.3	Axial and swirl velocity profile of the air stream at the inlet	31
3.4	Temperature and axial velocity vs radial position at 27 mm from the quarl exit	45
3.5	O ₂ mass fraction vs radial position at 27 mm from the quarl exit	45
3.6	Radial distribution profiles of absorption coefficient to study the effect of radiation models	48
3.7	Radial distribution profiles of radiation source term	49
3.8	Contour of gas temperature using the developed E-EWBM	49
3.9	Radial distribution profiles of temperature to study the effect of radiation models	50
3.10	Radial distribution profiles of axial velocity to study the effect of radiation models	51
3.11	Radial distribution profiles of O ₂ mass fraction to study the effect of radiation models	52
3.12	Radial distribution profiles of temperature to study the effect of reaction mechanisms	54
3.13	Radial distribution profiles of axial velocity to study the effect of reaction mechanisms	55
3.14	Radial distribution profiles of O ₂ mass fraction to study the effect of reaction mechanisms	56
3.15	Radial distribution profiles of the net production rate of CO ₂	57

4.1	Cross section diagram of the OXYFLAME furnace reproduced from Bollettini et al. (1997) [3]	60
4.2	Diagram of the high-momentum jet burner, Burner A [3]	61
4.3	The full oxy-NG furnace used in simulation	62
4.4	A close view of burner of 0.8 MW furnace	66
4.5	Radial distribution profiles of absorption coefficient in oxy-fuel combustion	70
4.6	Radial distribution profiles of temperature in oxy-fuel combustion	71
4.7	Radial distribution profiles of axial velocity in oxy-fuel combustion	72
4.8	Radial distribution profiles of O ₂ volume fraction in oxy-fuel combustion .	73
4.9	Radial distribution profiles of CO ₂ volume fraction in oxy-fuel combustion	74

List of Tables

2.1	Look up table for $\alpha(T)$ (*) The 2.7 μm H_2O consists of three overlapping bands	13
2.2	Fitting coefficients a_k for $\beta(T)$	15
2.3	Table for Exponential Wide Band correlation for an isothermal gas	16
2.4	Table for coefficient a_i , b_i and c_i	17
2.5	Emissivity data base generated for partial pressure of CO_2 and H_2O vapor in Smith et al. (1982) WSGGM [4]	22
2.6	Emissivity data base generated for partial pressure of CO_2 and H_2O vapor in Yin (2013) WSGGM [4]	23
3.1	Air composition used in air-fuel case [5]	30
3.2	Fuel composition used in air-fuel case [5]	30
3.3	Boundary conditions for the fuel and air inlets [6]	31
3.4	Boundary conditions for outlet in air-fuel case [6]	31
3.5	Boundary conditions for walls [6]	32
3.6	Coefficients of the temperature profile along the furnace cylinder wall in the hot wall configuration [5]	32
3.7	Overview of the main models used in the air-fuel simulations	33
3.8	1-step reaction mechanism for CH_4	38
3.9	Original WD 2-step reaction mechanism for CH_4 [1]	38
3.10	Original JL 4-step reaction mechanism for CH_4 [1]	39
3.11	JL-1 4-step reaction mechanism for CH_4 [1]	40
3.12	JL-Refined (Yan et al., 2015) 4-step reaction mechanism for CH_4 [7]	40
3.13	Material properties used in all air-fuel CFD simulations [6]	42
3.14	Relaxation factors employed in simulation for air-fuel simulations [6]	43
3.15	Quality parameters of the meshes N, 4N and 16N for 2D-axisymmetric furnace	44
3.16	Convergence summary for the effect of mesh	45
3.17	Convergence summary for the effect of gas radiative property models	47
3.18	Comparison of radiation heat transfer rate with different radiation models	47
3.19	Comparison of peak temperature with different radiation models	50
3.20	Convergence summary for the effect of reaction mechanisms	53
3.21	Comparison of peak temperature with different reaction mechanisms	54
4.1	Dimensions of the 0.8 MW furnace [3]	61
4.2	Dimension of high-momentum jet burner, Burner A [3]	61
4.3	Oxygen composition used in oxy-fuel case [1]	61
4.4	Fuel composition used in oxy-fuel case [1]	62

4.5	Boundary conditions for inlet fuel and oxygen for oxy-fuel case [3]	63
4.6	Boundary conditions for outlet for oxy-fuel case [3]	63
4.7	Boundary conditions for walls for oxy-fuel case [3]	63
4.8	Quality parameters of the mesh for oxy-fuel furnace	67
4.9	Refined WD 2-step reaction mechanism for CH ₄ under oxy-fuel combustion [1]	68
4.10	Material properties used in all oxy-fuel CFD simulations	68
4.11	Relaxation factors employed in simulation for oxy-fuel simulations	69
4.12	Computational time of the WSGGM and E-EWBM in the oxy-fuel case	74
A.1	WSGGM coefficients for emissivity for Smith et al. (1982) WSGGM [1]	78
A.2	WSGGM coefficients for emissivity for Yin (2013) refined WSGGM [4]	79
B.1	Polynomial coefficients $\alpha_{ij}(T)$ for temperature range of 300-500 [K] [7]	81
B.2	Polynomial coefficients $\beta_{ij}(T)$ for temperature range of 300-500 [K] [7]	81
B.3	Polynomial coefficients for $\alpha_{ij}(T)$ for temperature range 500-2000 [K] [7]	82
B.4	Polynomial coefficients for $\beta_{ij}(T)$ for temperature range of 500-2000 [K] [7]	83
B.5	Polynomial coefficients $\alpha_{ij}(T)$ for temperature range of 2000-2500 [K] [7]	84
B.6	Polynomial coefficients $\beta_{ij}(T)$ for temperature range of 2000-2500 [K] [7]	84
C.1	Exponential wide band parameters [1]	86

Abbreviations

AAU	A alborg U niversity
CFD	C omputational F luid D ynamics
DO	D iscrete O rdinates
ED	E ddy D issipation
EDC	E ddy D issipation C oncept
E-EWBM	E fficient- E xponential W ide B and M odel
EWBM	E xponential W ide B and M odel
EWT	E nhanced W all T reatment
HITEMP	H igh T emperature Molecular Spectroscopic Database
HITRAN	H igh-Resolution T ransmission Molecular Absorption Database
ICEM	I ntegrated C omputer E ngineering M anufacturing
IFRF	I nternational F lame R esearch F oundation
JL	J ones and L indtedt (1988)
LBL	L ine B y L ine
RANS	R eynolds- A veraged N avier S tokes
RNG k-ϵ model	R e- N ormalisation G roup k - ϵ model
RTE	R adiative T ransfer E quation
WD	W estbrook and D ryer (1981)
WSGGM	W eighted S um of G ray G as M odel

Symbols

Alphabetical symbols

A_{ij}	Total band absorptance	$[cm^{-1}]$
a_k	Fitting coefficient for $\beta_{ij}(T)$	-
$a_{\epsilon,i}(T_g)$	Weighting factors	-
B	$B = \beta_{ij} \cdot P_{e,ij}$	-
b_{ij}	Self-broadening coefficient	-
b_n	Polynomial coefficient	-
$b_{\epsilon,i,j}$	Gas temperature polynomial coefficient	-
C_2	Planck radiation constant, $C_2 \equiv \frac{hc}{k_B} = 1.438786 \cdot 10^{-2}$	$[m \cdot K]$
c_0	Speed of light, $c_0 = 299792458$	$[m/s]$
c_p	Specific heat	$[J/kg \cdot K]$
$c_{p,i}$	Specific heat of species i	$[J/kg \cdot K]$
C_μ	Dimensionless number	-
Da	Damkohler number	-
$D_{i,m}$	Mass diffusion coefficient	$[m^2/s]$
$D_{T,i}$	Thermal diffusion coefficient	$[m^2/s \cdot K]$
d	Line spacing between two consecutive absorption lines	$[cm^{-1}]$
$F(x)$	Fractional function of blackbody radiation	-
G_b	Generation of turbulent kinetic energy due to buoyancy	$[m^2/s^2]$
G_k	Generation of turbulent kinetic energy due to velocity gradient	$[m^2/s^2]$
$G(\vec{r}')$	Incident radiation	$[kW/m^2]$
g_k	Degeneracy of the fundamental band	-
h	Planck's constant, $h = 6.626176 \cdot 10^{-34}$	$[J \cdot s]$
I	Total radiation intensity	$[W/m^2 \cdot sr]$

\vec{J}_i	Diffusion flux	$[m^2/s]$
k	Turbulent kinetic energy	$[m^2/s^2]$
k_a	Effective absorption coefficient	$[m^{-1}]$
$k_a(\vec{r})$	Absorption coefficient	$[m^{-1}]$
k_i	Pressure absorption coefficient	$[atm^{-1} \cdot m^{-1}]$
$k(T)$	Reaction rate coefficient	-
L	Path length	[m]
M_i	Molar weight of gas i	[g/mol]
n	Refractive index	-
n_{ij}	Fitting parameter	-
P	Sum of partial pressure of participating gases	[atm]
P_0	Reference pressure	[atm]
P_c	Partial pressure of CO ₂	[atm]
$P_{e,ij}$	Dimensionless equivalent broadening pressure for species i	-
P_t	Total gas pressure of the gas	[atm]
P_w	Partial pressure of water vapor	[atm]
\vec{q}	Radiation heat source	$[kW/m^3]$
R_u	Universal gas constant, $R_u = 8.3144$	$[J/(mol \cdot K)]$
\vec{r}, \hat{s}	Position vector, direction vector	-
S_{ct}	Turbulent Schmidt number	-
$(S/d)_{i,j}$	Mean line intensity to line spacing ratio	-
S_{ij}	Mean strain rate tensor	$[s^{-1}]$
S_k, S_ϵ	User defined source term	-
s_k	$s_k = \frac{1}{1 - \exp^{-u_k}}$	-
T	Total gas temperature	[K]
T_0	Reference temperature	[K]
T_g	Gas temperature	[K]
T_{ref}	Reference temperature of gas	[K]
\vec{u}	Velocity vector	$[m/s]$
u_k	$u_k \equiv \frac{hc_0 \eta_k}{k_B T}$	-
x_i	Molar fraction of gas i	[-]
Y_i	Piece wise polynomial coefficient	-
Y_M	Dissipation rate	$[m^2/s^3]$

Greek symbols

$\alpha_{0ij}(T)$	Reference band intensity	$[cm^{-1}/(g \cdot m^{-2})]$
$\alpha_{ij}(T)$	Integrated band intensity	$[cm^{-1}/(g \cdot m^{-2})]$
$\alpha_{\eta ij}$	Spectral absorptivity	$[cm^{-1}/(g \cdot m^{-2})]$
$\beta_{0ij}(T)$	Reference mean line width to spacing ratio	-
$\beta_{ij}(T)$	Mean line width to spacing ratio	-
γ	Width of a line at half of its maximum intensity level	$[cm^{-1}]$
γ_E	Line half width for rotational band of H ₂ O	$[cm^{-1}]$
$\Delta \eta_{ij}$	Width of each band	$[cm^{-1}]$
δ_k	Vibrational transition quantum step	-
ϵ	Emissivity	-
ϵ	Turbulent energy dissipation rate	$[m^2/s^3]$
$\epsilon_{b\lambda}$	Planck's constant distribution of emissive power	-
η_C	Band wave-number centre	$[cm^{-1}]$
η_k	Fundamental band	$[cm^{-1}]$
$\eta_{L,ij}, \eta_{U,ij}$	Lower and upper band limit of species i and band j	$[cm^{-1}]$
η_U	Dimension less parameter	-
λ	Characteristic band wavelength	$[\mu m]$
μ_t	Turbulent viscosity	$[kg/m \cdot s]$
ν	Kinematic viscosity	$[m^2/s]$
ν_k	Vibrational quantum number of band	-
χ_i	Mass path length	$[g/m]$
π	$\pi = 3.1416$	-
ρ_i	Density of gas i	$[g/m^3]$
$-\overline{\rho u'_i u'_j}$	Reynolds shear stress	$[N/m^2]$
$\sigma_k, \sigma_\epsilon$	Turbulent Prandtl numbers for k- ϵ	-
σ_s	Scattering coefficient	$[m^{-1}]$
τ_{gij}	Mean band transmissivity	-
τ_H	Optical depth at band head	-
$\tau_{\Delta\eta,k}$	Spectral block transmissivity	-
ϕ	Line-width to spacing ratio temperature variation parameter	-

ψ	Band-intensity temperature variation parameter	-
$\omega_{0ij}(T)$	Reference band width parameter	$[cm^{-1}]$

Chapter 1

Introduction

1.1 Why is gas radiation property model of interest?

Radiative heat transfer rates are generally proportional to temperature in the fourth power. Therefore, radiative heat transfer becomes increasingly important with rising temperature levels and is the principal mode of heat transfer in high temperature environments (e.g., utility boiler furnaces). Models for radiative properties play a key role in reliable Computational Fluid Dynamics (CFD) simulations of utility boilers and simulation-based boiler design and optimization [4]. The advantages of using such radiative property models in CFD are multiple. For instance, they can serve to investigate the effects of burner design modifications on radiative heat transfer in a much faster and economical way than experiments would do [2].

Much of the current work on the modelling of industrial flames using CFD codes still applies the sum of gray gases models or polynomial approximations to predict the total radiative properties of absorbing gaseous phase [2]. The success encountered by these models in their mathematical modelling of flames is greatly attributed to their mathematical simplicity and their ability to simulate reasonably well the non-grayness of gases in a range of temperature and partial pressure that usually covers most furnace applications. However, in recent years the industry has shown an increasing interest for high pressure combustion systems, either for thermodynamic reasons (e.g., gas turbines), combustion process intensification (e.g., pressurized fluidized beds) and oxy-fuel combustion, in which the concentration of participating gases is significantly higher than that

in traditional air-fuel combustion processes. The radiative property models presently used in most CFD codes are limited to the total emissivity and absorptivity calculations at atmospheric pressure and at low participating gases concentration will have to be replaced by more general models [2].

Major combustion products, such as carbon dioxide and water vapor, are found to be significant emitters and absorbers of radiant energy. For oxy-fuel combustion, gas radiative property models have gained a lot of concern, due to the much higher concentrations of participating gases such as carbon dioxide and water vapor in oxy-fuel conditions. Predicting the radiative properties of participating gases constitutes a new challenge in calculating radiative heat transfer. The solution to the radiative property model requires the knowledge of the temperature distribution, as well as the concentration of the different species present in the medium. Since the temperature and species concentration distribution come from application of conservation of mass and energy principles, the solution procedure is iterative and computationally intensive. From the application point of view of radiative property models, the total emissivity and effective absorption coefficient are usually concerned [8].

1.2 The background of weighted-sum-of-gray-gas-model

Weighted-sum-gray-gases-model (WSGGM) is very efficient in computation of radiative heat transfer and generates acceptable errors for the range of temperature and pressure that covers almost all combustion and gasification process.

Some efforts have been made recently to develop WSGGMs applicable to oxy-fuel conditions, using more accurate but computationally expensive models as the reference. For instance, Yin (2011) developed a refined WSGGM for oxy-fuel conditions and performed a numerical study of the impacts of radiation and chemistry in oxy-fuel flames [1]. Kangwanpongpan et al. (2012) proposed another enhanced WSGGM based on the HITEMP-2010 spectral database for oxy-fuel combustion and validated their model with the Line by Line method [9]. Further, a refined air-fuel WSGGM has been developed by Yin (2013) and remarkable difference between the refined model and the most widely used air-fuel WSGGM in CFD of a utility boiler was observed [4].

Although WSGGM represents a good compromise between computational efficiency and accuracy and is most widely used in combustion CFD, it still has a few drawbacks in practical applications, e.g.:

- This model cannot adjust to accommodate the different combustion environments naturally. For instance, the Smith et al. (1982) air-fuel WSGGM has been widely used in combustion simulations. However, the implementation of air-fuel WSGGM in oxy-fuel combustion results in error. This is due to the fact that the Smith et al. WSGGM is only adequate for low CO₂ and H₂O concentrations. The higher concentrations of CO₂ and H₂O in oxy-fuel combustion furnaces lead to a higher gas emissivity.

Some efforts have been made to develop WSGGM applicable to oxy-fuel combustion CFD, such as those mentioned above. Current scenario is one has to pick different WSGGM (oxy-fuel or air-fuel WSGGM) for oxy-fuel and air-fuel combustion, in order to get acceptable and reliable result [1].

- All the existing WSGGMs only account for two species, i.e., CO₂ and H₂O, while other participating gases (e.g., CH₄ and CO) which could be important under some scenarios cannot be easily included in WSGGMs [1].
- In a flame it is difficult for WSGGMs to account for the variations in H₂O to CO₂ molar ratio in an accurate way. WSGGMs employ parameter tables for different H₂O to CO₂ molar ratio. These parameter tables are discrete in nature and induce discontinuities in the calculation of absorption coefficient. However, few authors have addressed to this problem by replacing the discrete parameter table with smooth coefficient functions of H₂O to CO₂ molar ratio, but still these WSGGMs are only applicable to oxy-fuel combustion [1].

1.3 The background of the EWBM

The Exponential Wide Band Model (EWBM) can easily address and solve all the above problems in a natural way while distinguishing oxy-fuel from air-fuel combustion, and can accurately account for variation in gas composition such as CO₂, H₂O, CO, CH₄, SO₂, NO, C₂H₂, NH₃ and N₂O and produces fairly good result. The EWBM is computationally faster than Line by Line method and Narrow Band Model. The model utilizes

simple mathematical expressions to predict pressure and temperature dependency of the most important absorption bands of H_2O , CO_2 , CH_4 and CO . The homogeneous gas emissivity can be computed by summing up the band emissivity times the fraction of blackbody radiation in the band interval over all bands and species [2].

Initially, the EWBM developed by Edwards and co-workers (1964) is based on a physical analysis of gas absorption [2]. They used a set of semi empirical expressions to predict the total band absorptance of infrared active molecules.

Yan et al. (2015) tried to develop a computationally efficient EWBM model which is applicable to combustion CFD and takes into account absorption bands of H_2O , CH_4 , CO_2 and CO [7]. The model is computationally efficient, but one limitation of the model is its applicability only up to certain temperature range.

Yin (2011) tried once to develop the original EWBM applicable to both air-fuel and oxy-fuel combustion but the main disadvantage of this model is its computational inefficiency if compare with WSGGM [1]. The EWBM model is not really computationally applicable to CFD simulation for real combustion systems. Thus, it is necessary to develop a computationally efficient EWBM which is applicable to CFD combustion and maintain the accuracy of the original EWBM to calculate the emissivity of any gas mixture at any condition.

1.4 Work done in this thesis

In this work an effort has been made on developing a new generic E-EWBM, using computer language C++. The computer code is validated by calculating the emissivity of a given flue gas and comparison is made with results available from literature. This new generic E-EWBM model is applicable to both air-fuel and oxy-fuel combustion. It can naturally account for the contribution of participating gases such as CO_2 , H_2O , CO , CH_4 , SO_2 , NO , C_2H_2 , NH_3 and N_2O and the variations in the concentrations of these species, as well as different pressures other than the atmospheric pressure. Readers are advised that the E-EWBM model differs from the EWBM developed by Yin (2011) in three aspects:

1. The calculation of the integrated band intensity, $\alpha_{ij}(T)$ [$cm^{-1}/(g \cdot m^{-2})$], which physically represents the area under the mean absorption coefficient curve.
2. The calculation of the mean line width to spacing ratio parameter $\beta_{ij}(T)$.
3. The calculation of the fractional function of black body radiation $F(x)$.

In the EWBM, the two parameters in 1 and 2 are calculated based on the quantum mechanics and the parameter in 3 is iteratively solved, which is quite time consuming. The E-EWBM relies more on polynomial correlations and look-up table, which greatly speed up the calculation [2].

The E-EWBM is reformulated to C code because this language is compatible with the user defined function (UDF) in ANSYS Fluent.

Numerical simulations have been performed in air-fuel and oxy-fuel combustion conditions, with the aim to demonstrate the applicability of the generic E-EWBM. While performing advanced CFD simulations of the natural gas fired furnace key issues such as mesh independency, turbulence and combustion mechanisms have also been addressed. The simulation results based on the new E-EWBM have been compared with the results of other radiation models, as well as the experimental data available in literature.

Chapter 2

The computationally efficient Exponential Wide Band Model: formulation and verification

2.1 Introduction

This chapter is mainly about the formulation and verification of the generic gas radiative property model. A computer C++ code is developed to evaluate the emissivity of any gas mixture at any condition by using the Efficient-Exponential Wide Band Model (E-EWBM) and the calculation is validated with a reference in literature. Other gaseous radiative property models are also briefly summarized and the emissivity plots calculated by the different models are compared.

2.2 Fundamental characteristics of gas thermal radiation

Absorption by molecular gases is mainly concentrated within four or five strong absorption bands located in the near-infrared and infrared region (1-20 μm in the wavelength). For example, Figure 2.1 shows the low-resolution spectrum of the absorption bands for CO_2 under a certain condition. Such absorption bands are result of the superposition of a very large number of overlapped absorption lines [1].

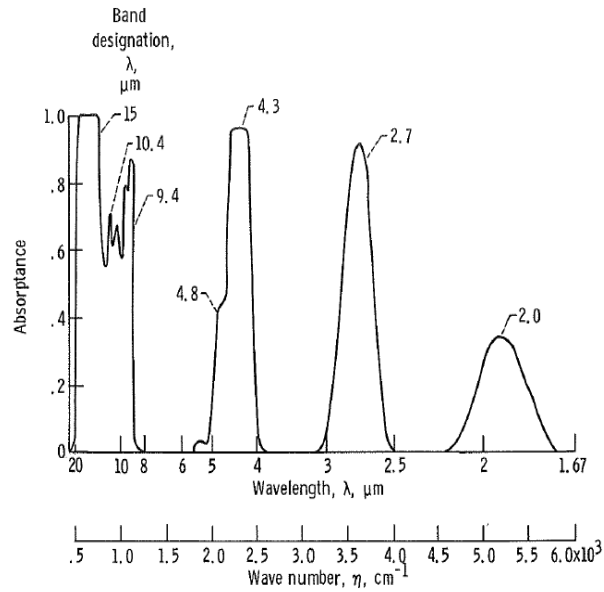


FIGURE 2.1: Low resolution spectrum of absorption band for CO₂ at 830 K, 10 atm and for path length through gas of 0.388 m [1]

The total band absorptance is the quantity to be modelled in a gas radiation band given by the expression [1]:

$$A_{ij} = \int_{\eta_{L,ij}}^{\eta_{U,ij}} \alpha_{\eta,ij} d\eta \quad (2.1)$$

$\alpha_{\eta,ij}$: spectral absorptivity of species i and band j

$\eta_{L,ij}, \eta_{U,ij}$: lower and upper band limits of species i and band j , respectively

From the above equation, one can see that prediction of total band absorptance requires the dependency of $\alpha_{\eta,ij}$ on wave number η .

2.3 Exponential Wide Band Model (EWBM)

In the Exponential Wide Band Model (EWBM) developed by Edwards and Menard (1964) and Edwards and Balakrishnan (1973), the spectral absorptivity of a homogenous gas of path length L for species i and band j is calculated with the following expression [1]:

$$\alpha_{\eta,ij} = 1 - \exp\left(\frac{-(S/d)_{i,j}\rho_i L}{\sqrt{1 + \frac{(S/d)_{i,j}\rho_i L}{\beta_{i,j}P_{e,i}}}}\right) \quad (2.2)$$

$(S/d)_{i,j}$: mean line intensity to line spacing ratio

ρ_i : density of gas i

L : path length (or mean beam length)

$\beta_{i,j}$: line width to spacing ratio parameter

$P_{e,i}$: dimensionless equivalent broadening pressure for species i

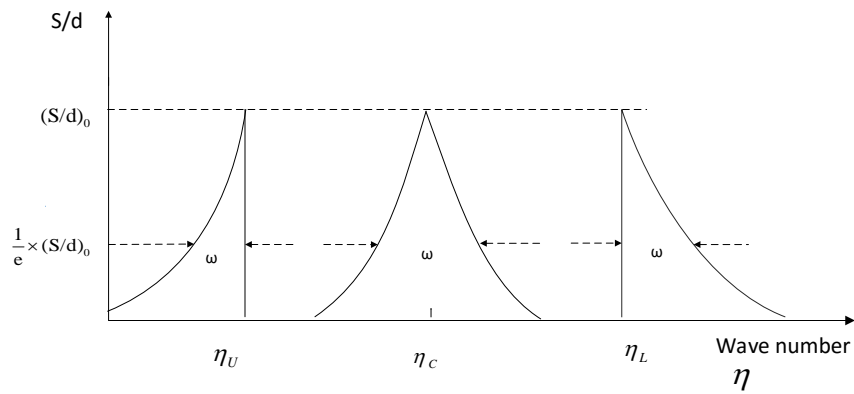


FIGURE 2.2: Band Shapes for Exponential Wide Band [1]

Developing a Wide Band Model (WBM) is to predict how the two narrow band parameters $(S/d)_{i,j}$ and $\beta_{i,j}$ vary with temperature and wave number throughout the entire band. An assumption was made by Edwards and Menard that the smooth spectral absorption coefficient $(S/d)_{i,j}$ has one of the following three shapes (as shown in Figure 2.2):

Case with an upper limit head at $\eta_{U,ij}$:

$$(S/d)_{\eta,ij} = \frac{\alpha_{ij} \exp\left(\frac{-(\eta_{U,ij}-\eta)}{\omega_{ij}}\right)}{\omega_{ij}} \quad (2.3)$$

The Equation 2.3 is valid for $\eta < \eta_{U,ij}$. In case $\eta > \eta_{U,ij}$ the value is $(S/d)_{i,j} = 0$.

Case with symmetrical band with centre at $\eta_{C,ij}$:

$$(S/d)_{\eta,ij} = \frac{\alpha_{ij} \exp(-2 \frac{|\eta - \eta_{C,ij}|}{\omega_{ij}})}{\omega_{ij}} \quad (2.4)$$

Case with a lower limit head at $\eta_{L,ij}$:

$$(S/d)_{\eta,ij} = \frac{\alpha_{ij} \exp(\frac{-(\eta - \eta_{L,ij})}{\omega_{ij}})}{\omega_{ij}} \quad (2.5)$$

The Equation 2.5 is valid for $\eta > \eta_{L,ij}$. In case $\eta < \eta_{L,ij}$ the value is $(S/d)_{i,j} = 0$.

From Equations 2.2 to 2.5, it is clear that three parameters are required to describe the EWBM:

- $\alpha_{i,j}(T)$: integrated band intensity
- $\beta_{i,j}(T)$: line width to spacing ratio parameter
- $\omega_{i,j}(T)$: band width parameter

2.4 The computationally Efficient Exponential Wide Band Model (E-EWBM) formulated in this thesis

In this project, several changes have been implemented in the originally developed C++ code by Yin (2011) to calculate the total emissivity of any gas mixture at any condition using the EWBM [1]. These changes consist of approximations aiming to speed up the calculation, which will make the E-EWBM computationally applicable to CFD, while still producing accurate result as the original EWBM does. The E-EWBM model differs from the originally developed EWBM by Yin (2011) in three aspects:

1. The calculation of the integrated band intensity, $\alpha_{i,j}(T)$ [$cm^{-1}/(g \cdot m)^{-2}$], which physically represents the area under the mean absorption coefficient curve.
2. The calculation of the mean line width to spacing ratio parameter $\beta_{i,j}(T)$.
3. The calculation of the fractional function of blackbody radiation $F(x)$.

In the EWBM, the two parameters in 1 and 2 are calculated based on the quantum mechanics and the parameter in 3 is iteratively solved, which is quite time consuming. The E-EWBM relies more on polynomial correlations and look-up table, which greatly speed up the calculation. Use of the E-EWBM for the calculation of radiative properties of gas mixtures requires the specification of following parameters:

- Total gas temperature T
- Total gas pressure of the gas P_t
- Path length L
- Molar fractions of the different gases in the mixture x_i

The step-by-step procedure for the calculation of total emissivity using the E-EWBM is as follows [2]:

1. For each gas i , calculate the mass-path length product, $\chi_i = \rho_i L$.
2. For band j of gas i , calculate the parameters $P_{e,ij}$, ω_{ij} , α_{ij} and β_{ij} .
3. For band j of gas i , calculate the total band absorptance A_{ij} .
4. For band j of gas i , calculate the band transmissivity τ_{ij} and evaluate the upper and lower limits of each band respectively.
5. All the band limits being calculated, sort in blocks and arrange in increasing order: the lower limit of block $k + 1$ being the same as the upper limit of block k .
6. By comparing whether the limits of a given block belongs to none, one or several absorption bands, compute the block transmissivity as the product of the band transmissivity to which the block belongs.
7. Multiply each block emissivity by the fraction of blackbody radiation in the block limits and sum over all the blocks. The result of this summation gives the total emissivity.

Although only some approximations have been developed in the original EWBM C++ code, the calculation method is explained below in details for all the 7 steps. All the tables and formulas have been taken from the reference [2]. The exact differences between the E-EWBM and the original EWBM are specified over the following parts (i.e., from step 1 to step 7).

Step-1: Calculation of the Mass path length, χ_i

$$\chi_i = \rho_i L = \frac{x_i \cdot P_T \cdot M_i}{R_u \cdot T} L \quad (2.6)$$

ρ : density of gas i [g/m^3]

L : path length (or mean beam length) [m]

x_i : molar fraction of gas i [-]

P_T : total pressure of the mixture [Pa]

M_i : molar weight of gas i [g/mol]

R_u : universal gas constant=8.3144 [$J/mol \cdot K$]

T : gas temperature [K]

Step-2: Calculation of Dimensionless equivalent broadening pressure $P_{e,ij}$, Band width parameter ω_{ij} , Integrated band intensity $\alpha_{ij}(T)$ and Mean line-width to spacing ratio parameter $\beta_{ij}(T)$

- $P_{e,ij}$ is the dimensionless equivalent broadening pressure, sometimes also called the effective pressure. $P_{e,ij}$ accounts for the broadening pressure dependence of the band j of gas i due to collisions with other molecules present in the mixture.

$$P_{e,ij} = \left(\frac{P_T}{P_0} \right)^{n_{ij}} [1 + x_i(b_{ij} - 1)]^{n_{ij}} \quad (2.7)$$

P_0 : a reference pressure: 1 atm=101325 [Pa]

x_i : molar fraction gas [-]

b_{ij} : self-broadening coefficient [-]

n_{ij} : also fitting parameters (similar with b_{ij}) [-].

Refer to Table C.1 in appendix C

- $\omega_{ij}(T)$ is the band width parameter, defined as the width of the mean absorption coefficient $(S/d)_{ij}$ at $1/e$ ($e = 2.718281\dots$) of its maximum value:

$$\omega_{ij}(T) = \omega_0 \left(\frac{T}{T_0} \right)^{0.5} \quad (2.8)$$

ω_0 : band width parameter at a reference temperature $T_0=100$ K. See Table C.1 of appendix C for the value of ω_0 .

• $\alpha_{ij}(T)$ is the integrated band intensity parameter, which represents the area under the curve $(S/d)_{ij} \sim \eta$. The integrated band intensity parameter is solely a function of temperature for species i and band j and is given by expression:

$$\alpha_{ij}(T) = \alpha_0 \left(\frac{[1 - \exp(-\sum_{k=1}^m u_k \delta_k)] \cdot \psi(T)}{[1 - \exp(-\sum_{k=1}^m u_{0,k} \delta_k)] \cdot \psi(T_0)} \right) \quad (2.9)$$

where α_0 : the integrated band intensity constant in the unit of $[cm^{-1}/(g/m^2)]$. The value of α_0 , δ_k and η_k for species i_{th} and j_{th} band can be seen in Table C.1 of appendix C.

$$u_k \equiv \frac{h \cdot c_0 \cdot \eta_k}{k_B T}, u_{0,k} \equiv \frac{h \cdot c_0 \cdot \eta_k}{k_B T_0} \quad (2.10)$$

$T_0=100$ K for convenience

Planck's constant $h = 6.626176 \cdot 10^{-34}$ [J · s]

Speed of light in vacuum $c_0 = 299792458$ [m/s]

Boltzmann constant $k_B = 1.380662 \cdot 10^{-23}$ [J/K]

$\frac{hc_0}{k_B}$, constant = $1.438786 \cdot 10^{-2}$ [m · K]

$$\psi(T) = \left(\frac{\prod_{k=1}^m \sum_{v_k=v_{0,k}}^{\infty} \frac{(v_k + g_k + |\delta_k| - 1)!}{(g_k - 1)! v_k!} e^{-u_k v_k}}{\prod_{k=1}^m \sum_{v_k=0}^{\infty} \frac{(v_k + g_k - 1)!}{(g_k - 1)! v_k!} e^{-u_k v_k}} \right) \quad (2.11)$$

for the lowest possible state of v_k :

$$v_k = \begin{cases} 0 & \delta_k \geq 0 \\ |\delta_k| & \delta_k < 0 \end{cases} \quad (2.12)$$

g_k : degeneracy of the fundamental band, as given in Table C.1 of appendix C.

=1 for non-degenerate vibrations

=2 for η_2 mode of CO₂

=2 for η_2 vibration of CH₄; and =3 for η_3 and η_4 modes of CH₄

The computation of the two terms $\psi(T)$ and $\psi(T_0)$ appearing in the analytical expression of integrated band intensity using Equation 2.11 increases the computational time significantly, thus making implementation of the EWBM in CFD less applicable. In present report, the calculation for the integrated band intensity is simplified by introducing an expression for $\psi(T)$ and $\psi(T_0)$ for each species i and band j . The expressions for $\psi(T)$ along with $\alpha_{ij}(T)$ are given in Table 2.1. The simplified expressions in the table speed up calculation of radiative properties.

Species	Bands[μm]	$\psi(T)$	$\alpha_{ij}(T)$
H ₂ O	Rotational > 10	-	$\alpha_0 \cdot \exp(-9(T_0/T)^{1/2})$
	6.3	s_2	α_0
	2.7(*)	$2 \cdot s_2^2$	Equation 2.9
		s_1	α_0
		s_3	α_0
	1.87	$s_2 \cdot s_3$	Equation 2.9
	1.38	$s_2 \cdot s_3$	Equation 2.9
CO ₂	15	$2 \cdot s_2$	α_0
	10.4	$\exp^{-u_1} (2 - \exp^{-u_1}) s_1 \cdot s_3$	Equation 2.9
	9.4	$\exp^{-u_1} (2 - \exp^{-u_1}) s_1 \cdot s_3$	Equation 2.9
	4.3	s_3	α_0
	2.7	$s_1 \cdot s_3$	Equation 2.9
	2	$2s_1^2 \cdot s_3$	Equation 2.9
CH ₄	7.66	$3 \cdot s_4$	α_0
	3.31	$3 \cdot s_3$	α_0
	2.37	$3 \cdot s_1 \cdot s_4$	Equation 2.9
	1.71	$6 \cdot s_1 \cdot s_2 \cdot s_4$	Equation 2.9
CO	4.7	s_1	α_0
	2.35	$2 \cdot s_1^2$	Equation 2.9

TABLE 2.1: Look up table for $\alpha(T)$

(*) The 2.7 μm H₂O consists of three overlapping bands

Where s_k is defined by following equation:

$$s_k = \frac{1}{1 - \exp^{-u_k}}, u_k \equiv \frac{hc_0 \eta_k}{k_B T} \quad (2.13)$$

The main advantage of these simplified expressions is clear, the integrated band intensity of all fundamental bands is constant and independent of temperature. This implies that half of the absorption bands do not require any calculation. The expressions in Table 2.1 derived for overtone, combination and differences band are simple enough to work together with Equation 2.9. Further, this table makes the calculation of integrated band intensity simple enough for hand calculation.

For species H₂O, CO₂, CO and CH₄, there are in total two special bands that need different treatments:

1) H₂O (>10 μm): for the pure rotational band.

2) H₂O (2.7 μm): the 2.7 μm H₂O band is made up the overlapping of the $\eta_1 = 3652 \text{ cm}^{-1}$ fundamental band, $\eta_3 = 3756 \text{ cm}^{-1}$ fundamental band, and $2\eta_2 = 3190 \text{ cm}^{-1}$ overtone band. It has been suggested to patch the contribution of the three overlapping bands into an equivalent band centered at 3760 cm^{-1} (2.66 μm). The calculation of the equivalent integrated band intensity for this band is $\alpha_{2.7}(T) = \sum_{j=1}^3 \alpha_{2.7}(T)$.

One more advantage of using the above tables is that CO₂ 9.4 μm band can be removed from the list of special bands. This is due to the reason while computing the $\psi(T)$ and $\psi(T_0)$ using Equation 2.11 the set of δ 's of the 10.4 μm (960 cm^{-1}) band of CO₂ must be utilized for both 9.4 μm and 10.4 μm bands respectively. But the look-up tables do not utilize the set of δ 's for computing function $\psi(T)$ and $\psi(T_0)$, thus eliminating the band 9.4 μm of CO₂ from the list of special bands.

• β_{ij} is defined as π times the mean line-width to spacing ratio for a dilute mixture at 1 atm total pressure, i.e.:

$$\beta_{ij} \equiv \frac{\pi\gamma}{dP_e} \quad (2.14)$$

γ : width of a line at half of its maximum intensity level [cm^{-1}]

d : line spacing between two consecutive absorption lines [cm^{-1}]

The temperature dependence of $\beta_{ij}(T)$ is given by:

$$\beta_{ij}(T) = \beta_0 \sqrt{\frac{T_0}{T}} \frac{\phi(T)}{\phi(T_0)} \quad (2.15)$$

where $\phi(T)$ is given by expression:

$$\phi(T) = \left(\frac{\left\{ \prod_{k=1}^m \sum_{v_k=v_{0,k}}^{\infty} \frac{(v_k+g_k+|\delta_k|-1)!}{(g_k-1)!v_k!} e^{-u_k v_k} \right\}^2}{\prod_{k=1}^m \sum_{v_k=0}^{\infty} \frac{(v_k+g_k+|\delta_k|-1)!}{(g_k-1)!v_k!} e^{-u_k v_k}} \right) \quad (2.16)$$

β_0 : the value for each band of each gas can be found in Table C.1 appendix C.

The coefficients $\beta_{ij}(T)$ were calculated using Equations 2.15 and 2.16 in the original EWBM, which is quite time consuming. In this work, the calculation has been implemented in C++ using the following approximated expression:

$$\beta(T) = \beta_0 \sqrt{\frac{T_0}{T}} \left(\sum_{k=0}^4 a_k T^k \right) \quad (2.17)$$

The advantage of using Equation 2.17 instead of Equations 2.15 and 2.16 is an increase of the computational efficiency achieved, obtaining quite similar results for the calculation of $\beta_{ij}(T)$.

Species	Bands[μm]	a_0	a_1	a_2	a_3	a_4
H ₂ O	6.3	0.84230	3.7975e-04	6.6803e-07	1.2324e-09	3.9887e-14
	2.7	1.54095	7.4836e-04	3.4807e-07	2.2125e-09	1.5899e-13
	1.87	0.74454	9.0230e-04	-2.6953e-07	1.8845e-09	7.4664e-14
	1.38	0.79549	7.5882e-04	-4.6984e-07	1.6554e-09	1.0327e-13
CO ₂	15	0.19613	4.6026e-03	-6.5426e-07	1.9376e-08	4.6826e-15
	10.4	-1.65605	1.4951e-02	-2.2221e-05	3.3419e-08	6.3939e-13
	9.4	-1.64289	1.4896e-02	-2.2150e-05	3.3385e-08	6.4455e-13
	4.3	-0.46520	8.6506e-03	-1.0921e-05	2.4181e-08	6.1291e-14
	2.7	-1.56314	1.4952e-02	-2.4018e-05	3.8078e-08	1.4219e-13
	2.0	-2.33309	1.9693e-02	-3.4813e-05	5.0231e-08	7.2356e-15
CH ₄	7.66	1.56484	-6.8944e-03	2.5449e-05	-2.8449e-08	2.7312e-11
	3.31	1.43359	-6.7502e-03	2.6663e-05	-3.1839e-08	2.7962e-11
	1.71	5.26993	-3.0613e-02	8.0130e-05	-8.6364e-08	5.610E-11
CO	4.7	0.96845	-3.1940e-04	1.5869e-06	-4.9542e-10	5.8419e-14
	2.35	0.98939	-5.3279e-04	2.1390e-06	-6.5794e-10	7.6326e-14

TABLE 2.2: Fitting coefficients a_k for $\beta(T)$

The band parameter $\beta_{ij}(T)$ have been calculated in the temperature range 300-3000 K for the absorption bands [2]. Results of these calculations have been utilized to fit fourth order polynomial using a general linear least square method. The fitting coefficients a_k for the bands of H₂O, CO₂, CO and CH₄ are given in Table 2.2.

Only one special band in the calculation of β_{ij} for species H₂O, CO₂, CO and CH₄, which is the pure rotational band of H₂O ($>10 \mu m$). For this band, $\beta(T)$ has to be calculated using the equation $\beta(T) = \beta_0 \sqrt{\frac{T_0}{T}}$.

Step 3 : Calculation of the total band absorptance, A_{ij}

The total band absorptance (or band absorption) A_{ij} of band “j” and species “i” is defined as the integral of spectral absorptivity over the width of band $\Delta\eta_{ij}$:

$$A_{ij} = \int_{\eta_{L,ij}}^{\eta_{U,ij}} \alpha_{\eta,ij} d\eta \quad (2.18)$$

Table 2.3 shows the four-region expressions for the total band absorptance A_{ij} and the mean band transmissivity $\tau_{g,ij}$. Based on the above calculated $(\chi_i, P_{e,ij}, \omega_{ij}, \alpha_{ij}, \beta_{ij})$, the values of A_{ij} and $\tau_{g,ij}$ can be evaluated from the expressions given in Table 2.3.

	Conditions	Region	A_{ij}	$\tau_{g,ij}$
B \geq 1	$0 \leq \tau_H \leq B$	Linear region	$A_{ij} = \omega_{ij} \cdot \tau_H$	$\tau_{g,ij} = 0.9$
	$1/B \leq \tau_H < \infty$	logarithmic region	$A_{ij} = \omega_{ij}(\ln(\tau_H \cdot B) + 2 - B)$	$\tau_{g,ij} = \frac{\omega_{ij}}{A_{ij}}$
B<1	$0 \leq \tau_H \leq B$	Linear region	$A_{ij} = \omega_{ij} \cdot \tau_H$	$\tau_{g,ij} = 0.9$
	$B \leq \tau_H \leq 1/B$	Square region	$A_{ij} = \omega_{ij}(2(\sqrt{B} \cdot \tau_H - B))$	$\tau_{g,ij} = 0.5(1 + \frac{\omega_{ij}}{A_{ij}})$
	$1/B \leq \tau_H < \infty$	logarithmic region	$A_{ij} = \omega_{ij}(\ln(\tau_H \cdot B) + 2 - B)$	$\tau_{g,ij} = \frac{\omega_{ij}}{A_{ij}}$

TABLE 2.3: Table for Exponential Wide Band correlation for an isothermal gas

In Table 2.3, $B = \beta_{ij} \cdot P_{e,ij}$ and $\tau_H = (\alpha_{ij} \cdot \chi_i) / \omega_{ij}$, if calculated value of $\tau_{g,ij} > 0.9$ then value of 0.9 should be taken.

Only one special band: for species H₂O, CO₂, CO and CH₄, which is a pure rotational band of H₂O ($> 10 \mu m$). For this kind of band, the band absorptance is calculated using Equation 2.19, instead of Table 2.3 [2]:

$$\frac{A_{ij}}{\omega_{ij}} = 2E_1(\beta \cdot P_e \cdot \eta_u) + E_1\left(\frac{\eta_u}{2}\right) - E_1\left(\frac{\eta_u}{2}(1 + 2\beta \cdot P_e)\right) + \ln\left(\frac{(\beta \cdot P_e \cdot \eta_u)^2}{1 + 2\beta \cdot P_e}\right) + 2\gamma_E \quad (2.19)$$

η_U : dimensionless parameter, $\eta_u \equiv \frac{1}{\sqrt{\frac{B(1+\frac{B}{\tau_H})}{\tau_H}}}$

$B_{ij}, \tau_{H,ij}$: both defined in Table 2.3

$E_n(x)$: Exponential integral of order n , $E_n(x) \equiv \int_1^\infty \frac{e^{-xt}}{t^n} dt$ where
($n = 0, 1, 2, \dots$)

If $0 \leq x \leq 1$: $E_1(x) + \ln x = a_0 + a_1x + a_2x^2 + a_3x^3 + a_4x^4 + a_5x^5$

$x > 1$: $xe^x E_1(x) = \frac{x^4 + b_1x^3 + b_2x^2 + b_3x + b_4}{x^4 + c_1x^3 + c_2x^2 + c_3x + c_4}$

(a_i, b_i, c_i): coefficients, as given in Table 2.4

Coefficients	i=0	i=1	i=2	i=3	i=4
a_i	-0.57721	0.99999	-0.24991	0.05519	-0.00976
b_i	0	8.57323	18.05901	8.63476	0.26777
c_i	0	9.57332	25.63295	21.09965	3.95849

TABLE 2.4: Table for coefficient a_i , b_i and c_i

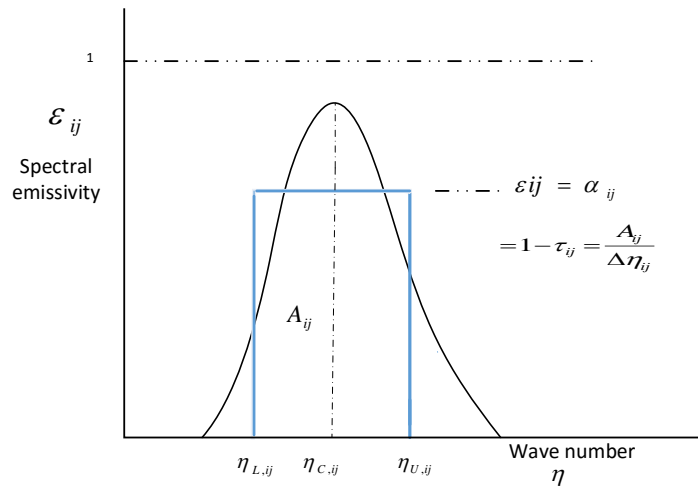


FIGURE 2.3: Gray treatment of CO₂-4.3 μ m [1]

Step 4: Calculation of the band transmissivity and the upper and lower limits of each band

For species i , band j the band transmissivity $\tau_{g,ij}$ can be calculated using the expressions given in Table 2.3. The width of each band $\Delta\eta_{ij}$ is calculated by:

$$\Delta\eta_{ij} \equiv \frac{A_{ij}}{1 - \tau_{g,ij}} \quad (2.20)$$

The lower and the upper band limits are estimated by:

$$(1) \text{ For a symmetrical band with centre at } \eta_{C,ij} = \begin{cases} \eta_{L,ij} \cong \eta_{C,ij} - \frac{1}{2}\Delta\eta_{ij} \\ \eta_{U,ij} \cong \eta_{C,ij} + \frac{1}{2}\Delta\eta_{ij} \end{cases}$$

$$(2) \text{ For a band with an upper wave number head at } \eta_{U,ij}: \eta_{L,ij} \cong \eta_{U,ij} - \Delta\eta_{ij}$$

For species H₂O, CO₂, CO and CH₄ the only asymmetric band is CO₂, 4.3 μm , whose upper wave number is given, as shown by the band shape in Figure 2.3. Rest other bands are symmetrical bands whose central wave number is given in Table C.1 of appendix C.

Step 5: Sort all the bands in blocks in ascending order

After all the band limits are calculated, sort them in blocks and arrange in ascending order, $[\eta_{L,k}, \eta_{U,k}]$, $k = 1, 2, \dots, N$. The lower limit of block $k + 1$ must be the same as the upper limit of block, i.e., $\eta_{L,k+1} = \eta_{U,k+1}$.

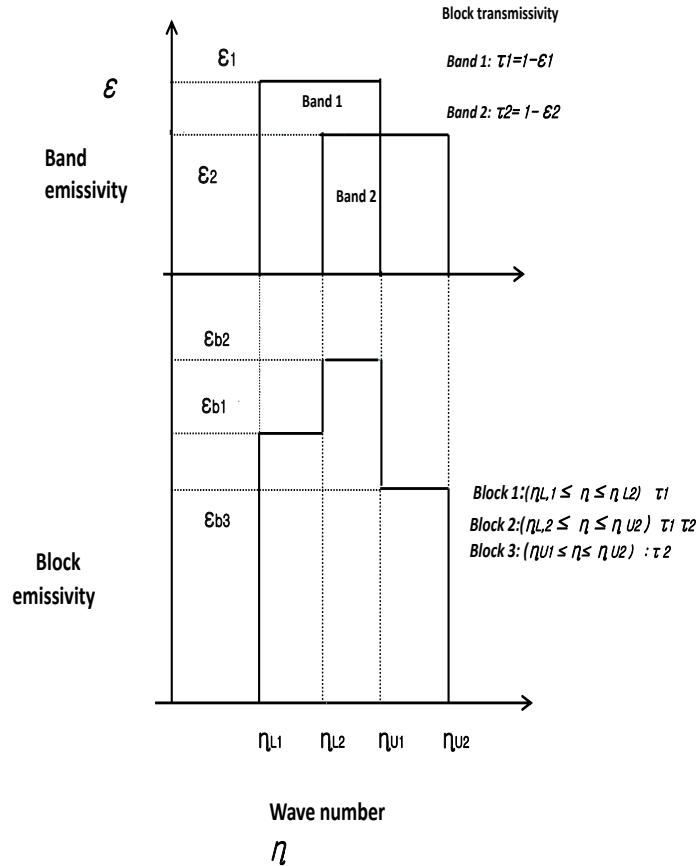


FIGURE 2.4: Treatment of Bands overlapping in EWBM [2]

Step 6: Compute the block transmissivity

After sorting, it is necessary to compute the block transmissivity, which can be estimated by comparing the limits of a given block belongs to no-existing, non-overlapping and overlapping absorption bands. The block transmissivity can be defined as product of the band transmissivity to which block belongs, using Equation 2.21, as demonstrated in Figure 2.4. If there is no band in the interval (or block), then the block emissivity will be one.

$$\tau_{\Delta\eta,k} = \prod \tau_{g,ij} \quad (2.21)$$

Step 7: Calculate the total emissivity of the mixture

The final step is to calculate the total emissivity (ϵ), of a gas/mixture having N distinct spectral regions (blocks) using the E-EWBM as follows:

$$\epsilon \cong \sum_{k=1}^N (1 - \tau_{\Delta,k}) \left[F\left(\frac{\eta_{L,k}}{T}\right) - F\left(\frac{\eta_{U,k}}{T}\right) \right] \quad (2.22)$$

where, $F(x)$ is the fractional function of blackbody radiation, defined as:

$$F(\lambda T) = F_{0 \rightarrow \lambda T} \equiv \frac{\int_0^\lambda e_{b\lambda} d\lambda}{\int_0^\infty e_{b\lambda} d\lambda} = \int_0^{\lambda T} \frac{e_{b\lambda}}{\sigma T^5} d(\lambda T) \quad (2.23)$$

$$= F\left(\frac{\eta}{T}\right) = \frac{15}{\pi^4} \sum_{n=1}^{\infty} \left[\frac{e^{-n\xi}}{n} \left(\xi^3 + \frac{3\xi^2}{n} + \frac{6\xi}{n^2} + \frac{6}{n^3} \right) \right] \quad (2.24)$$

$$\xi \equiv \frac{C_2}{\lambda T} = C_2 \frac{\eta}{T}$$

$$C_2 \equiv \frac{hc_0}{k_B} = 1.438786 \cdot 10^{-2} [m \cdot K] : \text{Planck radiation constant}$$

$$h = 6.626176 \cdot 10^{-34} [J \cdot s] : \text{Planck constant}$$

$$c_0 = 29979245 \text{ [m/s]: speed of light in vacuum}$$

$$k_B = 1.380662 \cdot 10^{-23} [J/K]: \text{Boltzmann constant}$$

$$e_{b\lambda}: \text{Planck's constant distribution of emissive power}$$

The series in Equation 2.24 require a number of terms to obtain the desired accuracy. For $\xi \geq 2$ five or six terms are usually sufficient to achieve up to 8 digit accuracy. However, for $\xi \leq 2$, more terms must be calculated to achieve same accuracy, thus increasing the computational time needed to calculate. However, the International Flame Research Foundation (IFRF) report recommends the use of Equation 2.25 if $\xi < 2$ [2]:

$$F(\lambda T) = 1 - \frac{15}{\pi^4} \cdot \xi^3 \left(\frac{1}{3} - \frac{\xi}{8} - \frac{\xi^2}{60} - \frac{\xi^4}{5040} + \frac{\xi^6}{272160} - \frac{\xi^8}{13305600} \right) \quad (2.25)$$

However, when Equation 2.24 and 2.25 are implemented in C++ codes and results are compared with the IFRF report results are fairly accurate up to 5 decimal places. At this point the implementation of these equations to the E-EWBM model is fairly justified. The total emissivity of any combustion gas mixture at any condition can be calculated using the above explained steps, from which the effective absorption coefficient of the gas mixture, K_a , can be evaluated by using equation [2]:

$$K_a = -\frac{1}{L} \ln(1 - \epsilon) \quad (2.26)$$

Before making use of the computer code to derive useful emissivity database and further gas radiative property models applicable to CFD modeling, one has to assure the correctness of the above description of the E-EWBM (the equations, parameters and calculation procedure) and the developed C++ code. The following section demonstrates the calculation of the total emissivity of a given gas mixture.

2.4.1 E-EWBM C++ code: validation with IFRF example

The total emissivity of following gas mixture has been calculated using the above mentioned steps in section 2.4. The calculation presented in Figure 2.5 has been done at following conditions:

- Mean beam length = 0.5 m
- Total gas temperature T=1500 K
- Total gas pressure of the gas $P_T=1$ atm

Further, the composition of the gas is as follows:

The gas mixture consists of 4 participating species H_2O ($i=0$), CO_2 ($i=1$), CO ($i=2$) and CH_4 ($i=3$). Their molar fraction are $x_{H_2O}=0.160$, $x_{CO_2}=0.085$, $x_{CO}=0.020$ and $x_{CH_4}=0.005$.

[1] Calculation of the lower and upper band limits of the participating species involved -----										
lambda[micro]	X[g/m2]	Pe	omega[cm^-1]	alpha[m2/(g^2cm)]	beta	A_tot[cm^-1]	tau_g	delta_eta[cm^-1]	eta_L[cm^-1]	eta_U[cm^-1]
H2O										
71.43	11.7090	1.2753	268.398	4327.750522	0.03695	879.403	0.3052	1265.701	0.000	772.850
6.25	11.7090	1.2753	218.436	41.200000	0.17711	259.212	0.5952	640.296	1279.852	1920.148
2.66	11.7090	1.2753	232.379	24.995037	0.39998	253.976	0.7334	952.494	3283.753	4236.247
1.87	11.7090	1.2753	166.926	3.913281	0.17360	45.344	0.9000	453.443	5123.279	5576.721
1.38	11.7090	1.2753	123.935	2.647639	0.20976	31.001	0.9000	310.011	7094.995	7405.005
CO2										
14.99	15.1962	1.0178	49.187	19.000000	1.12948	136.241	0.3610	213.219	560.391	773.609
10.42	15.1962	1.0203	51.898	0.156331	0.90029	2.376	0.9000	23.756	948.122	971.878
9.43	15.1962	1.0203	39.117	0.158436	2.66439	2.408	0.9000	24.076	1047.962	1072.038
4.15	15.1962	1.0203	43.377	110.000000	4.45940	201.774	0.2150	257.030	2152.970	2410.000
2.73	15.1962	1.0165	91.015	5.953672	3.30884	90.473	0.9000	904.730	3207.635	4112.365
1.92	15.1962	1.0165	133.618	0.138024	12.02041	2.097	0.9000	20.974	5189.513	5210.487
CO										
4.67	2.2757	1.0016	98.761	20.900000	0.05201	26.141	0.5984	65.093	2110.454	2175.546
2.35	2.2757	1.0000	77.460	0.181109	0.13712	0.412	0.9000	4.122	4257.939	4262.061
CH4										
7.63	0.3259	1.0012	81.333	28.000000	2.03783	9.124	0.9000	91.238	1264.381	1355.619
3.31	0.3259	1.0012	216.887	46.000000	1.53757	14.989	0.9000	149.892	2945.054	3094.946
2.37	0.3259	1.0012	232.379	4.248850	9.89862	1.384	0.9000	13.845	4213.078	4226.922
1.71	0.3259	1.0012	174.284	0.811520	23.41090	0.264	0.9000	2.644	5859.678	5862.322
[2] Calculation of band transmittances, Planck Blackbody Fractional Function, & the total emissivity										
eta_L[cm^-1]	eta_U[cm^-1]	OverlappingBands	tau_1	tau_2	tau_b	f_U	f_L	(1-tau_b)^delta_f		
0.00	560.39	(0, 0) (99,99)	0.3052	1.0000	0.3052	1.00000	0.99352	0.004502		
560.39	772.85	(0, 0) (1, 0)	0.3052	0.3610	0.1102	0.99352	0.98433	0.008176		
772.85	773.61	(1, 0) (99,99)	0.3610	1.0000	0.3610	0.98433	0.98429	0.000027		
773.61	948.12	(99,99) (99,99)	1.0000	1.0000	1.0000	0.98429	0.97298	0.000000		
948.12	971.88	(1, 1) (99,99)	0.9000	1.0000	0.9000	0.97298	0.97116	0.000181		
971.88	1047.96	(99,99) (99,99)	1.0000	1.0000	1.0000	0.97116	0.96491	0.000000		
1047.96	1072.04	(1, 2) (99,99)	0.9000	1.0000	0.9000	0.96491	0.96280	0.000212		
1072.04	1264.38	(99,99) (99,99)	1.0000	1.0000	1.0000	0.96280	0.94346	0.000000		
1264.38	1279.85	(3, 0) (99,99)	0.9000	1.0000	0.9000	0.94346	0.94172	0.000174		
1279.85	1355.62	(0, 1) (3, 0)	0.5952	0.9000	0.5357	0.94172	0.93282	0.004132		
1355.62	1920.15	(0, 1) (99,99)	0.5952	1.0000	0.5952	0.93282	0.84848	0.034147		
1920.15	2110.45	(99,99) (99,99)	1.0000	1.0000	1.0000	0.84848	0.81415	0.000000		
2110.45	2152.97	(2, 0) (99,99)	0.5984	1.0000	0.5984	0.81415	0.80616	0.003205		
2152.97	2175.55	(1, 3) (2, 0)	0.2150	0.5984	0.1286	0.80616	0.80189	0.003728		
2175.55	2410.00	(1, 3) (99,99)	0.2150	1.0000	0.2150	0.80189	0.75599	0.036032		
2410.00	2945.05	(99,99) (99,99)	1.0000	1.0000	1.0000	0.75599	0.64526	0.000000		
2945.05	3094.95	(3, 1) (99,99)	0.9000	1.0000	0.9000	0.64526	0.61382	0.003144		
3094.95	3207.63	(99,99) (99,99)	1.0000	1.0000	1.0000	0.61382	0.59031	0.000000		
3207.63	3283.75	(1, 4) (99,99)	0.9000	1.0000	0.9000	0.59031	0.57452	0.001578		
3283.75	4112.37	(0, 2) (1, 4)	0.7334	0.9000	0.6600	0.57452	0.41325	0.054831		
4112.37	4213.08	(0, 2) (99,99)	0.7334	1.0000	0.7334	0.41325	0.39545	0.004745		
4213.08	4226.92	(0, 2) (3, 2)	0.7334	0.9000	0.6600	0.39545	0.39304	0.000819		
4226.92	4236.25	(0, 2) (99,99)	0.7334	1.0000	0.7334	0.39304	0.39142	0.000432		
4236.25	4257.94	(99,99) (99,99)	1.0000	1.0000	1.0000	0.39142	0.38767	0.000000		
4257.94	4262.06	(2, 1) (99,99)	0.9000	1.0000	0.9000	0.38767	0.38696	0.000071		
4262.06	5123.28	(99,99) (99,99)	1.0000	1.0000	1.0000	0.38696	0.25687	0.000000		
5123.28	5189.51	(0, 3) (99,99)	0.9000	1.0000	0.9000	0.25687	0.24839	0.000848		
5189.51	5210.49	(0, 3) (1, 5)	0.9000	0.9000	0.8100	0.24839	0.24575	0.000502		
5210.49	5576.72	(0, 3) (99,99)	0.9000	1.0000	0.9000	0.24575	0.20306	0.004269		
5576.72	5859.68	(99,99) (99,99)	1.0000	1.0000	1.0000	0.20306	0.17432	0.000000		
5859.68	5862.32	(3, 3) (99,99)	0.9000	1.0000	0.9000	0.17432	0.17406	0.000025		
5862.32	7094.99	(99,99) (99,99)	1.0000	1.0000	1.0000	0.17406	0.08549	0.000000		
7094.99	7405.01	(0, 4) (99,99)	0.9000	1.0000	0.9000	0.08549	0.07076	0.001473		
7405.01	10000.00	(99,99) (99,99)	1.0000	1.0000	1.0000	0.07076	0.00000	0.000000		
!!! (i,j) means the j-th band of i-th species; (99,99) means NO BANDs (transmissivity=1) !										
[3] The Total Emissivity = 0.167252356										
The Equivalent (Grey) Absorption Coefficient, $-(1/L)*\log(1-total_emissivity)=$ 0.36604926										

FIGURE 2.5: Result obtained from C++

The previous conditions were chosen to compare the result with one computed in the IFRF report [2]. The emissivity calculated by the E-EWBM developed in this work is 0.167252356, while the emissivity reported in the given reference is 0.167253. Hence, it can be concluded that the E-EWBM code is reliable and well validated.

2.5 Other gas radiative property models used for comparison in this thesis

2.5.1 Smith et al. (1982) air-fuel WSGGM

It postulates that the total emissivity of participating gases may be represented by the sum of the emissivities of several hypothetical gray gases and one clear gas, weighted by temperature-dependent factors. In this method each of the N gray gases has a constant pressure absorption coefficient k_i and for the clear gas $k_i=0$. The total emissivity of the WSGGM is calculated from the following equation [4]:

$$\epsilon = \sum_{i=0}^N a_{\epsilon,i}(T_g)(1 - e^{-k_i PL}) \quad (2.27)$$

where $a_{\epsilon,i}(T_g)$ is the temperature-dependent emissivity weighting factor for the i th gray gas and T_g is the gas temperature (K). The above equation can be used to calculate the emissivity of the i th gray gas whose pressure absorption coefficient is k_i ($\text{atm}^{-1} \cdot \text{m}^{-1}$). For a mixture of gas P is the sum of partial pressures of participating gases (atm) and L is the beam length (m). The weighted factors are calculated from [4]:

$$a_{\epsilon,i}(T_g) = \sum_{j=1}^J b_{\epsilon,i,j} \cdot T_g^{j-1}, (i = 1, \dots, N, a_{\epsilon,i} > 0) \quad (2.28)$$

From the Equation 2.27 it is clear that the total emissivity is an increasing function of the partial-beam length product and it approaches to 1 as its maximum limit. Therefore, the weighting factor $a_{\epsilon,i}(T_g)$ must be positive and sum to 1.

Species	Condition
Carbon dioxide	$P_c \rightarrow 0$ atm
Gas mixture	$P_w/P_c=1$ ($P_c=0.1$ atm)
Gas mixture	$P_w/P_c=2$ ($P_c=0.1$ atm)
Water vapor	$P_w \rightarrow 0$ atm
Water vapor	$P_w=1$ atm

TABLE 2.5: Emissivity data base generated for partial pressure of CO₂ and H₂O vapor in Smith et al. (1982) WSGGM [4]

In the work done by Smith et al. (1982), the Exponential Wide Band Model (EWBM) was used as a reference model to generate the emissivity databases. The emissivity databases were generated for five partial pressures of CO₂ and H₂O vapor.

Then, the emissivity data can be fitted by three gray gases plus one clear gas WSGGM and third-order temperature polynomials; i.e., $N=3$ and $J=4$ in Equation 2.27 and Equation 2.28. The five sets of model coefficients used in order to generate emissivity can be found in Table A1 of appendix A. The Smith et al. (1982) WSGGM is valid for $0.001 \leq PL \leq 10$ atm m and $600 \leq T_g \leq 2400$ K.

2.5.2 Yin (2013) air-fuel WSGGM

Yin (2013) has refined the air-fuel WSGGM and compared it with the Smith et al. (1982) WSGGM. The refined WSGGM is found to significantly outperform the Smith et al. WSGGM in terms of accuracy.

In his work, Yin has derived new coefficients for four gray gas plus one clear gas WSGGM, i.e., k_i , $b_{\epsilon,i,1}$, $b_{\epsilon,i,2}$, $b_{\epsilon,i,3}$ and $b_{\epsilon,i,4}$ ($i = 1, 2, 3, 4$). In order to improve the data fitting accuracy, the gas temperature is normalized by a reference temperature $T_{ref}=1200$ K. Instead of Equation 2.28, the weighting factors in the refined WSGGM is computed by [4]:

$$a_{\epsilon,i}(T_g) = \sum_{j=1}^J b_{\epsilon,i,j}(T_g/T_{ref})^{j-1}, (i = 1 \dots N, a_{\epsilon,i} > 0) \quad (2.29)$$

Species	Condition
Carbon dioxide	$P_c \rightarrow 0$ atm
Gas mixture	$P_w/P_c=0.05$ ($P_c=0.1$ atm)
Gas mixture	$P_w/P_c=1$ ($P_c=0.1$ atm)
Gas mixture	$P_w/P_c=2$ ($P_c=0.1$ atm)
Water vapor	$P_w \rightarrow 0$ atm
Water vapor	$P_w=0.05$ atm
Water vapor	$P_w=1$ atm

TABLE 2.6: Emissivity data base generated for partial pressure of CO₂ and H₂O vapor in Yin (2013) WSGGM [4]

In his work, the emissivity databases were generated for seven partial pressures of CO₂ and H₂O vapor. Then, the emissivity data can be fitted by four gray gas plus one clear

gas WSGGM and third-order temperature polynomial; i.e, $N=4$ and $J=4$ in Equation 2.27 and Equation 2.29. The seven sets of model coefficients used in order to generate emissivity can be found in Table A2 of appendix A. The Yin (2013) WSGGM has been validated for $0.001 \leq PL \leq 60 \text{ atm} \cdot \text{m}$ and $500 \leq T_g \leq 3000 \text{ K}$.

2.5.3 Yan et al. (2015) E-EWBM

For any radiation model it is important that it should calculate the absorption coefficient accurately. Yan et al. (2015) has developed a computational efficient model in order to calculate the absorption coefficient. In his work, some reference EWBM parameters are calculated based on the Line by Line method and HITEMP-2010, which is a spectroscopic data-base that contains more hot lines than HITRAN database and is more accurate for high temperature radiation calculation. Mathematical regression is done to simplify the model. The calculation steps for this model is precisely the same as discussed in section 2.3. The only differences are in computation of the following parameters [7]:

- $\alpha_{0ij}(T)$: reference band intensities
- $\alpha_{ij}(T)$: the integrated band intensity
- $\beta_{ij}(T)$: mean line width to spacing ratio parameter

A polynomial fitting method is used in order to compute $\alpha_{0ij}(T)$, $\alpha_{ij}(T)$ and $\beta_{ij}(T)$. This fitting is done for the temperature range from 300-2500 [K]. Then, the generated data are used in Equations 2.30, 2.31 and 2.32 to compute the $\alpha_{0ij}(T)$, $\alpha_{ij}(T)$ and $\beta_{ij}(T)$ respectively for different species at varying band. The polynomial coefficient for $\alpha_{ij}(T)$ and $\beta_{ij}(T)$ are fitted for the temperature range 300-2500 [K]. The coefficients can be found in appendix B.

$$\alpha_{0ij}(T) = b_0 + b_1T^1 + b_2T^2 + b_3T^3 + b_4T^4 + b_5T^5 + b_6T^6 + b_7T^7 + b_8T^8 + b_9T^9 \quad (2.30)$$

$$\alpha_{ij}(T) = b_0 + b_1T + b_2T^2 + b_3T^3 + b_4T^4 + b_5T^5 + b_6T^6 + b_7T^7 \quad (2.31)$$

$$\beta_{ij}(T) = b_0 + b_1T + b_2T^2 + b_3T^3 + b_4T^4 + b_5T^5 + b_6T^6 + b_7T^7 \quad (2.32)$$

where $b_n =$ polynomial coefficient.

The reference band intensities $\alpha_{0ij}(T)$ for some species are recalculated in his work. This is due to the fact that some literature gave different reference band intensity values, but these values are not accurate enough compared with LBL results obtained from the HITEMP 2010 data-base. When they are used to calculate the Planck mean absorption coefficient substantial error occurred. Reference rotational band intensities of H_2O for the bands centered at 140 cm^{-1} and 1600 cm^{-1} were recalculated. For CO_2 , the reference band intensities centered at 667 cm^{-1} and 2410 cm^{-1} were recalculated. Similarly for CO , the reference band intensity for band centered at 2143 cm^{-1} was recalculated. The reference band intensities are considered as a function of temperature. Since HITEMP database does not include CH_4 , the reference band intensities are not included [7].

2.6 Emissivity as a function of temperature and beam length: Comparison of the 4 models

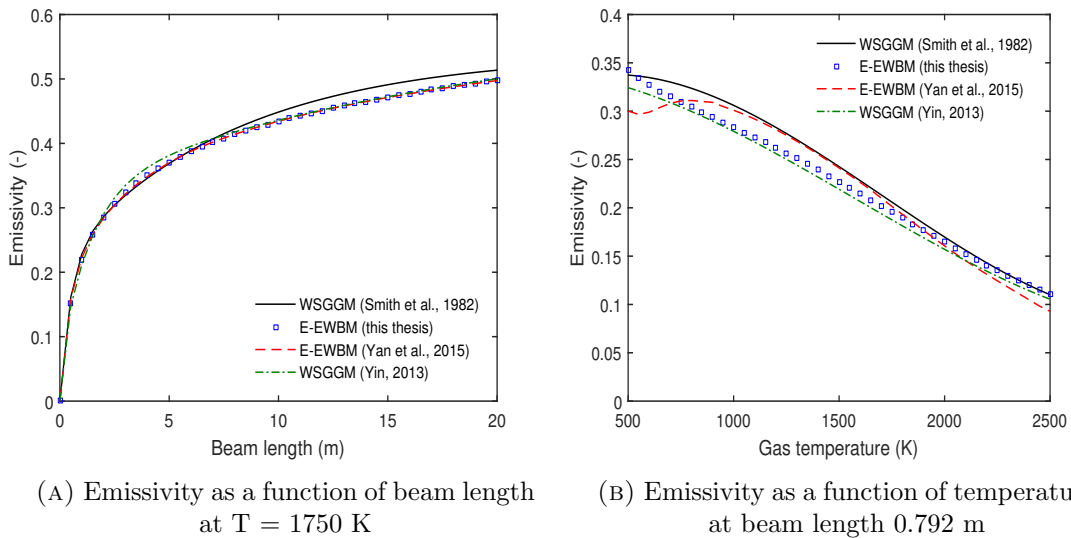


FIGURE 2.6: Emissivity as a function of temperature and beam length at condition $P_w/P_c=2$ ($P_c=0.1 \text{ atm}$) and $x_{\text{H}_2\text{O}}=0.2$, $x_{\text{CO}_2}=0.1$, $x_{\text{CO}}=0.0$ and $x_{\text{CH}_4}=0.0$

Figure 2.6 shows the calculated emissivity as a function of beam length and temperature. The calculation has been done at condition ($P_w/P_c=2$, where $P_c=0.1 \text{ atm}$), and gas temperature equals to 1750 K. The gas mixture consists of four participating species

H_2O ($i=0$), CO_2 ($i=1$), CO ($i=2$) and CH_4 ($i=3$). Their molar fraction are $x_{\text{H}_2\text{O}} = 0.2$, $x_{\text{CO}_2} = 0.1$, $x_{\text{CO}} = 0.0$ and $x_{\text{CH}_4} = 0.0$.

It can be seen from Figure 2.6A that the three radiation models, i.e., WSGGM (Yin, 2013), E-EWBM (this thesis) and E-EWBM (Yan et al., 2015) are quite close to each other. As expected, with default WSGGM the emissivity varies when the beam length becomes larger.

Figure 2.6B shows the calculated emissivity as a function of temperature. It can be seen from the graph that relative difference of emissivity decreases when the temperature increases for a beam length of 0.792 m.

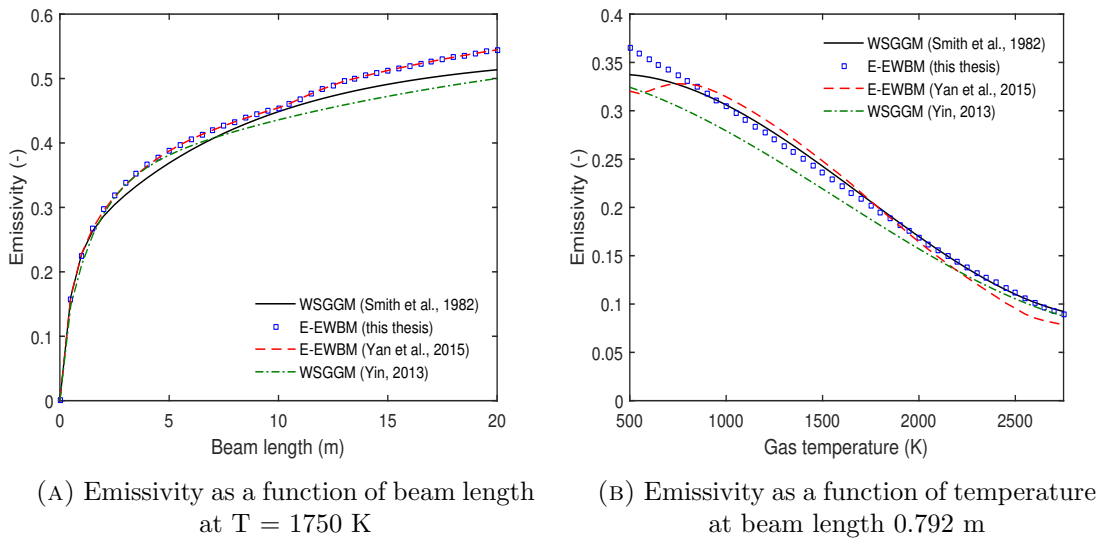


FIGURE 2.7: Emissivity as a function of temperature and beam length at condition $P_w/P_c=2$ ($P_c=0.1$ atm) and $x_{\text{H}_2\text{O}}=0.2$, $x_{\text{CO}_2}=0.1$, $x_{\text{CO}}=0.020$ and $x_{\text{CH}_4}=0.005$

Figure 2.7 shows the calculated emissivity as a function of beam length and temperature. The calculation has been done at condition ($P_w/P_c=2$, where $P_c=0.1$ atm), and gas temperature equals to 1750 K. The gas mixture consists of four participating species H_2O ($i=0$), CO_2 ($i=1$), CO ($i=2$) and CH_4 ($i=3$). Their molar fraction are $x_{\text{H}_2\text{O}} = 0.2$, $x_{\text{CO}_2} = 0.1$, $x_{\text{CO}} = 0.020$ and $x_{\text{CH}_4} = 0.005$.

The differences observed in Figure 2.6 and 2.7 are due to the fact that both E-EWBM take into account the effect of CO and CH_4 on emissivity.

It can be seen from the Figure 2.7A that some differences can be observed in the emissivities predicted by the E-EWBM and different WSGGMs when the beam length becomes larger.

The Figure 2.7B shows the calculated emissivity as a function of temperature. It can be seen from the graph that relative difference of emissivity decreases when the temperature increases for a beam length of 0.792 m.

From figures above, it can be concluded that relative differences in the emissivities are quite high over a temperature range of 500-2750 K. It signifies that the E-EWBM leads to more accurate result of radiative properties for CFD modelling.

2.7 Conclusion

A computer code in C++ for the simplified E-EWBM has been developed and validated to evaluate total emissivity of any gas mixture at any condition. Further, the different radiation models such as the WSGGM (Smith et al., 1982), WSGGM (Yin, 2013) and E-EWBM (Yan et al., 2015) have been studied. Furthermore, for all above mentioned radiation models the emissivity as a function of temperature and beam length plots have been studied. Remarkable differences can be seen in the plots of emissivity as a function of beam length, which justifies the implementation of E-EWBM in air-fuel and oxy-fuel furnaces.

Chapter 3

Implementation and impact of the E-EWBM in air-fuel combustion CFD

This chapter describes the implementation and impact of the E-EWBM in air-fuel combustion. Firstly, the geometry of the furnace is described together with the operational and boundary conditions. Then, the models and parameters used for simulations are discussed. The modelling includes turbulence, radiative heat transfer and reaction mechanisms. Further, the material properties and solution methods selected are described. Then, the effect of mesh is presented. Lastly, the impacts of different gas radiative property models and different global combustion mechanisms are discussed.

3.1 Furnace

The geometry of the furnace is presented, followed by the operational conditions (i.e., the conditions used in the CFD study) and the experimental data used for comparing with the simulation results.

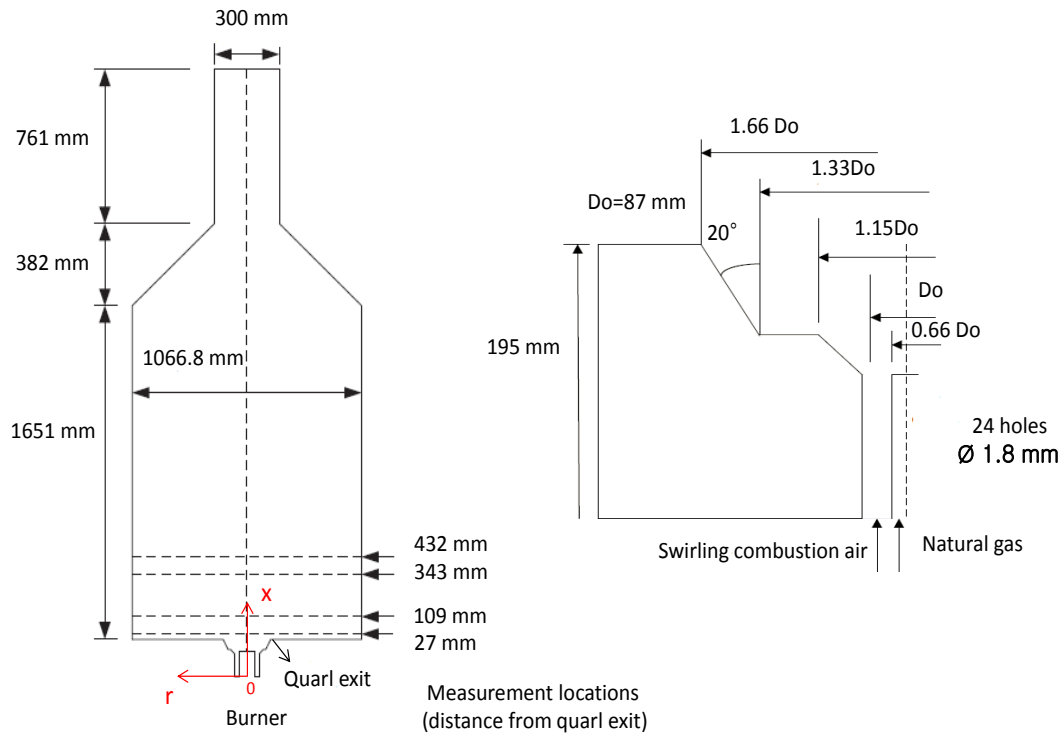


FIGURE 3.1: To the left is a 2D axi-symmetric furnace for air-fuel combustion and to the right is the close-up view of the burner

3.1.1 Geometry

The furnace is vertically-fired and of octagonal cross section with a conical furnace hood and a cylindrical exhaust duct. The furnace walls are refractory-lined or water cooled. The burner features 24 radial fuel ports and a bluff centerbody. Air is introduced through an annular inlet and movable swirl blocks are used to impart swirl. The problem is modelled as a 2D axi-symmetric representation of a 3D problem. The combustor dimensions and close-up view of the burner are given in Figure 3.1 above [6].

3.1.2 Fuel and air composition

The air composition used in all simulations is given by Table 3.1, whereas the fuel composition used in all simulations is given by Table 3.2. The composition of air and fuel are taken from the reference [5].

Species	Mass fraction	Molecular weight [kg/kmol]
O ₂	0.23	31.9988
N ₂	0.77	28.0134

TABLE 3.1: Air composition used in air-fuel case [5]

Species	Mass fraction	Molecular weight [kg/kmol]	Standard state enthalpy [$\frac{J}{kg.mol}$]
CH ₄	0.97	16.04303	7.489518e+07
CO ₂	0.008	44.00995	3.935324e+08
N ₂	0.022	28.0134	0

TABLE 3.2: Fuel composition used in air-fuel case [5]

It can be seen from Table 3.2 that methane is the dominating species in the fuel, with mass fraction of 0.97. Thus, an assumption is made at this stage that the only alkane present in fuel is CH₄.

3.1.3 Boundary conditions

The operational conditions of the air-fuel furnace, which are used as the boundary conditions in the CFD study, are taken from tutorial 17 in the reference [6]. These conditions for the fuel inlet, air inlet, outlet and walls are given in the tables below. The axial and swirl velocities of the air stream at the inlet are given by Figure 3.3.

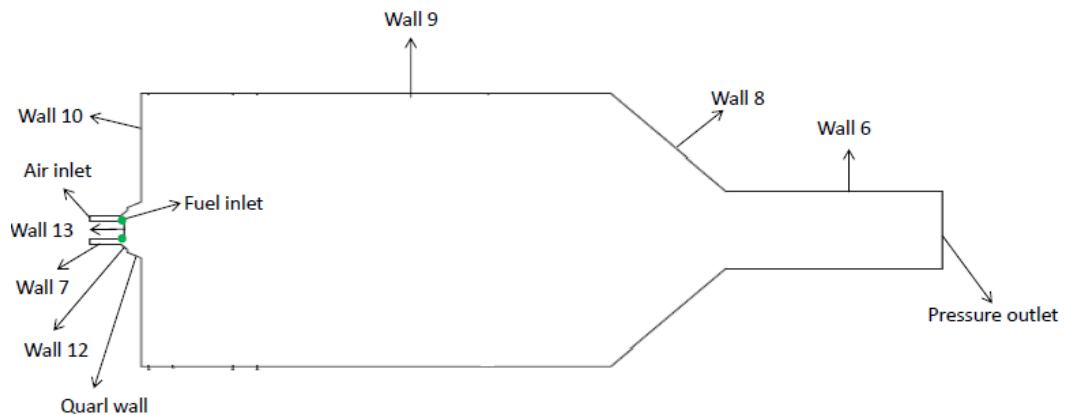
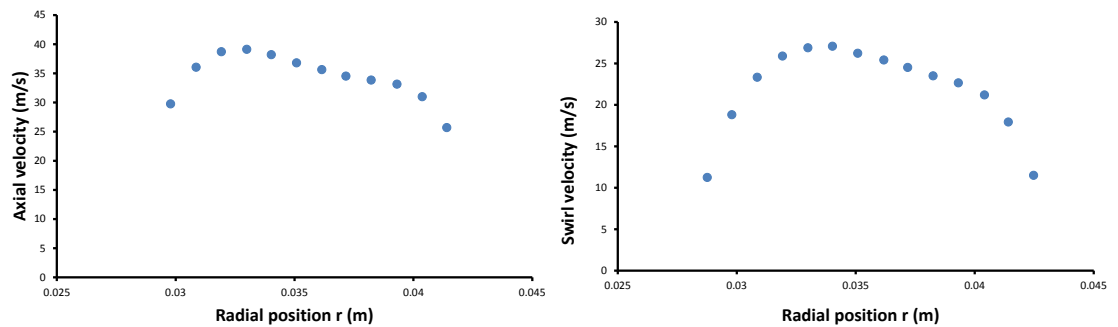


FIGURE 3.2: Boundaries used of furnace for air-fuel case

Inlet	Air-inlet	Fuel-inlet
Boundary type	Velocity-inlet	Velocity-inlet
Axial velocity [m/s]	Vel-prof-u	0
Radial velocity [m/s]	0	157.25
Swirl velocity [m/s]	vel-prof-w	0
Turbulent intensity	17 %	5 %
Hydraulic diameter [m]	0.029	0.0018
Inlet temperature [K]	312	308
Composition	Table 3.1	Table 3.2

TABLE 3.3: Boundary conditions for the fuel and air inlets [6]



(A) Axial velocity profile

(B) Swirl velocity profile

FIGURE 3.3: Axial and swirl velocity profile of the air stream at the inlet

Outlet	Pressure-outlet
Boundary type	Pressure-outlet
Back flow turbulent intensity	5 %
Hydraulic diameter [m]	0.3
Back flow temperature [K]	1300

TABLE 3.4: Boundary conditions for outlet in air-fuel case [6]

The temperature profile along the wall 9 is given by the following equation, where $0.195 \leq x \leq 1.845$ m is the position along the wall.

$$T(x) = a_0 + a_1(x + 0.195) + \dots + a_6(x + 0.195)^6 \quad (3.1)$$

The coefficients of a_i are given in Table 3.6.

Wall	Temperature[K]	Internal emissivity
Wall 6	1370	0.5
Wall 7	312	0.5
Wall 8	1305	0.5
Wall 9	temp-prof t, T(x)	0.5
Wall 10	1100	0.5
Quarl wall	1273	0.5
Wall 12	1173	0.5
Wall 13	1173	0.5

TABLE 3.5: Boundary conditions for walls [6]

Coefficients	Values
a_0	1.257e03
a_1	-2.177e03
a_2	9.9349e03
a_3	-1.74799e04
a_4	1.46151e04
a_5	-5.83885e03
a_6	8.98612e02

TABLE 3.6: Coefficients of the temperature profile along the furnace cylinder wall in the hot wall configuration [5]

3.1.4 Experimental data available

The CFD results have been plotted on four measuring lines along the radial direction from the centerline at four axial locations, i.e., 27 mm, 109 mm, 343 mm and 432 mm downstream from the quarl exit, on which experimental data are available in literature [7]. These measurement locations are shown in Figure 3.1. The experimental data in reference [5] are found to be same as in the reference [7]. The plotted parameters for which experimental data are available are gas temperature, axial velocity and O₂ mass fraction.

3.2 Computational cases: an overview

Table 3.7 gives an overview of the main models used in the air-fuel simulations, with more details to be given in the subsequent sections.

Software	Ansys V15.0
Time/space	Steady/Axi-symmetric swirl
Mesh	9784 cells vs. 39136 cells vs. 156544 cells
Turbulence	Realizable $k - \epsilon$ with Enhanced Wall Treatment
Radiation	DO with 4 different radiative property models
	E-EWBM (this thesis)
	WSGGM (Smith et al., 1982)
	WSGGM (Yin, 2013)
	E-EWBM (Yan et al., 2015)
Reaction	Species transport with 4 different reaction mechanisms
	1-step
	2-step WD
	4-step JL-1
	4-step (Yan et al., 2015)

TABLE 3.7: Overview of the main models used in the air-fuel simulations

3.3 Turbulence modelling

In CFD, various governing equations are solved numerically using the finite volume method for the turbulent reacting flow. The partial differential equations expressing conservation of mass, momentum, energy and species concentration can be given by a same general equation [3].

$$\frac{\partial(\rho\phi)}{\partial t} + \frac{\partial(\rho u_i \phi)}{\partial x_i} = D_\phi + S_\phi \quad (3.2)$$

The first term on the left hand side is the unsteady term. The second term is the convective term, ρ is the density term and u_i is the velocity component along the x_i direction. The first term on right is the diffusive term, while the second term is the source term. In turbulent flows, the instantaneous values of the variable ϕ can be expressed as the sum of a mean term $\bar{\phi}$ and a fluctuating term ϕ' . The fluctuating part of $\bar{\phi}$ leads to additional terms in the conservation equations, representing the transport of ϕ due to turbulent fluctuation. The main task of turbulence model is to express these fluxes in terms of mean properties of the flow, with additional equations which determine the closure of model [3]. In this project, the realizable k- ϵ model is used to better account for the swirling flow in the furnace.

3.3.1 Realizable k- ϵ model

The k- ϵ is an eddy-viscosity model in which Reynolds stresses are assumed to be proportional to the rate of strain, with the constant of proportionality given by the turbulent viscosity μ_t .

$$-\overline{\rho u'_i u'_j} = \mu_t \left(\frac{\partial u_i}{\partial x_j} + \frac{\partial u_j}{\partial x_i} \right) \quad (3.3)$$

$-\overline{\rho u'_i u'_j}$ is called Reynolds stresses or Turbulent stresses. The turbulent viscosity is given by the following expression:

$$\mu_t = \rho C_\mu \frac{k^2}{\epsilon} \quad (3.4)$$

where c_μ is given by, $c_\mu = \frac{1}{A_0 + A_s U^* \frac{k}{\epsilon}}$. A_0 and A_s are model constants. U^* is given by the expression $U^* = \sqrt{S_{ij}S_{ij} + \tilde{\Omega}_{ij}\tilde{\Omega}_{ij}}$. $\tilde{\Omega}_{ij} = \Omega_{ij} - 2\epsilon_{ijk}\omega_k$, Ω_{ij} is called mean rate of rotation tensor [s^{-1}] and ω_k is called angular velocity [rad/s].

The k- ϵ turbulence model solves transport equations for the turbulent kinetic energy k [$\frac{m^2}{s^2}$] and turbulent energy dissipation rate ϵ [$\frac{m^2}{s^3}$].

The term realizable means that the model satisfies certain mathematical constraints on Reynolds stress consistence with physics of turbulent flows. The realizable k- ϵ model contains a new formulation for turbulent viscosity. This is due to the fact that C_μ introduced in Equation 3.4 is no longer constant. The realizable k- ϵ can more accurately predicts the performance of flow involving rotation, boundary layer under strong adverse pressure gradients, separation and recirculation [10].

The transport equations for realizable k- ϵ model are given by Equation 3.5 and 3.6:

$$\frac{\partial(\rho k)}{\partial t} + \frac{\partial(\rho k u_j)}{\partial x_j} = \frac{\partial}{\partial x_j} \left[\left(\mu + \frac{\mu_t}{\sigma_k} \right) \frac{\partial k}{\partial x_j} \right] + G_k + G_b - \rho \epsilon - Y_M + S_k \quad (3.5)$$

$$\frac{\partial(\rho \epsilon)}{\partial t} + \frac{\partial(\rho \epsilon u_j)}{\partial x_j} = \frac{\partial}{\partial x_j} \left[\left(\mu + \frac{\mu_t}{\sigma_\epsilon} \right) \frac{\partial \epsilon}{\partial x_j} \right] + \rho C_1 S \epsilon - \rho C_2 \frac{\epsilon^2}{k + \sqrt{\nu \epsilon}} + C_{1\epsilon} \frac{\epsilon}{k} C_{3\epsilon} G_b + S_\epsilon \quad (3.6)$$

where

$$C_1 = \max[0.43, \frac{\eta_T}{\eta_T+5}], \eta_T = S_\epsilon^k, S = \sqrt{2S_{ij}S_{ij}}$$

In these equations, G_k represents the generation of turbulence kinetic energy due to the mean velocity gradients. G_b is the generation of turbulence kinetic energy due to buoyancy. Y_M represents the dissipation rate due to fluctuating dilatation in compressible flow. C_2 and $C_{1\epsilon}$ are model constants. σ_k and σ_ϵ are the turbulent Prandtl numbers for k - ϵ , respectively. S_k and S_ϵ are user-defined source terms.

The realizable k - ϵ turbulence model has been selected for all simulations. This is due to the fact that the realizable k - ϵ model is an improvement over the standard k - ϵ model with respect to prediction of swirling flows. The realizable k - ϵ offers largely same benefits and has similar application as RNG- k - ϵ . But one advantage is that it is possibly more accurate and easier to get convergence than the RNG- k - ϵ model [10].

3.3.2 Near wall modelling

Walls are the main source of vorticity and turbulence. Presence of walls usually gives rise to turbulent momentum/thermal boundary layer. Thus, it is necessary to have accurate near-wall modeling. For the near wall modelling there are two options [10]:

- i) Wall functions
- ii) Enhanced Wall Treatment (EWT)

In general, wall functions obey set of laws that serve as boundary conditions for momentum, energy, species and turbulence quantities. The EWT model combines the use of enhanced wall functions and a two-layer model [10]. It can calculate more accurately velocity, temperature, species mass fraction or turbulence if the near-wall mesh is fine to resolve the viscous sublayer. The mesh which has been used is fine enough in the near-wall zone. Further, this model is suitable for flow with complex near-wall phenomena. Thus, the EWT model has been used for all simulations.

3.4 Radiative heat transfer modelling

This section describes the radiation heat transfer which has been selected, along with the gas radiative property models utilized to calculate the absorption coefficient.

3.4.1 RTE and DO model

Radiation heat transfer is accounted for by solving the radiative heat transfer equation (RTE) given by the following equation [10]:

$$\frac{\partial I(\vec{r}, \hat{s})}{\partial s} = K_a(\vec{r}) \left(\frac{\sigma T^4}{\pi} - I(\vec{r}, \hat{s}) \right) \quad (3.7)$$

where I [$\frac{W}{m^2 \cdot sr}$] is the total radiation intensity and K_a [m^{-1}] is the absorption coefficient. The Equation 3.7 is a simplified expression for gaseous fuel combustion, where the value of scattering coefficient is $\sigma_s=0$ and refractive index is $n=1$. The discrete ordinate (DO) model solves the RTE in a finite number of solid angles. But the DO model is computationally expensive due to the fact that $8N_\theta N_\phi$ equations are solved where N_θ and N_ϕ are the number of subdivisions of $1/8$ of a sphere in the θ and ϕ spherical coordinates. In this report, the DO model has been used to solve above mentioned Equation 3.7 in all CFD simulations. This is because the DO model takes into account the effect of participating medium in combustion processes and is also applicable to all optical thicknesses. $N_\theta = N_\phi = 2$ subdivisions have been used for all simulations [10].

3.4.2 The four gas radiative property models used and compared

In order to compute the absorption coefficient in RTE, different gas radiative property models have been used. The four gas radiative property models which have been used in the air-fuel simulations and already described in chapter 2 are as follows:

- E-EWBM developed in this thesis.
- Default WSGGM (Smith et al., 1982).
- Refined air-fuel WSGGM (Yin, 2013).
- E-EWBM (Yan et al., 2015).

3.5 Reaction modelling

This section describes the reaction modelling of the flame, including the species model selected, different global combustion mechanisms and the turbulence-chemistry interaction model used.

3.5.1 Species modelling

Fluent can model species transport and reaction using several independent models. For this case the species transport approach has been selected, due to the fact that detailed chemistry is involved in the species transport approach. Thus, it leads to better temperature prediction. The species transport approach solves the conservation equations for convection, diffusion and reaction sources for multiple component species. One more advantage is that multiple chemical reactions may be specified to model simultaneously, with reactions occurring in the bulk flow, at wall or particle surfaces [10].

$$\frac{\partial(\rho Y_i)}{\partial t} + \nabla(\rho \vec{u} Y_i) = -\nabla(\rho \vec{J}_i) + R_i + S_i \quad (3.8)$$

This conservation equation describes the convection and diffusion of the local mass fraction of species Y_i , R_i is the rate of production by chemical reaction, and S_i is the rate of creation by addition from the dispersed phase and user-defined sources.

The diffusion flux \vec{J}_i occurs due to gradients of concentration and temperature. With turbulence, further accommodation is necessary because mixing must be explicitly included as a function of turbulence at small length scales. The diffusion flux \vec{J}_i is given by the Equation 3.9. Where $D_{i,m}$ is the mass diffusion coefficient and $D_{T,i}$ is the thermal diffusion coefficient. S_{ct} is the turbulent Schmidt number [10]:

$$\vec{J}_i = -(\rho D_{i,m} + \frac{\mu_t}{S_{ct}}) \nabla Y_i - D_{T,i} \frac{\nabla T}{T} \quad (3.9)$$

Naturally, species transport introduces a number of significant physical effects into the system, including diffusion, enthalpy transport and temperature gradients.

3.5.2 The four global combustion mechanisms used and compared

Combustion occurs due a number of elementary reactions that lead to overall reaction. A number of elementary reactions together constitute the reaction mechanism. Detailed mechanism for the combustion of CH_4 can include thousands of elementary reactions. Detailed mechanism consists of series of elementary reactions which makes it computational prohibitive in the CFD simulations. This is because detailed mechanism leads the CFD solver to solve a large system of differential equations associated with such a mechanism when reaction kinetics are included. Thus, global and quasi global mechanisms are in use to model overall behaviour of the detailed reaction mechanism with a reduced set of reactions [11].

The 1-step reaction mechanism is given in Table 3.8, with the default values from Fluent.

	Reactions	Rate equations[$\text{kmol}/(\text{m}^3 \cdot \text{s})$]	A	b	E
1	$\text{CH}_4 + 2\text{O}_2 \rightarrow \text{CO}_2 + 2\text{H}_2\text{O}$	$[\text{CH}_4]^{0.2}[\text{O}_2]^{1.3}$	2.119e11	0	2.027e08

TABLE 3.8: 1-step reaction mechanism for CH_4

	Reactions	Rate equations[$\text{kmol}/(\text{m}^3 \cdot \text{s})$]	A	b	E
1	$\text{CH}_4 + 1.5\text{O}_2 \rightarrow \text{CO} + 2\text{H}_2\text{O}$	$[\text{CH}_4]^{0.7}[\text{O}_2]^{0.8}$	5.01e11	0	2.00e08
2	$\text{CO} + 0.5\text{O}_2 \rightarrow \text{CO}_2$	$[\text{CO}][\text{O}_2]^{0.25}[\text{H}_2\text{O}]^{0.5}$	2.23e12	0	1.70e08
3	$\text{CO}_2 \rightarrow \text{CO} + 0.5\text{O}_2$	$[\text{CO}_2]$	5.00e08	0	1.70e08

TABLE 3.9: Original WD 2-step reaction mechanism for CH_4 [1]

WD: the Westbrook and Dryer two-step reaction mechanism. The WD mechanism consists of two reactions, where the second step is oxidation of CO to CO_2 is reversible. Table 3.9 shows the reactions and their kinetic data. The rate constant for the first and second reactions originate from Dryer and Glassman (1973), in which high temperature oxidation of CO and CH_4 was studied under fuel lean conditions in a turbulent flow reactor. Later, Westbrook and Dryer introduced the reverse reaction for CO_2 decomposition in order to account for proper heat of reaction [1]. For grid-independency study the WD 2-step reaction is used, which has been described briefly in a subsequent section of this chapter.

JL four step: the 4-step global mechanisms developed by Jones and Lindstedt for the combustion of alkane hydrocarbons up to butane in mixtures with air. The scheme includes two fuel breakdown reactions, and in order to derive initial estimates of the forms of the rate expressions an assumption of equilibrium have been made [1].

The final kinetic parameters of the resulting rate equations have been determined by comparison with experimental data for premixed methane and propane flames, along with diffusion flame data for a methane-air flame. The resulting schemes have been found to combine good agreement with experimental data for a range of flame parameters such as flame speed, flame thickness and species profiles.

	Reactions	Rate equations[$kmol/(m^3 \cdot s)$]	A	b	E
1	$CH_4 + 0.5O_2 \rightarrow CO + 2H_2$	$[CH_4]^{0.5}[O_2]^{1.25}$	4.40e11	0	1.26e08
2	$CH_4 + H_2O \rightarrow CO + 3H_2$	$[CH_4][H_2O]$	3.00e08	0	1.26e08
3	$H_2 + 0.5O_2 \rightarrow H_2O$	$[H_2]^{0.25}[O_2]^{1.5}$	6.80e15	-1	1.67e08
4	$H_2O \rightarrow H_2 + 0.5O_2$	$[H_2]^{-0.75}[O_2][H_2O]$	1.25e17	-0.877	4.09e08
5	$CO + H_2O \leftrightarrow CO_2 + H_2$	$[CO][H_2O]$	2.75e09	0	8.40e07

TABLE 3.10: Original JL 4-step reaction mechanism for CH_4 [1]

The original JL 4-step reaction global mechanism is given in Table 3.10. All the kinetic data is taken from reference [1]. However, the mentioned reference has taken the reverse reaction of H_2 oxidation. This is due to the fact that consideration to derive new kinetic data for separate reverse reaction is that $H_2 + 0.5O_2 \leftrightarrow H_2O$ is a global reaction and the forward reaction orders do not follow stoichiometry. As a result, the reverse reaction constant may not be simply determined from the equilibrium constant and forward rate constant. It can be seen from Table 3.10 that the derived kinetic rate data for the reverse reaction $H_2O \rightarrow 0.5O_2 + H_2$ involves a negative H_2 concentration dependence i.e -0.75, which induces some numerical difficulties [1]. Further, with this air-fuel case, some tests were made by using the original JL 4-step mechanism coupled with the Eddy Dissipation Concept (EDC), but due to stiff chemistry, it was not possible to get fully converged solution.

JL-1: in order to overcome the above mentioned problem a refined JL-4 step reaction mechanism has been used in this thesis.

There are two changes comparing with the JL mechanism: one for H_2 oxidation reaction and the other one for CO oxidation reaction, as shown in Table 3.11. The first two

	Reactions	Rate equations[$kmol/(m^3 \cdot s)$]	A	b	E
1	$CH_4 + 0.5O_2 \rightarrow CO + 2H_2$	$[CH_4]^{0.5}[O_2]^{1.25}$	4.40e11	0	1.26e08
2	$CH_4 + H_2O \rightarrow CO + 3H_2$	$[CH_4][H_2O]$	3.00e08	0	1.26e08
3	$H_2 + 0.5O_2 \rightarrow H_2O$	$[H_2][O_2]^{0.5}$	7.90e10	0	1.46e08
4	$CO + 0.5O_2 \rightarrow CO_2$	$[CO][O_2]^{0.3}[H_2O]^{0.5}$	2.50e08	0	6.69e07

TABLE 3.11: JL-1 4-step reaction mechanism for CH_4 [1]

reactions are precisely same as those in JL 4-step mechanism. The third reaction (H_2 oxidation) is replaced by the global kinetic model. However, in order to predict CO concentration reasonably, the pre-exponential factor of H_2 oxidation was fitted to the simulation results with detailed chemistry from the Sandia Flame D case. A global reaction rate proposed by Hottel et al. (1965) is applied for CO oxidation in the fourth reaction. All reactions are treated as irreversible in this refined global mechanism [1].

In this work one more reaction mechanism, i.e. JL-Refined (Yan et al., 2015), has been used [7]. The reaction mechanism is given in Table 3.12. The results of all those above mentioned reactions mechanism have been discussed in section 3.7.

Species	Reactions	Rate equations[$kmol/(m^3 \cdot s)$]	A	b	E
1	$CH_4 + 0.5O_2 \rightarrow CO + 2H_2$	$[CH_4]^{0.5}[O_2]^{1.25}$	4.40e14	0	1.99e08
2	$CH_4 + H_2O \rightarrow CO + 3H_2$	$[CH_4][H_2O]$	3.00e11	0	1.99e08
3	$H_2 + 0.5O_2 \rightarrow H_2O$	$[H_2]^{0.25}[O_2]^{1.5}$	2.50e19	-1	2.66e08
4	$CO + H_2O \rightarrow CO_2 + H_2$	$[CO][H_2O]$	2.75e12	0	1.33e08

TABLE 3.12: JL-Refined (Yan et al., 2015) 4-step reaction mechanism for CH_4 [7]

3.5.3 Turbulence-chemistry interaction modelling

The turbulence-chemistry interaction models indicates which model is to be used for turbulence-chemistry interaction when the Species Transport model with volumetric reactions is used. Volumetric reactions enables the calculation of reacting flow using the finite rate [10]. In order to model the interaction of chemistry with turbulence Eddy Dissipation Concept (EDC) has been selected. This is due to the following reasons:

- 1) EDC models turbulence-chemistry interaction with detailed chemical mechanisms, whereas model such as Laminar Finite-Rate neglects turbulence-chemistry interaction [10].

2) EDC model attempts to incorporate the significances of fine structure in a turbulent reacting flow. This sounds reasonable since combustion is more likely to occur at fine structure [10].

3) When more detailed combustion mechanism is considered, the temperature peak is more reasonably predicted. More energy is tied up on chemical bonds at the expense of sensible enthalpy [10].

4) Further, models such as Eddy-Dissipation (ED) is suitable for fast chemistry and assumes that chemical reactions occurs much faster than turbulence ($Da \gg 1$), whereas the EDC model consider mixing and kinetic time scale are comparable ($Da \sim 1$). Da = Damkohler number, defined as the ratio of characteristic turbulence time scale to the characteristic chemical/chemistry time scale [10].

5) ED only models turbulent reaction rates and does not include kinetic reaction rates. The reaction mechanisms discussed above employ the Arrhenius expression to model reaction rates. The ED model cannot predict intermediate species and is ill suited for the 2-step and 4-step reaction mechanisms [10].

Eddy Dissipation Concept has been used for all simulations with the WD 2-step and JL 4-step reaction mechanism, whereas for the simulation with the one step reaction mechanism the ED model has been used. This is because the chemistry with one step is not in detail, so when the EDC model was used with the one step reaction mechanism, achieving a converged solution was an issue.

3.6 Properties and solution methods/control

This section explains the material properties, solution methods and solution controls which have been used in all simulations.

3.6.1 Material properties

The material properties given in Table 3.13 have been used. The constant pressure specific heat capacity c_p for the gas mixture is determined from Equation 3.10 as the

sum of the mass fraction weighted c_p of each species. The expression c_p for species is given by the expression [11]:

$$c_p = \sum_{i=1}^N Y_i c_{p,i} \quad (3.10)$$

where $c_{p,i}$ is the constant pressure specific heat capacity of species i and Y_i is the piecewise polynomial coefficient.

$c_{p,i}$ is determined from the polynomial functions of temperature. The default polynomial coefficients provided for CH₄ are used for the fuel.

Property	Value
Thermal conductivity $k[\frac{W}{m \cdot K}]$	0.0454
Viscosity $\mu[\frac{kg}{m \cdot s}]$	1.72e-05
Mass diffusion coefficient $D_{i,m}[\frac{m^2}{s}]$	2.88e-05
Scattering coefficients $\sigma_s[m^{-1}]$	0
Refractive index n	1

TABLE 3.13: Material properties used in all air-fuel CFD simulations [6]

The laminar thermal conductivity $k[\frac{W}{m \cdot K}]$, mass diffusion coefficient $D_{i,m} [\frac{m^2}{s}]$ and the viscosity $\mu[\frac{kg}{m \cdot s}]$ are the default values given by Fluent. The flow is turbulent and the turbulent properties corresponding to laminar properties provided by Fluent as given in Table 3.13 are dominant, thus detailed modelling of the laminar properties is assumed to be unnecessary [11]. The absorption coefficient is determined using the E-EWBM as described in section 2.4.

3.6.2 Solution methods

The Reynolds-Averaged Navier Stokes (RANS) equations and models discussed above have been solved using the Fluent V15 CFD software. Fluent employs the finite volume method to solve the RANS partial differential equations. The COUPLED pressure velocity coupling has been used in all simulations. This solver offers some advantages over the pressure based segregated algorithm. The pressure-based coupled algorithm obtains a more robust and efficient single phase implementation for steady-state flows. In all cases the least square cell based method has been used for evaluation of gradients and derivatives. This is due to the fact that more accurate flow solution is achieved in

the least square cell based method than Green-Gauss cell based gradients as reported by reference [10]. In the least square cell based method the solution is assumed to vary linearly, thus resulting in an accurate flow solution. The first order upwind discretization scheme has been used in all simulations. However, with the second-order discretization scheme the accuracy is better than with the first order scheme [10]. But with the second order upwind scheme achieving a converged solution turned out to be a difficult and time consuming task. Thus, for all simulations the first order upwind discretization scheme has been used because it is one of the simplest and most stable discretization schemes.

3.6.3 Solution controls

Table 3.14 shows the relaxation factors which have been used in the simulations. The amount of relaxation factors used can be critical. Too much leads to numerical instabilities, while too little slows down convergence. Similarly a poorly chosen convergence criteria can lead to either poor results (when too loose) or excessive computational time [11]. Default values of relaxation factors have been used in all simulations.

Equation	Relaxation factors
Pressure	0.5
Momentum	0.5
Density	1
Body forces	1
Swirl velocity	0.75
Turbulent Kinetic Energy	0.75
Turbulent Dissipation rate	0.75
Turbulent Viscosity	1
Energy	0.75
Discrete Ordinates	1

TABLE 3.14: Relaxation factors employed in simulation for air-fuel simulations [6]

3.7 Results and discussion

In this section, the CFD results under air-fuel conditions are presented and discussed. Firstly, the effect of mesh has been evaluated to ensure that the solution is mesh independent. Secondly, the effect of the four radiative property models used is presented and

discussed. Lastly, the effect of the four global combustion mechanisms used is presented and explained.

3.7.1 Effect of mesh

This section is about grid-independency study. By varying the mesh density, the results, i.e., temperature, axial velocity and O₂ mass fraction, have been compared. The mesh considered to be fine enough to attain grid-independent results is selected for all further simulations.

The furnace is a 2D axi-symmetric furnace as discussed in above section. The mesh with N = 9784 cells is taken from Tutorial 17 of ANSYS Fluent. The quality of the mesh is given in Table 3.15.

It is expected that the truncation error decreases as the number of mesh cells increases [11]. Meshes with increasing number of cells have been constructed for the purpose of mesh independence study. The meshes are designated from N to 16N.

Mesh	cells	Minimum angle	Maximum aspect ratio	Minimum orthogonal quality
N	9784	44.11 °	50.1114	6.99472e-01
4N	39136	44.11 °	50.1716	6.98404e-01
16N	156544	44.11 °	50.2006	6.97396e-01

TABLE 3.15: Quality parameters of the meshes N, 4N and 16N for 2D-axisymmetric furnace

For the mesh independency test, the simulations were performed with the two step reaction mechanism in Fluent. Detailed reaction mechanisms, models and boundary conditions used in simulation have already been discussed in previous sections.

The settings and convergence summary are shown in Table 3.16.

To perform the mesh independency test, three variables have been used: temperature, axial velocity and O₂ mass fraction. In Figures 3.4 and 3.5 the radial profiles of these variables have been plotted at 27 mm from the quartz exit.

From the figures it can be seen that the calculation with the three meshes are close to each other. Further, from Figure 3.4A and 3.4B it can be seen that the temperature curve and axial velocity for all three meshes are same across the entire radial position.

Case	Main settings	Net flow rate (kg/s)	Net HT rate (W) HT p outlet (kW)
Case 0	N cells mesh (9784 cells) WSGGM (Smith et al.) 2-step reaction mechanism	$9.27 \cdot 10^{-8}$ kg/s	920.5 W 158.37 kW
Case 1-1	4N cells mesh (39136 cells) WSGGM (Smith et al.) 2-step reaction mechanism	$4.86 \cdot 10^{-7}$ kg/s	1507.26 W 162.7 kW
Case 1-2	16N cells mesh (156544 cells) WSGGM (Smith et al.) 2-step reaction mechanism	$5.35 \cdot 10^{-7}$ kg/s	563.69 W 158.47 kW

TABLE 3.16: Convergence summary for the effect of mesh

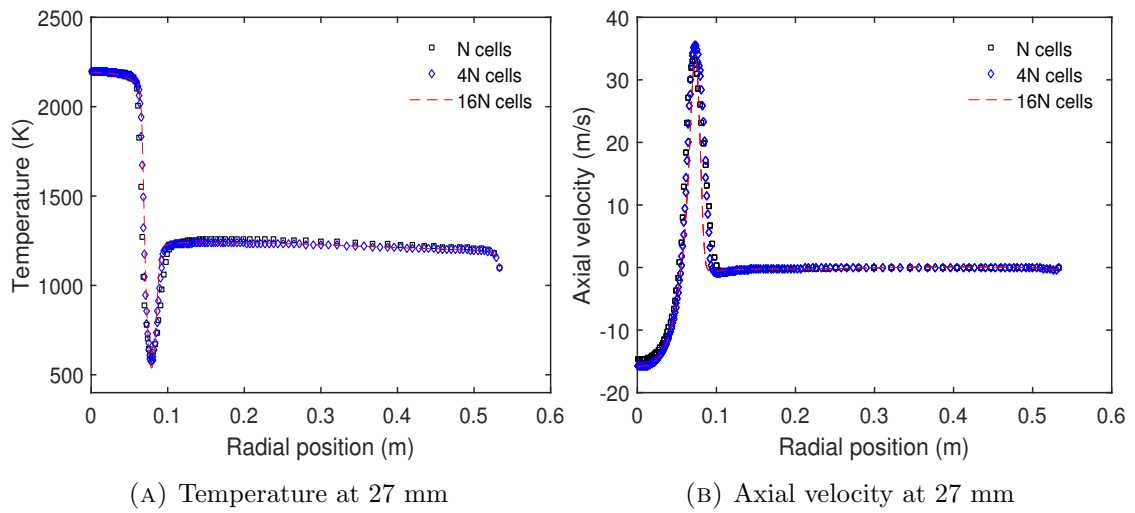
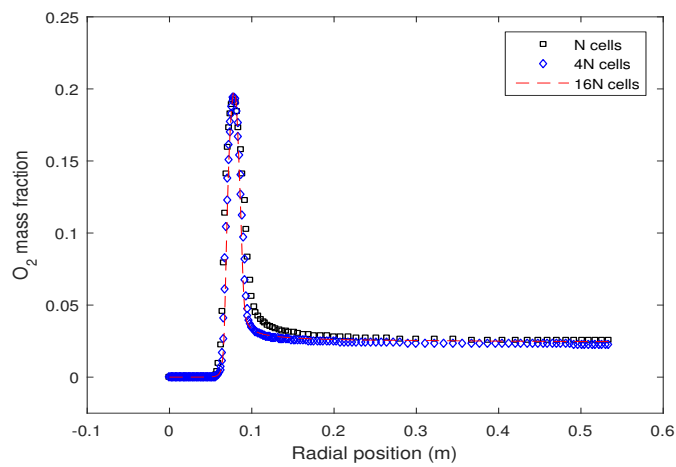


FIGURE 3.4: Temperature and axial velocity vs radial position at 27 mm from the quarl exit

FIGURE 3.5: O₂ mass fraction vs radial position at 27 mm from the quarl exit

In Figure 3.5 very slight variation can be seen in the O_2 mass fraction after radial position of 0.1 m, but this variation diminishes after certain point and the reading for all three meshes are almost same. Thus, mesh N is chosen in this work to do the following numerical simulations and the grid resolution used is found to be sufficient to obtain mesh independent results.

Further, Yan et al. (2015) have also performed the mesh independency test for the same furnace. In their work they compared the three parameters, i.e., temperature, axial velocity and O_2 mass fraction at partition 27 mm from the quarl exit. They concluded that the mesh with 9784 quadrilateral cells are enough to produce mesh independent solution [7].

Thus, the mesh with 9874 quadrilateral cells is used for all the simulations of this furnace.

3.7.2 Effect of gas radiative property models

The main goal of this section is to demonstrate the applicability of the E-EWBM developed in this thesis in air-fuel combustion. A sensitivity analysis is done in order to compare the effect of the E-EWBM with other radiation property models and the experimental data.

Numerical simulations have been done with four different radiative property models. These are the E-EWBM developed in this thesis, the default WSGGM (Smith et al., 1982), the refined air-fuel WSGGM (Yin, 2013) and the E-EWBM (Yan et al., 2015).

Table 3.17 gives a description of the main settings together with the overall convergence check summary. In this table the imbalances of mass flow rate and heat transfer rate can be assessed, in order to show that the simulations are well converged. The net imbalances are a small fraction of the total flux through the furnace.

In order to compare the effect of different radiative property models, the CFD results on four measuring lines along the radial position from the centerline of the furnace (located at 27 mm, 109 mm, 343 mm and 432 mm downstream from the quarl exit) have been plotted. The plotted parameters for which the experimental data is available are gas temperature, axial velocity and O_2 mass fraction.

Case	Main settings	Net flow rate (kg/s)	Net HT rate (W) HT p outlet (kW)
Case 0	N cells mesh (9784 cells) E-EWBM (this thesis) JL-1 reaction mechanism	$2.17 \cdot 10^{-7}$ kg/s	1148.91 W 164.5 kW
Case 2-1	N cells mesh (9784 cells) WSGGM (Smith et al.) JL-1 reaction mechanism	$3.2 \cdot 10^{-7}$ kg/s	1091.95 W 162.7 kW
Case 2-2	N cells mesh (9784 cells) WSGGM (Yin) JL-1 reaction mechanism	$3.216 \cdot 10^{-7}$ kg/s	1049.279 W 163.357 kW
Case 2-3	N cells mesh (9784 cells) E-EWBM (Yan et al.) JL-1 reaction mechanism	$3.46 \cdot 10^{-7}$ kg/s	707.59 W 163.38 kW

TABLE 3.17: Convergence summary for the effect of gas radiative property models

Furthermore, additional radiation parameters are presented, namely the absorption coefficient and radiation source term. Figure 3.6 shows the absorption coefficient as function of radial distance at the four locations from the quarl exit.

From Figure 3.6, it can be seen that the absorption coefficient calculated with both E-EWBM is higher than that predicted by both WSGGM near the centerline. This is due to the fact that both E-EWBM take into account the effect of CO_2 , H_2O , CH_4 and CO on absorption coefficient, while both WSGGM only account for the contribution of CO_2 and H_2O . Higher absorption coefficient leads to an increase in the radiation heat transfer [7]. The radiation heat transfer rate across all the furnace walls is reported in Table 3.18. It can be seen that the radiation heat transfer rate predicted by both E-EWBM is greater than that calculated by both WSGGM.

Radiation model	Radiation heat transfer rate (kW)
E-EWBM (this thesis)	129.3
WSGGM (Smith et al., 1982)	128.2
WSGGM (Yin, 2013)	128.7
E-EWBM (Yan et al., 2015)	131.1

TABLE 3.18: Comparison of radiation heat transfer rate with different radiation models

Further, relative differences can be seen between the absorption coefficient evaluated by the E-EWBM developed in this thesis and that predicted by the E-EWBM developed by Yan et al. (2015). This is somehow expected since the parameters of the latter model are fitted using the Line by Line method with the HITEMP-2010 spectral database.

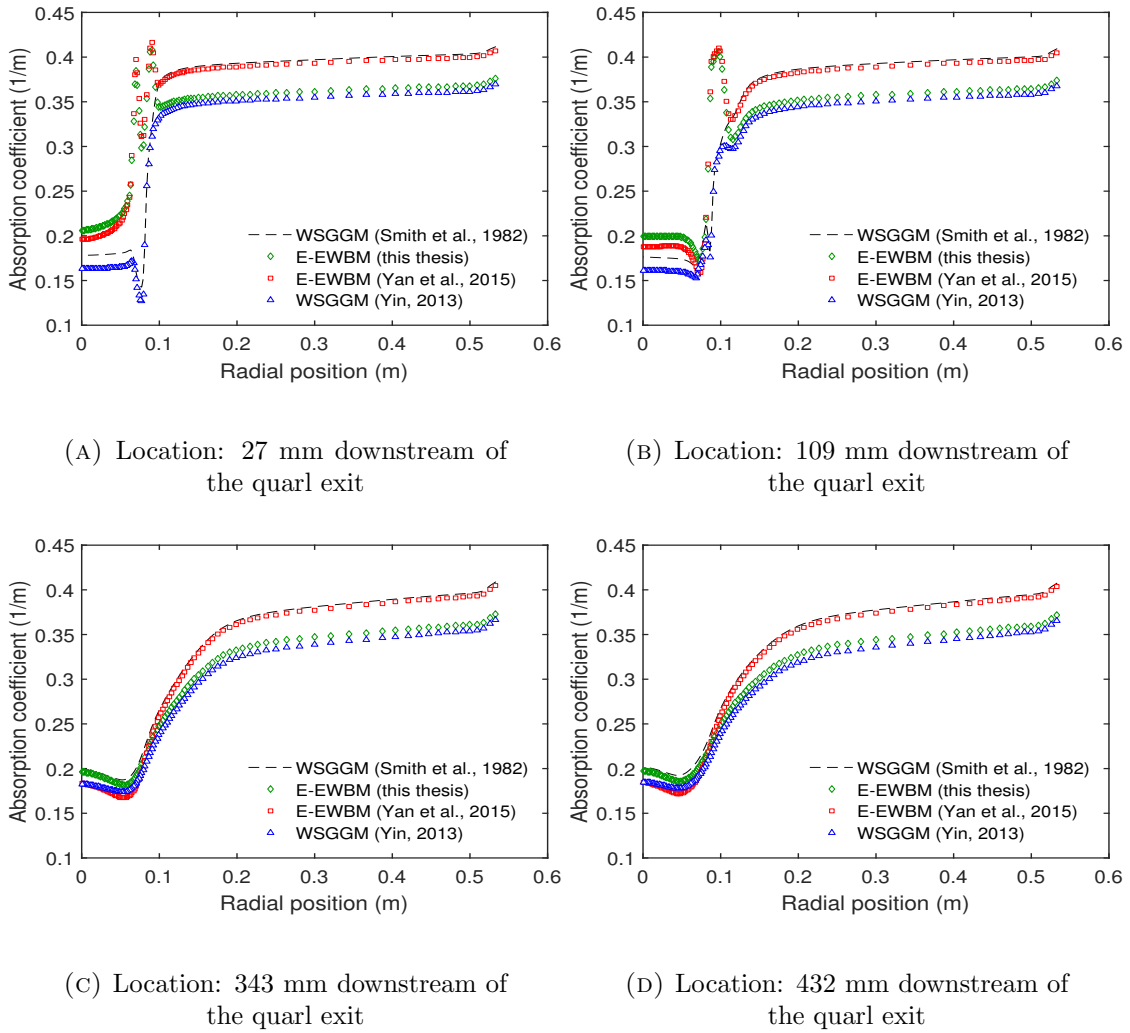


FIGURE 3.6: Radial distribution profiles of absorption coefficient to study the effect of radiation models

Also, variations in the absorption coefficient can be seen comparing the default WSGGM with the Yin WSGGM, because the latter is more refined.

Figure 3.7 shows the radiation source term as a function of radial distance at the four locations from the quarl exit. The radiation heat source is given by $-div[\vec{q}_{rad}(\vec{r})] \equiv k_a(\vec{r}) [G(\vec{r}) - 4\sigma T_g^4(\vec{r})]$, where $k_a(\vec{r})$, $G(\vec{r})$, $T_g(\vec{r})$ are the absorption coefficient, incident radiation and gas temperature respectively at the current location, while σ is the Stefan-Boltzmann constant.

A temperature contour and the temperature profiles at the four locations are given in Figures 3.8 and 3.9, respectively. In the latter, the four radiation models are compared along with the experimental data.

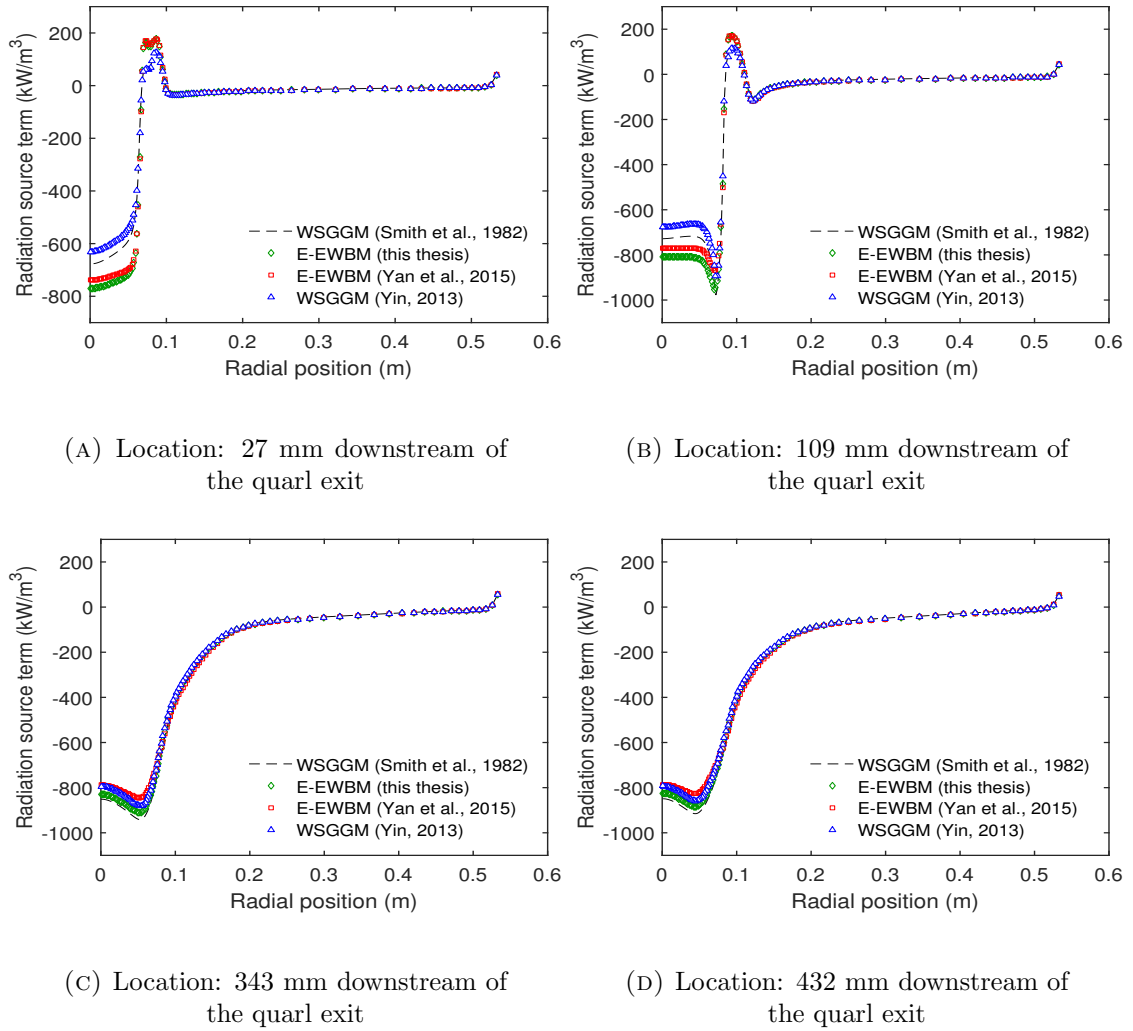


FIGURE 3.7: Radial distribution profiles of radiation source term

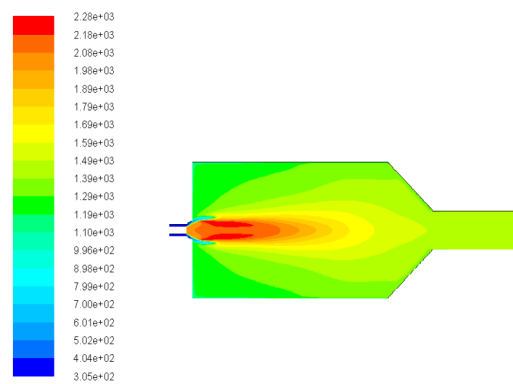


FIGURE 3.8: Contour of gas temperature using the developed E-EWBM

From Figure 3.9, it can be seen that the temperature predicted by the simulation with the E-EWBM developed in this work is close to that predicted by the default WSGGM. The same occurs with the other models under comparison. This is expected because

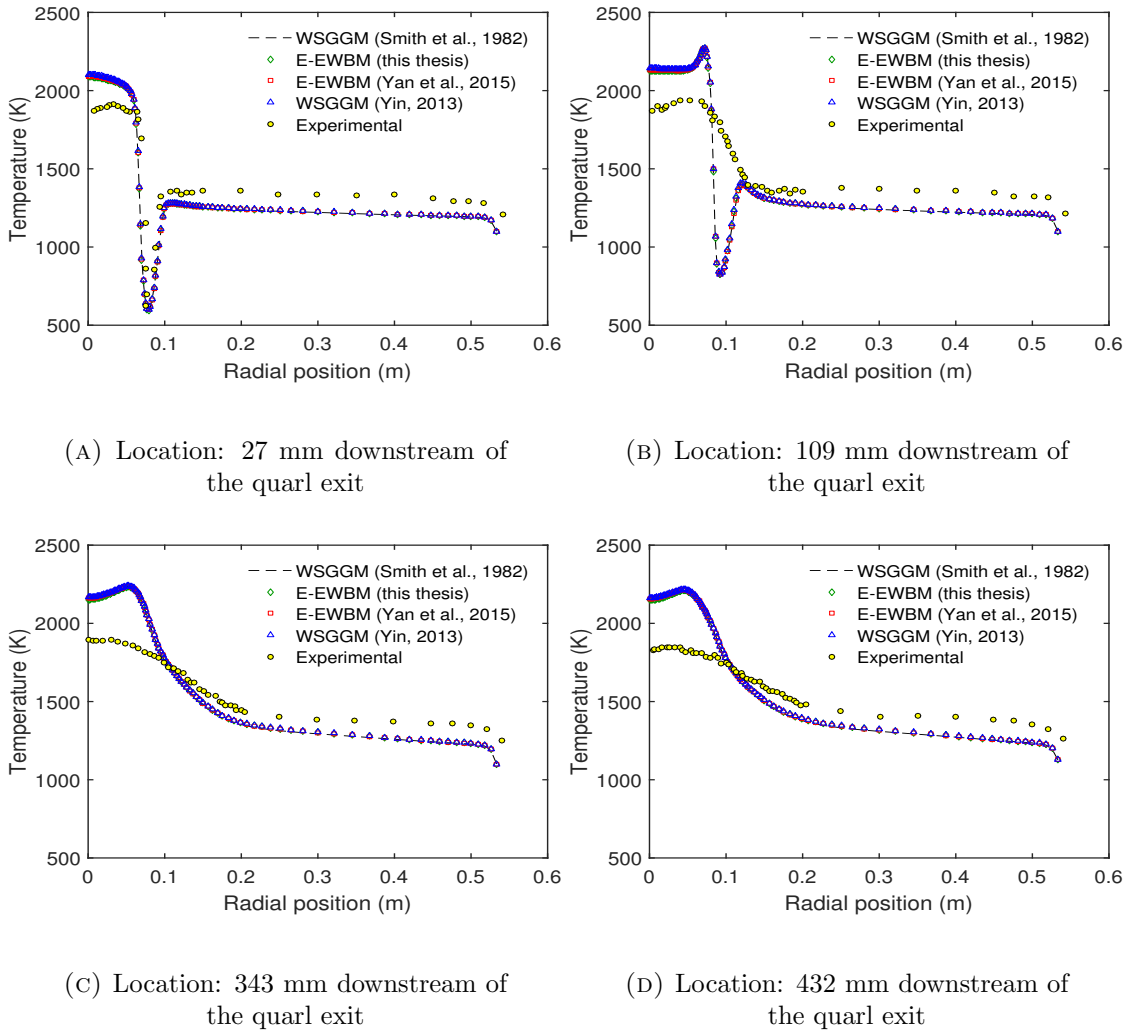


FIGURE 3.9: Radial distribution profiles of temperature to study the effect of radiation models

a small-scale furnace is being used for simulation, with a domain-based beam length around 0.72 m. For instance, slight differences in the peak temperature can be observed comparing the value predicted by the four radiation models, as given in Table 3.19.

Radiation model	Peak temperature (K)
E-EWBM (this thesis)	2282.5
WSGGM (Smith et al., 1982)	2280.96
WSGGM (Yin, 2013)	2283.08
E-EWBM (Yan et al., 2015)	2282.38

TABLE 3.19: Comparison of peak temperature with different radiation models

Yan et al. (2015) performed the CFD simulations comparing their E-EWBM with the default WSGGM [7]. They used the same furnace and similar operational conditions as in this work. The temperature obtained with the default WSGGM in this work and the

temperature predicted by Yan et al with the default WSGGM in their work is similar. Some deviation between the simulation and experimental data, as observed especially near the centerline, is expected because the problem was modeled as an axi-symmetric 2D representation of an inherently 3D problem [5].

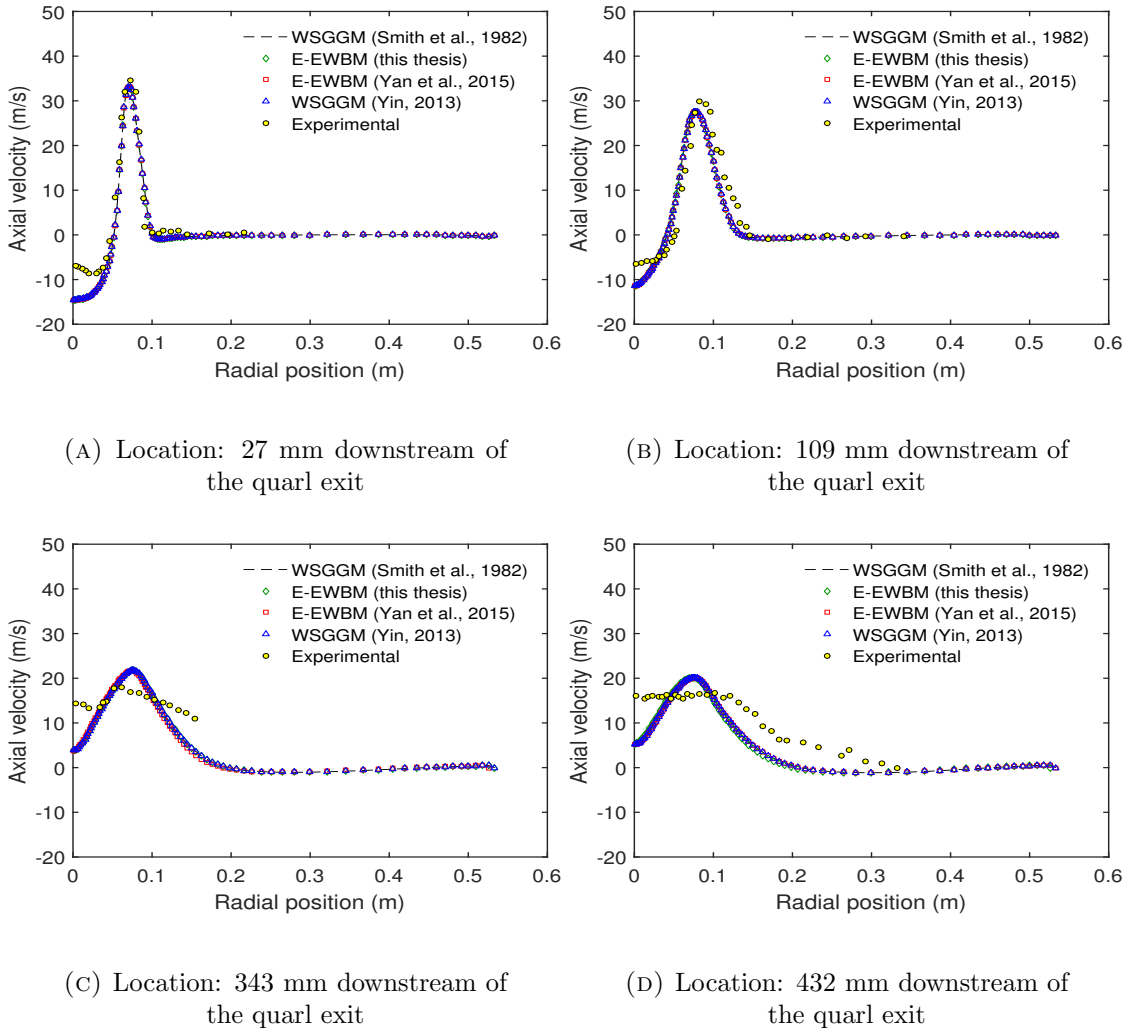


FIGURE 3.10: Radial distribution profiles of axial velocity to study the effect of radiation models

Figure 3.10 shows the axial velocity profiles at the four locations. From Figure 3.10, it can be observed that the axial velocity predicted is similar for the radiation models in such a small-scale furnace. Further, the axial velocity is in good agreement with the experimental data. Near the centerline at 27 mm and 109 mm, the counter flow (negative axial velocity) is surrounded by a relatively high speed flow injection due to the swirl velocity of the inlet flow [7]. Thus, a peak of axial velocity appears in the radial position of 0.1 m from the furnace centerline.

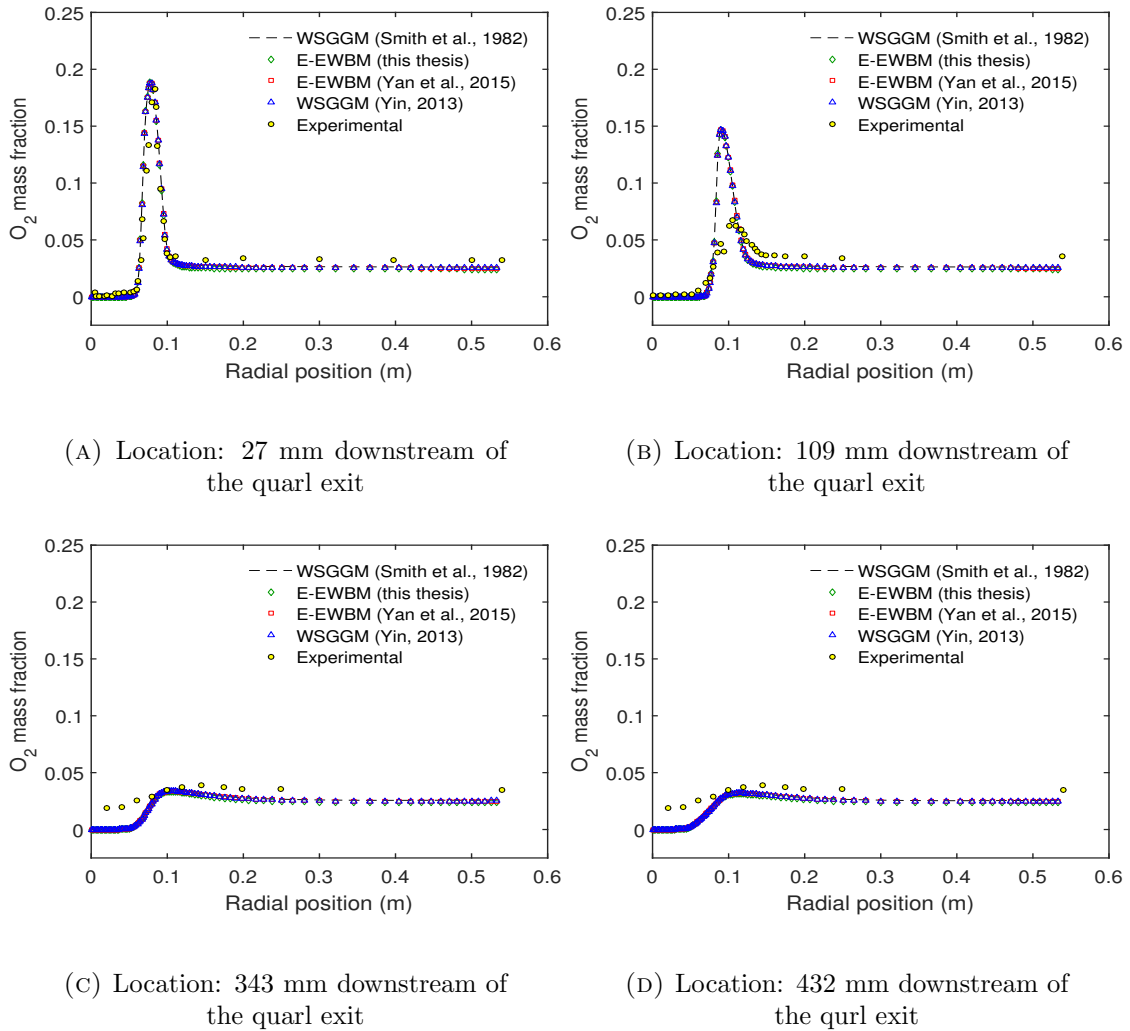


FIGURE 3.11: Radial distribution profiles of O_2 mass fraction to study the effect of radiation models

In Figure 3.11, the profiles of O_2 mass fraction are given at the four locations. As it can be observed from Figure 3.11, the radiative property model used does not lead to remarkable differences for the O_2 mass fraction. Moreover, it can be seen that the oxygen mass fraction is the lowest in the natural gas flame and highest in the injection flow, especially at the locations 27 mm and 109 mm from the quarl exit [7]. This can be explained according to the combustion physics occurring in the furnace. The injected air is led to the counter flow area due to the pressure difference between the outside and inside of the injection. Then, the injected air is heated to a very high temperature and is consumed rapidly in the natural gas flame [7].

In conclusion, the applicability of the new generic E-EWBM developed in air-fuel combustion is proved. It leads to a more reliable result of radiative properties such as the

absorption coefficient.

3.7.3 Effect of global combustion mechanisms

The effect of different combustion reaction mechanisms will be discussed, namely the 1-step, the WD 2-step, the JL-1 4-step and the 4-step reaction mechanism used in the Yan et al. (2015) work. Table 3.20 gives a description of the main settings together with the overall convergence check summary.

Case	Main settings	Net flow rate (kg/s)	Net HT rate (W) HT p outlet (kW)
Case 0	N cells mesh (9784 cells) E-EWBM (this thesis) JL-1 4-step reaction mechanism EDC	$2.17 \cdot 10^{-7}$ kg/s	1148.91 W 164.5 kW
Case 3-1	N cells mesh (9784 cells) E-EWBM (this thesis) 1-step reaction mechanism ED	$1.81 \cdot 10^{-7}$ kg/s	1922.47 W 156.58 kW
Case 3-2	N cells mesh (9784 cells) E-EWBM (this thesis) 2-step reaction mechanism EDC	$5.897 \cdot 10^{-8}$ kg/s	690.261 W 158.925 kW
Case 3-3	N cells mesh (9784 cells) E-EWBM (this thesis) Yan et al. reaction mechanism EDC	$6.41 \cdot 10^{-8}$ kg/s	25.72 W 161.09 kW

TABLE 3.20: Convergence summary for the effect of reaction mechanisms

In order to compare the effect of the four different reaction mechanisms, the results are presented on four measuring lines along the radial position from the centerline of the furnace, located at 27 mm, 109 mm, 343 mm and 432 mm downstream from the quarl exit.

In Figure 3.12, the radial temperature profiles are plotted. It can be seen that the 4-step reaction mechanisms predict lower temperature than the 1-step and 2-step reaction mechanisms near the center line. Thus, the temperature predicted by the 4-step mechanisms is closer to the experimental data. This is because the 4-step reaction mechanisms approach near to full dissociation. This is consequence of the species of dissociation, in general having a higher enthalpy of formation than ideal products [11].

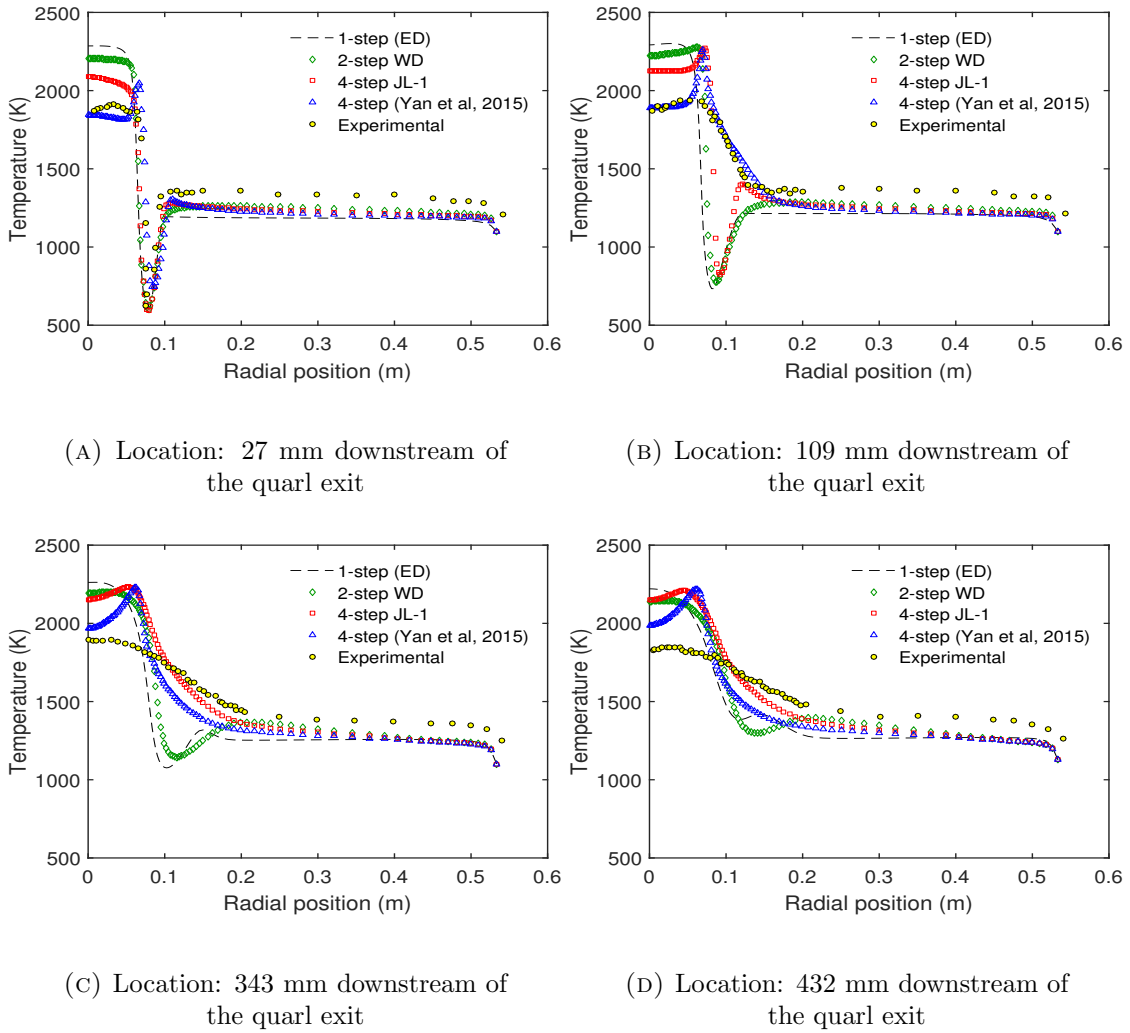


FIGURE 3.12: Radial distribution profiles of temperature to study the effect of reaction mechanisms

All simulations overpredict temperature near the centerline, except the Yan et al. (2015) reaction mechanism. At 27 mm and 109 mm, the temperature predicted with this reaction mechanism is in good agreement with the experimental data. In Table 3.21, the peak temperature for different reaction mechanisms is shown.

Reaction mechanisms	Peak temperature (K)
1-step (ED)	2301.057
2-step WD	2285.461
4-step JL-1	2282.5
4-step (Yan et al., 2015)	2272.792

TABLE 3.21: Comparison of peak temperature with different reaction mechanisms

In Figure 3.13 the radial distribution profiles of axial velocity are shown. It can be seen

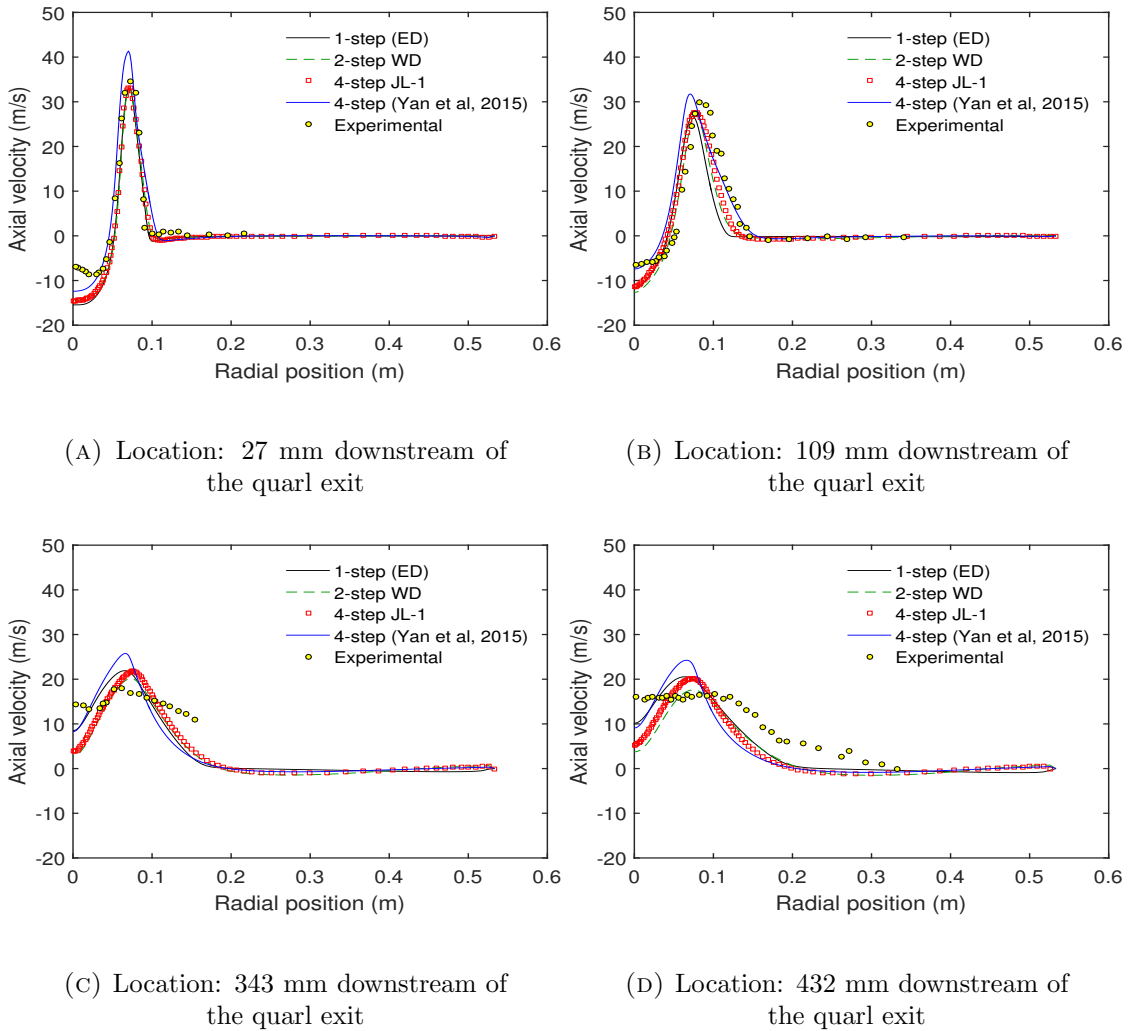


FIGURE 3.13: Radial distribution profiles of axial velocity to study the effect of reaction mechanisms

that the axial velocity predicted by the simulations are quite close to experimental data. At all locations downstream from the quarl exit, it can be observed a higher peak for the simulation with the reaction mechanism used by Yan et al. (2015).

In Figure 3.14 the radial distribution profiles of O_2 mass fraction are shown. One can observe that at 27 mm, the four different reaction mechanisms yield similar peak of O_2 mass fraction and it is close to the experimental data. But at location 109 mm, the Yan et al. (2015) reaction mechanism is producing lower values in the peak, leading to better agreement with the experimental data, while the other reaction mechanisms are over-predicting the O_2 mass fraction. Furthermore, as can be seen especially at locations 109 mm, 343 mm and 432 mm, the JL-1 reaction mechanism produces better results for O_2 than the 1-step and 2-step, due to the inclusion of H_2 oxidation.

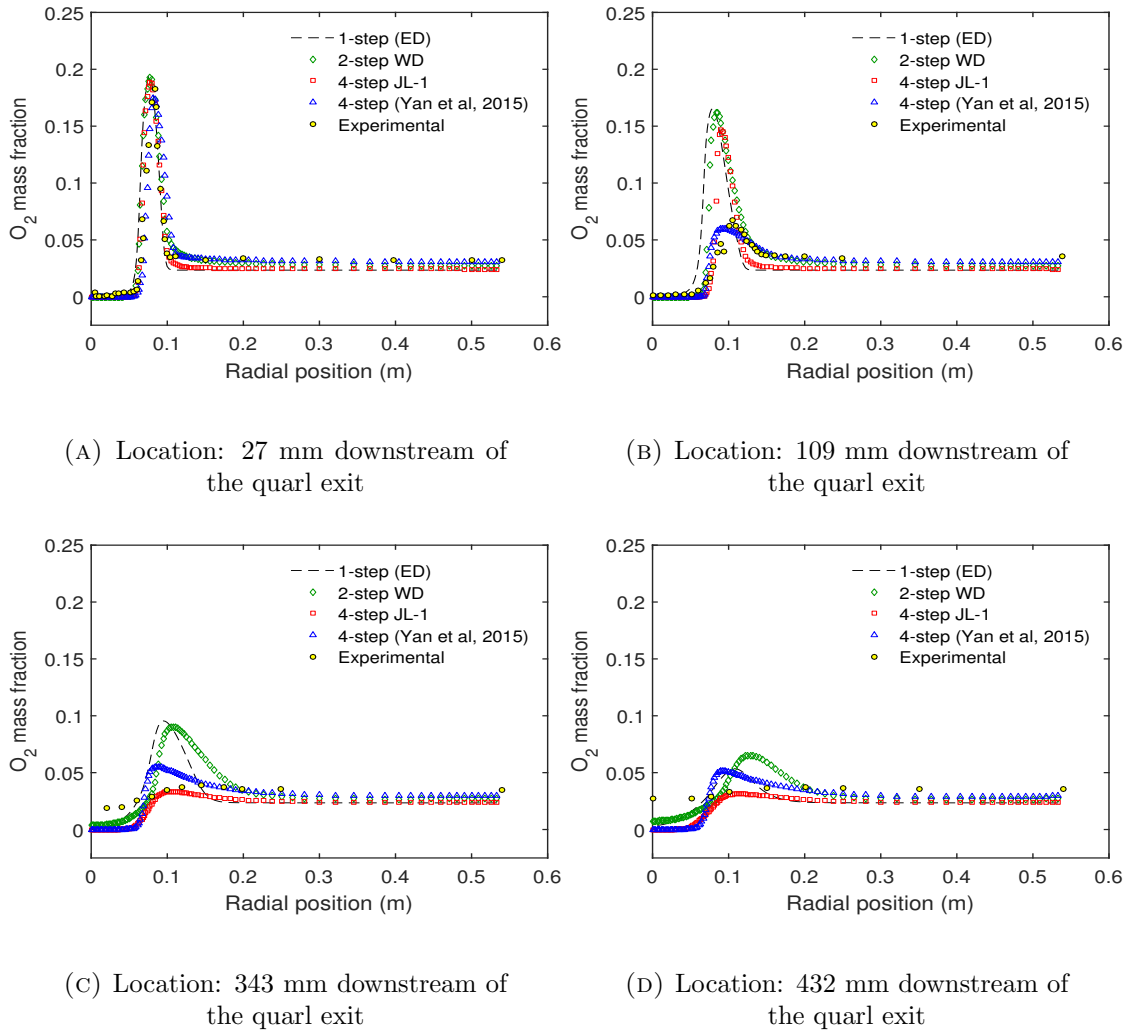
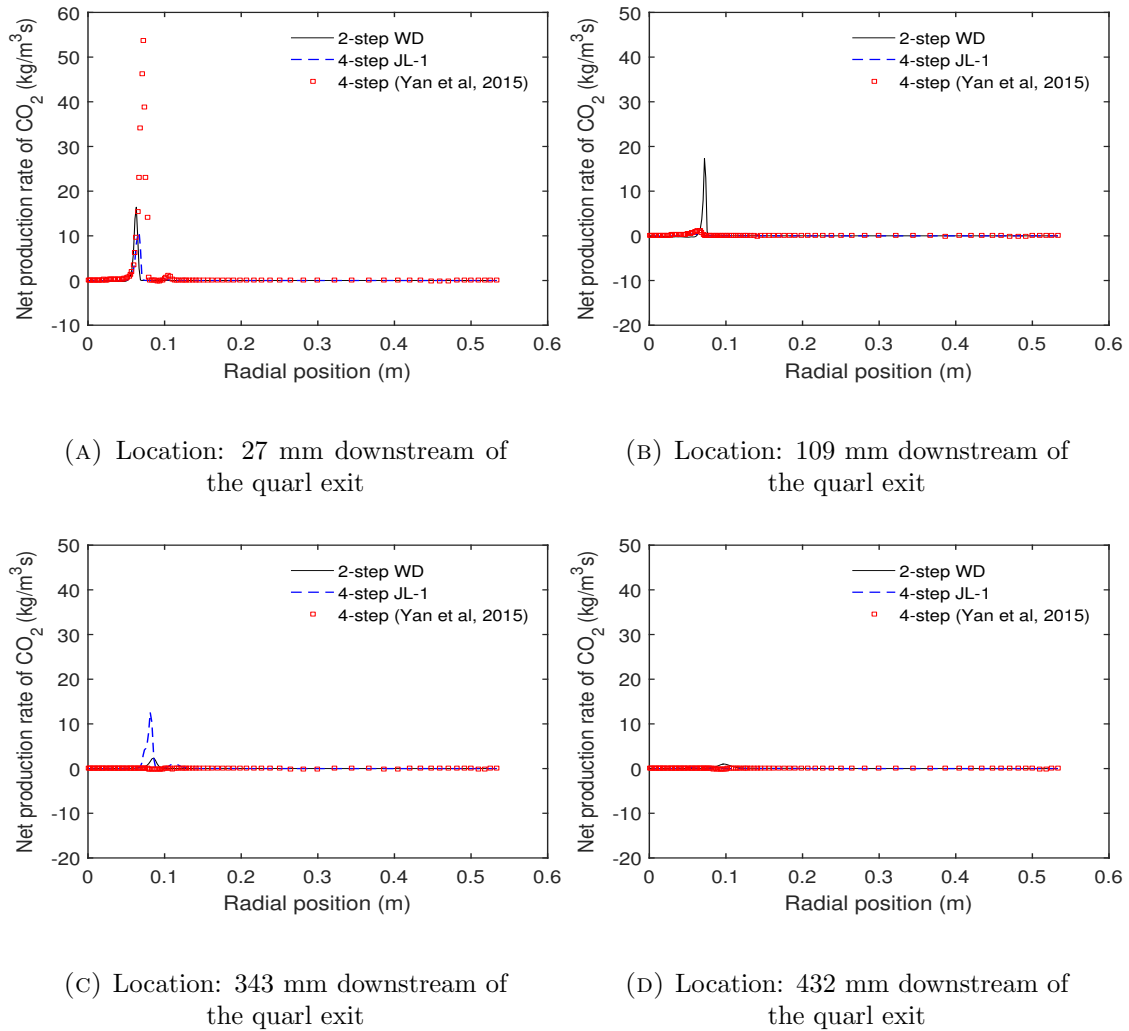


FIGURE 3.14: Radial distribution profiles of O_2 mass fraction to study the effect of reaction mechanisms

In Figure 3.15, the net production rate of CO_2 is plotted. As CO_2 is a reaction product the net production rate is equal to net reaction rate in Fluent [10]. At 27 mm, a peak can be seen at the radial position near the injection zone in the curve of the reaction mechanism used by Yan et al. (2015). This may be due to the fact that the reaction rate coefficient $k(T) = A \cdot T^b \cdot e^{-\frac{E}{RT}}$ in the oxidation of CO to CO_2 is higher with that reaction mechanism at 27 mm downstream of the quarl exit. Similar reason can be given for the other locations. At 109 mm, a smaller peak is found with the WD 2-step reaction mechanism and at 343 mm a peak is found with the JL-1 4-step reaction mechanism. At partition 432 mm, no formation of CO_2 is observed.

FIGURE 3.15: Radial distribution profiles of the net production rate of CO_2

3.8 Conclusion

The different models used in the CFD simulations have been studied and the results obtained in the air-fuel conditions are presented. The mesh with 9784 cells is enough to produce grid-independent results. The applicability of the E-EWBM developed in this thesis is demonstrated and the results are in good agreement with the experimental data. The impacts of the four different radiative property models have been discussed. Near to the centerline, absorption coefficient calculated with the E-EWBM (this thesis) is found to be higher than with the WSGGM. Results obtained with temperature, axial velocity and O_2 mass fraction at all partitions are similar for the different radiative property models. This is because the beam length of the furnace is small. The effect of reaction mechanisms is quite remarkable. The temperature predicted by the 4-step

reaction mechanism near the centreline zone is lower than that predicted by other reaction mechanisms such as 2-step and 1-step. At some partitions, relative differences can be seen in the axial velocity and O₂ mass fraction. The new E-EWBM is supposed to be generic. Its applicability in oxy-fuel combustion will be discussed in chapter 4.

Chapter 4

Implementation and impact of the E-EWBM in oxy-fuel combustion CFD

This chapter describes the implementation and impacts of the E-EWBM in oxy-fuel combustion CFD. The chapter comprises of six major sections. The first section describes the furnace which is used in the simulations. In the second section, the 3D mesh constructed for the CFD simulations is described. The third, fourth and fifth sections are about the brief description of cases in which the key models used are summarized. Lastly, the results of the two computational cases in which the only difference lies in the gas radiative property model (i.e., the E-EWBM vs the default WSGGM) are discussed. The computational time for each case is quite high and consequently the calculation has been limited to a determined number of iterations.

4.1 Furnace

The geometry of the furnace, the operational conditions (i.e., the boundary conditions used in the CFD), and the in-flame measurements are all presented in this section.

4.1.1 Geometry

The IFRF conducted the OXYFLAME project, along with industry partners, to produce information about oxy-natural gas combustion as outlined by Bollettini et al. (1997), with the following objectives [3]:

- To optimize heat transfer and NO_x emission in oxy-natural gas combustion.
- To characterize gas flames of 1-2 MW thermal input in oxy-natural gas combustion through in-flame measurements.

In the OXYFLAME configuration a refractory lining was used. The furnace consisted of 13 water cooled segments 300 mm wide. The OXYFLAME furnace is operated at 0.8 MW. The furnace is operated at a pressure of 3 mm H_2O to prevent air leaking in. In this report, the OXYFLAME configuration is taken as a test case. The dimensions of the furnace are given in Table 4.1. A cross section diagram of OXYFLAME furnace is given in Figure 4.1 [3].

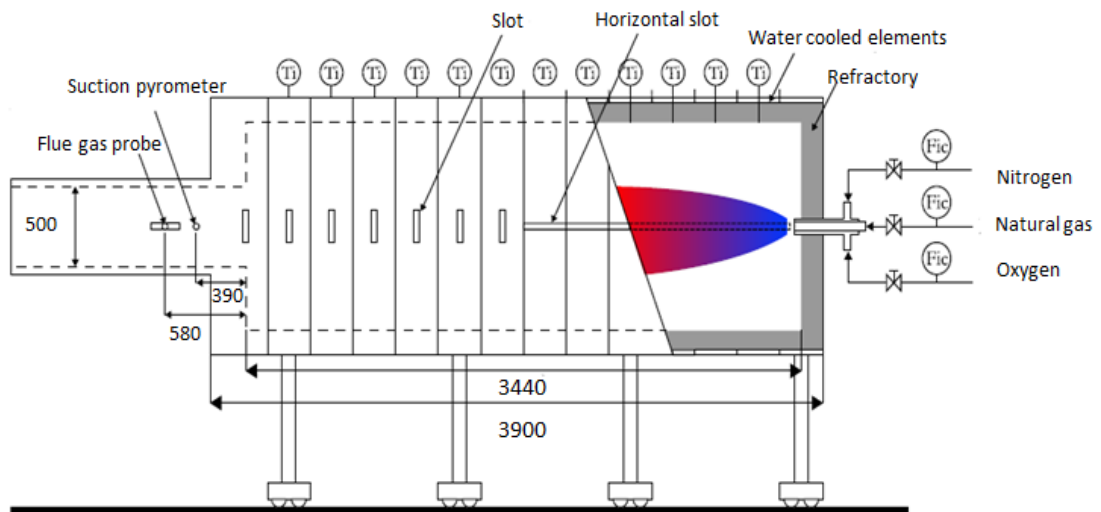


FIGURE 4.1: Cross section diagram of the OXYFLAME furnace reproduced from Bollettini et al. (1997) [3]

A horizontal slot spans the first 1700 mm from the burner in order to access for measurement. For the remainder of the furnace access is provided by slots in middle of each water cooled segments. The slots are shown in Figure 4.1. The burner is designed based on the same generic design given in Figure 4.2 [3].

Dimension[mm]	
Internal length	3440
Near square section	1050 x 1050
Chimney contraction diameter	500
Chimney length	800
Burner length	258

TABLE 4.1: Dimensions of the 0.8 MW furnace [3]

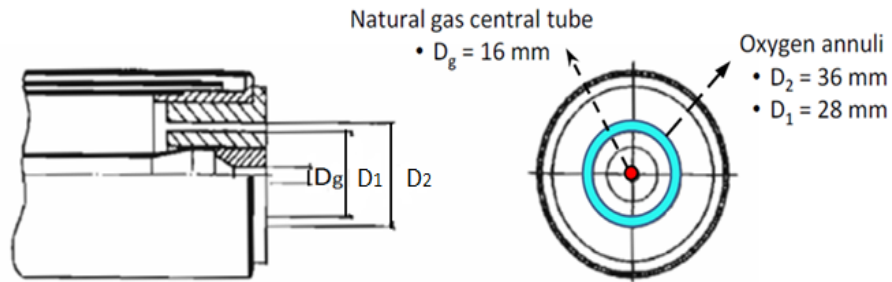


FIGURE 4.2: Diagram of the high-momentum jet burner, Burner A [3]

The natural gas is fed through the central inlet with diameter D_g , while the oxygen is fed through annular coaxial inlet with inner diameter D_1 and outer diameter D_2 .

Burner	Momentum	D_2 [mm]	D_1 [mm]	D_g [mm]
Burner A	High	36	28	16

TABLE 4.2: Dimension of high-momentum jet burner, Burner A [3]

4.1.2 Oxygen and fuel composition

The oxygen composition used in all simulations is given in Table 4.3, whereas the fuel composition is given in Table 4.4.

Species	Mass fraction	Molecular weight [kg/kmol]
O ₂	1	31.9988
N ₂	0	28.0134

TABLE 4.3: Oxygen composition used in oxy-fuel case [1]

Species	Mass fraction	Molecular weight [kg/kmol]	Standard state enthalpy [$\frac{J}{kg \cdot mol}$]
$C_{1.122}H_{4.244}$	0.894	17.75434	7.663413e+07
CO_2	0.0404	31.9988	3.93532e+08
N_2	0.062	28.0134	0
O_2	0.0036	31.9988	0

TABLE 4.4: Fuel composition used in oxy-fuel case [1]

From Table 4.3, it can be seen that the simulations have been done with the approximation of pure oxygen. This composition is obviously one of the main differences between oxy-fuel and air-fuel settings. From Table 4.4, it can be seen that a numerical fuel $C_{1.122}H_{4.244}$ is used to represent the hydrocarbons in the natural gas. The molecular weight and standard state enthalpy for the mixture of gases have been taken from the reference [1].

4.1.3 Boundary conditions

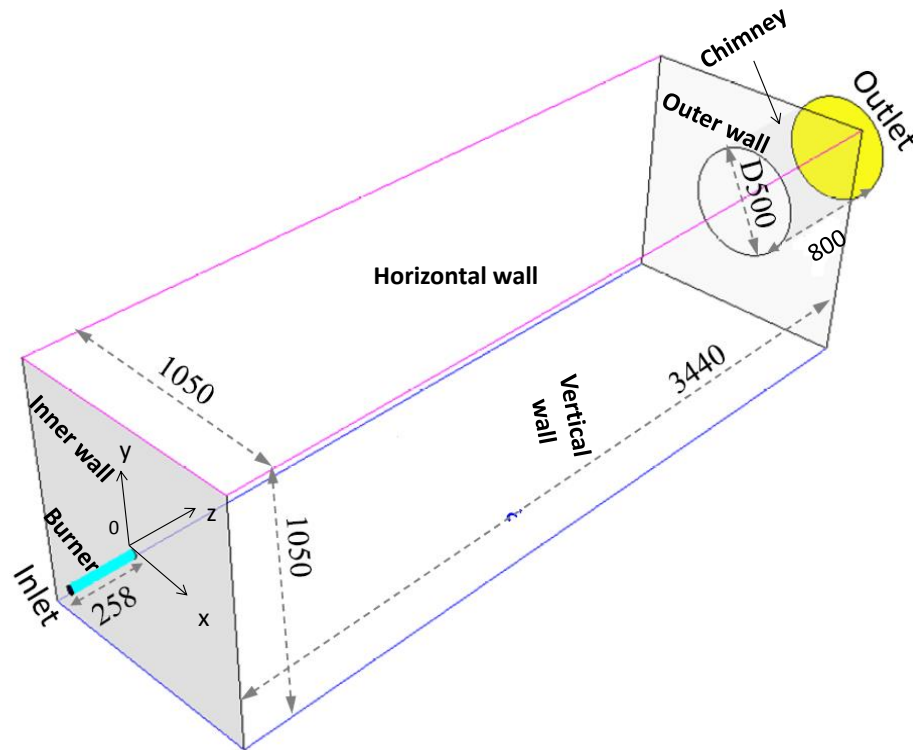


FIGURE 4.3: The full oxy-NG furnace used in simulation

The boundaries of the furnace are presented in Figure 4.3.

Inlet	Oxy-inlet	Fuel-inlet
Boundary type	Mass-flow inlet	Mass-flow inlet
Mass flow rate [<i>kg/s</i>]	0.0623611	0.0175
Flow direction	Normal to boundary	Normal to boundary
Turbulent intensity	20 %	20 %
Hydraulic diameter [m]	0.008	0.016
Total temperature [K]	298.15	298.15
Composition	Table 4.3	Table 4.4

TABLE 4.5: Boundary conditions for inlet fuel and oxygen for oxy-fuel case [3]

Outlet	Pressure-outlet
Boundary type	Pressure-outlet
Back flow Turbulent intensity	10 %
Hydraulic Diameter [m]	0.5
Inlet Temperature [K]	300

TABLE 4.6: Boundary conditions for outlet for oxy-fuel case [3]

The boundary conditions given in Tables 4.5, 4.6 and 4.7 have been used in all simulations. The boundary conditions are taken from the reference [3] in order to compare with the experimental data given in this reference. Table 4.5 shows the boundary conditions at the inlet of oxygen and natural gas. Table 4.6 shows the boundary conditions at the pressure outlet, whereas Table 4.7 shows the boundary conditions for the furnace walls.

The wall temperature is determined from a polynomial fit of measured wall temperatures by Bollettini et al. (1997) [3] and is given in Equation 4.1. A user defined function (UDF) is specified for the wall temperature in the CFD simulations. The limit of the wall temperature function is $0 \text{ m} \leq z \leq 3.44 \text{ m}$.

$$T_{wall} = 1700.598 + 212.5872 \cdot z - 46.66929 \cdot z^2 \quad (4.1)$$

Wall	Temperature [K]	Internal Emissivity
Horizontal walls	Equation 4.1	0.9
Vertical walls	Equation 4.1	0.9
Inner wall	Equation 4.1	0.9
Outer wall	300	0.9
Chimney	300	0.9
Burner	300	0.9

TABLE 4.7: Boundary conditions for walls for oxy-fuel case [3]

4.1.4 In-flame measurement

The in-flame measurements are the key part of the measuring campaign. The measurements were made via the slots as indicated in Figure 4.1. The radial profiles of velocity, velocity fluctuation, temperature and species (i.e., volume fractions of CO₂, O₂) were measured at 0.82 m and 1.42 m, downstream of the burner exit. Species measurements were also performed at 2.21 m downstream of the burner exit. The measurements were in general made at radial distance up to 0.45 m at intervals increasing from 0.01 m at the centreline to 0.05 m at the radial distance 0.45 m. The in-flame measurement instrumentation and the accuracy are introduced briefly as follows [1].

- In-flame velocity/velocity fluctuations measurements were performed using laser Doppler velocimetry (LDV): the required seeding for LDV measurements was performed with zirconium oxide particles with a size range of 2-8 μm . Zirconium oxide has a melting point of 2980° C and therefore suited for high temperature flows. The velocity measurements were reported to have good quality [1].
- In-flame temperature measurements were performed using a water-cooled suction pyrometer. The water-cooled suction pyrometer caused the temperature of the gas sampled to drop before the temperature measurements. The calibration curve developed extends to approximately 1650 K for the suction pyrometer measurement corresponding to a coherent anti-Stokes Raman spectroscopy (CARS) temperature of approximately 2200 K. The measurements presented by Lallemand et al. (1997) are not corrected. Bollettini et al. (1997) extrapolated the calibration curve for use at higher temperatures and this likely introduces errors in the temperature. The corrected temperatures are also used in this project report [1].
- In-flame species measurements were performed with a gas sampling probe. The water vapor was condensed and analysis of the gas sample was performed with different sensor/detector, depending upon the gas species to be determined [1].

(1) The high CO and H₂ concentration levels measured in oxy-flame strongly suggest that the flame temperatures must be in excess of 2400-2500° C in these flames.

(2) The measured H₂ concentrations may be a few percent off from their actual values due the recombination reactions taking place in the quenching section of the probe (i.e.,

H-atoms \rightarrow H₂ ; OH-radicals recombined to H₂O). If so, the measured H₂ concentrations should overestimate the actual flame concentrations.

(3) The NO_x measurements together with the N₂ concentration in the range of 4-10 % suggest that a small air in-leakage inside the furnace (except through the gas sampling line).

(4) The sum of all species measured lies between 98% and 102% confirming the good quality of the concentration measurements.

4.2 Mesh for the OXYFLAME furnace

Based on the data from section 4.1, a computational mesh of the interior furnace volume has been constructed for use in CFD simulations. The dimensions used for the mesh are given in Figure 4.3. Due to time restrictions and capacity of computers provided, only a mesh with 1033844 cells is constructed. The mesh centerline is aligned with the z axis. The mesh has been constructed using Ansys ICEM CFD.

The mesh is constructed with the blocking approach and consist of hexahedral cells. Hexahedral cells can be aligned with flow and this minimizes numerical diffusion [11]. The main idea to construct the mesh is taken from the reference [11]. In the block structure approach the geometry is subdivided into blocks. Then the blocks are subdivided further with hexahedral cells. Blocks serves as first level geometry discretization. A central block is used for the chimney and extend to the inner wall. The chimney diameter is the largest circle in the mesh. The three blocks are used for the surrounding region of the furnace. The central block is further divided into four o-grid blocks for the burner. The mesh burner inlet and the inner wall are shown in Figure 4.4. The flame is located in the central line and thus flow properties will vary a lot in this region. Therefore, more cells are concentrated in the central region in order to resolve the gradient more accurately.

4.2.1 Mesh quality

The quality of the mesh constructed has been evaluated by minimum angle, aspect ratio and orthogonal quality.

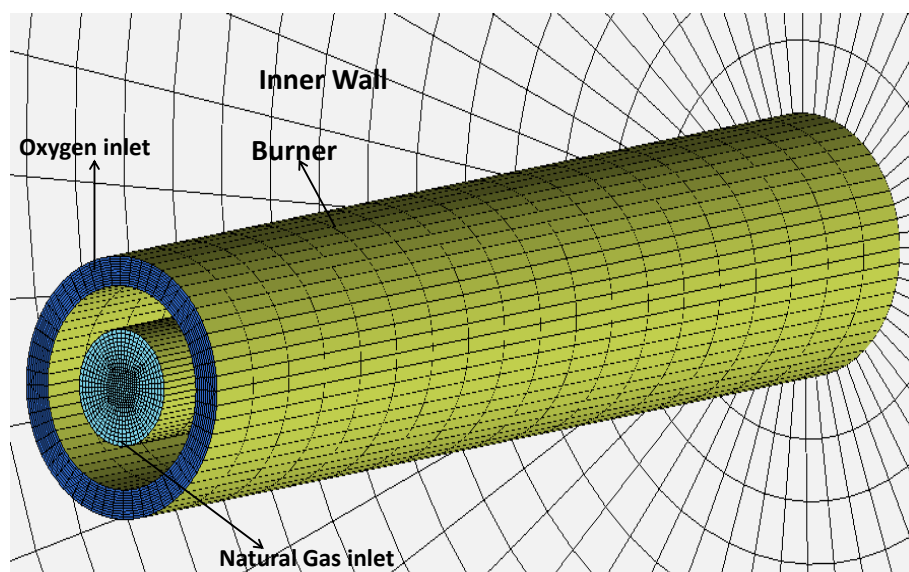
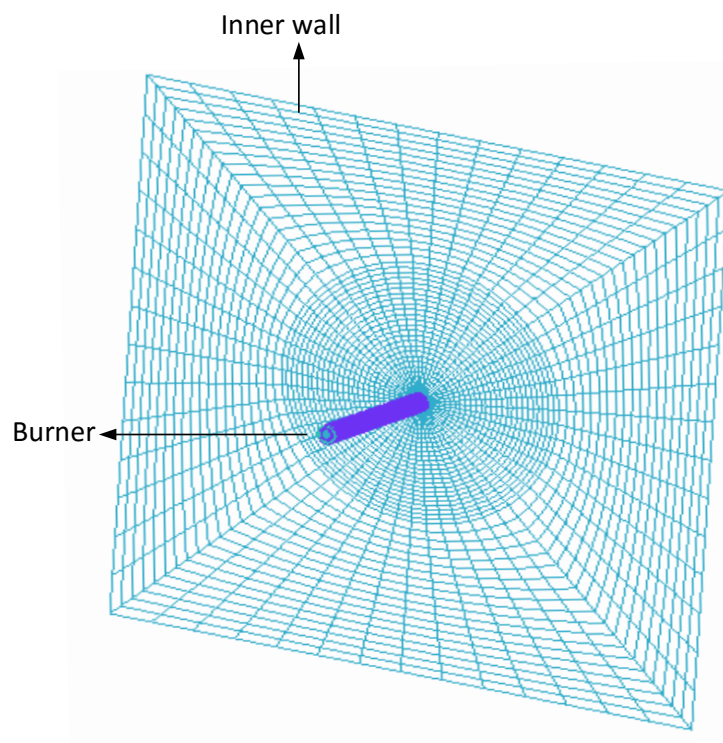


FIGURE 4.4: A close view of burner of 0.8 MW furnace

The minimum angle is determined from the minimum internal angle. Casey et al. recommends that cell angles should not be less than 40° [11]. The minimum angle reported for this mesh is 44.44° . The maximum aspect ratio is a measure of the stretching of a cell, and is defined by the size of the maximum element edge divided by the size of

Quality criterion	Value
Minimum angle	44.44°
Maximum aspect ratio	44.7612
Minimum orthogonal quality	0.7058

TABLE 4.8: Quality parameters of the mesh for oxy-fuel furnace

the minimum element edge [12]. In order to achieve good convergence the aspect ratio should be always less than 50 [11], whereas the maximum aspect ratio reported for this mesh is 44.7612. The orthogonal quality for cells is computed using the face normal vector, the vector from the cell centroid to the centroid of each of the adjacent cells, and the vector from the cell centroid to the centroid of each of the faces [12]. The value close to 0 corresponds to the worst quality, whereas quality near to one is good enough. For this mesh the reported orthogonal quality is of 0.705858.

4.3 Computational cases: an overview

For oxy-fuel case all the models are precisely same as for the air-fuel case, except the global combustion mechanisms. All the models have been discussed in chapter 3. Here only models selected for the simulations have been stated.

- The realizable k - ϵ turbulence model is selected for the oxy-fuel simulations.
- The near wall modelling is done through Enhanced wall treatment for the oxy-fuel simulations.
- In order to solve radiative heat transfer equations the DO model has been selected for the simulations.
- For calculation of the absorption coefficient both E-EWBM (this thesis) and default WSGGM have been used for comparison.
- For modelling species, the Species Transport method has been selected, in which the refined WD 2-step global mechanism applicable to oxy-fuel CFD is used to account for the impact of the elevated CO_2 concentration in oxy-fuel conditions.
- Eddy-Dissipation-Concept is selected for turbulence-chemistry interaction for the simulations.

4.4 Reaction mechanism

oxy WD: the original WD 2-step mechanism refined for oxy-fuel conditions. Reference calculations were done with a detailed chemical kinetic mechanism, validated for oxy-fuel combustion conditions. In the refined mechanism, the initiating reactions involving hydrocarbon CH_4 and O_2 were retained, while the CO - CO_2 reactions were refined in order to improve prediction of major species concentrations. The main concern has been to capture the trend and the level of CO predicted by the detailed mechanism along with the correct equilibrium concentration. The refined mechanism is given in Table 4.9 [1]. The oxy-WD reaction mechanism has been used in the simulations with both computational cases.

	Reactions	Rate equations[$\text{kmol}/(\text{m}^3\text{s})$]	A	b	E
1	$\text{CH}_4 + 1.5\text{O}_2 \rightarrow \text{CO} + 2\text{H}_2\text{O}$	$[\text{CH}_4]^{0.7}[\text{O}_2]^{0.8}$	5.03e11	0	2.00e08
2	$\text{CO} + 0.5\text{O}_2 \rightarrow \text{CO}_2$	$[\text{CO}][\text{O}_2]^{0.25}[\text{H}_2\text{O}]^{0.5}$	2.24e06	0	4.18e07
3	$\text{CO}_2 \rightarrow \text{CO} + 0.5\text{O}_2$	$[\text{CO}_2][\text{O}_2]^{-0.25}[\text{H}_2\text{O}]^{0.5}$	1.10e13	-0.97	3.28e08

TABLE 4.9: Refined WD 2-step reaction mechanism for CH_4 under oxy-fuel combustion [1]

4.5 Properties and solution methods/control

In this section the material properties, relaxation factors and solution schemes used in the oxy-fuel simulations have been discussed.

4.5.1 Material properties

The material properties used in the oxy-fuel simulations are given in Table 4.10.

Property	Value
Thermal conductivity k [$\frac{\text{W}}{\text{m}\cdot\text{K}}$]	0.0454
Viscosity μ [$\frac{\text{kg}}{\text{m}\cdot\text{s}}$]	1.72e-05
Mass diffusion coefficient $D_{i,m}$ [$\frac{\text{m}^2}{\text{s}}$]	2.88e-05
Scattering coefficients σ_s [m^{-1}]	0
Refractive index n	1

TABLE 4.10: Material properties used in all oxy-fuel CFD simulations

In the oxy-fuel simulations the specific heat capacity c_p for the gas mixture is determined from Equation 3.10 in the previous chapter as a mixing-law, i.e., the sum of the mass fraction weighted c_p of each species.

4.5.2 Solution method

The RANS equations and models have been solved using the ANSYS Fluent V15 software. Fluent employs the finite volume method to solve the RANS differential equations. For the pressure-velocity coupling in the oxy-fuel simulations SIMPLE scheme has been used. In this segregated algorithm, the individual governing equations for the solution variables are solved one after another. The advantages of this method over the coupled algorithm are more accurate solution and less memory required [10].

In all cases, Green-Gauss Cell Based spatial discretization has been used for the determination of gradients and derivatives, because less time is required to compute than with other settings. This method is computational efficient because the value is taken from the arithmetic average of values at the neighboring cell centers [10]. As a large number of cells have been used, the time consumed by the oxy-fuel simulations becomes important.

The first order upwind scheme has been used for all simulations because it leads to better convergence than the second order upwind scheme [10].

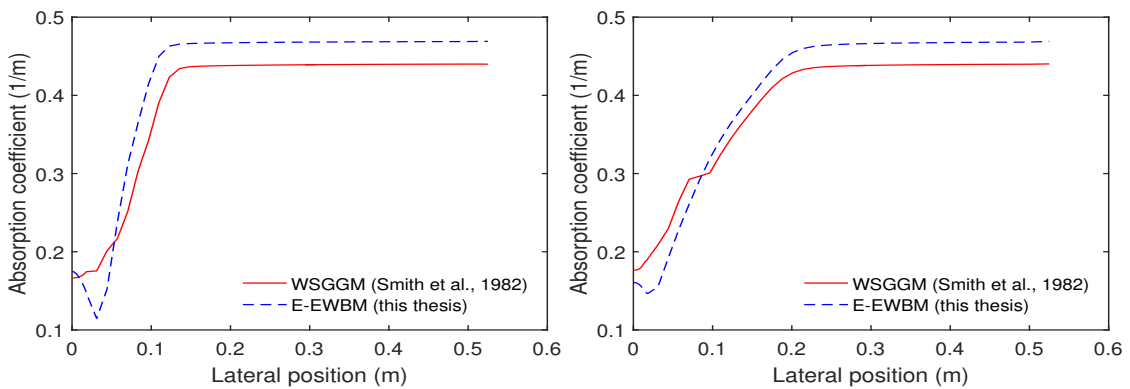
Table 4.11 shows the under relaxation factors used in the oxy-natural gas simulations. Default values of under-relaxation factors have been used in all simulations.

Equation	Relaxation factors
Pressure	0.3
Momentum	0.7
Density	1
Body forces	1
Turbulent Kinetic Energy	0.8
Turbulent Dissipation rate	0.8
Turbulent Viscosity	1
Energy	1
Discrete Ordinates	1

TABLE 4.11: Relaxation factors employed in simulation for oxy-fuel simulations

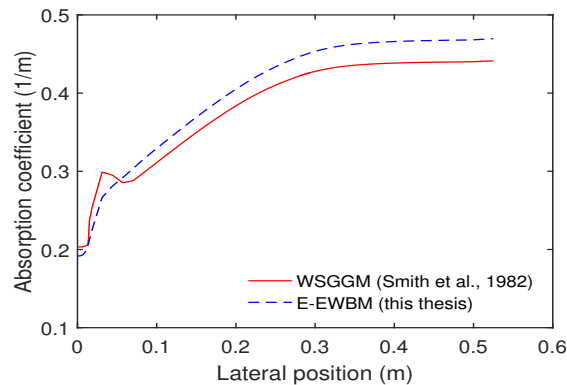
4.6 Effect of radiation property models: results and discussion

This part mainly focuses on the implementation of the new E-EWBM in oxy-fuel combustion CFD and its impacts. Two cases have been compared. The only difference between them is the radiation property model used to calculate the absorption coefficient. Due to time restrictions, the simulations have been limited to 3478 iterations and the solution is not fully converged. However, the solution had a converging trend before restricting the simulation.



(A) Location: 82 cm downstream of the burner exit

(B) Location: 142 cm downstream of the burner exit



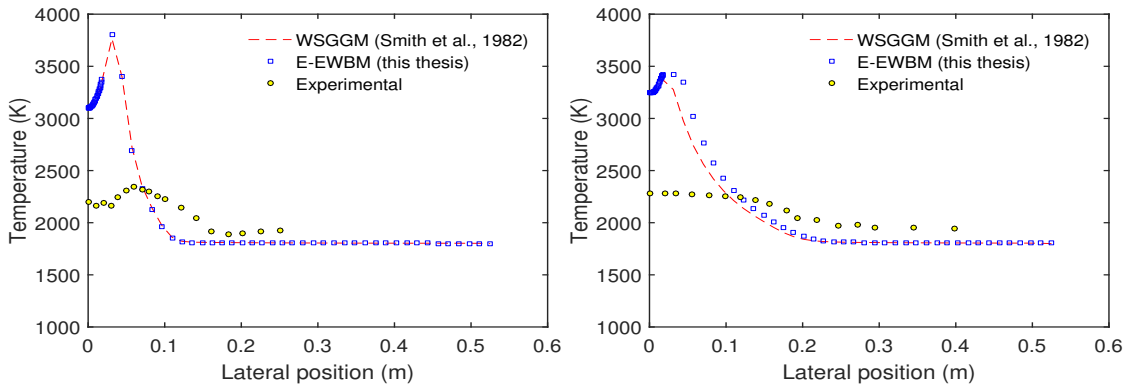
(C) Location: 221 cm downstream of the burner exit

FIGURE 4.5: Radial distribution profiles of absorption coefficient in oxy-fuel combustion

The temperature, axial velocity and volume fractions (dry) of O_2 and CO_2 have been obtained from the CFD simulations and compared with the experimental data from the reference [2]. Additionally, the absorption coefficient have been plotted. In all graphs,

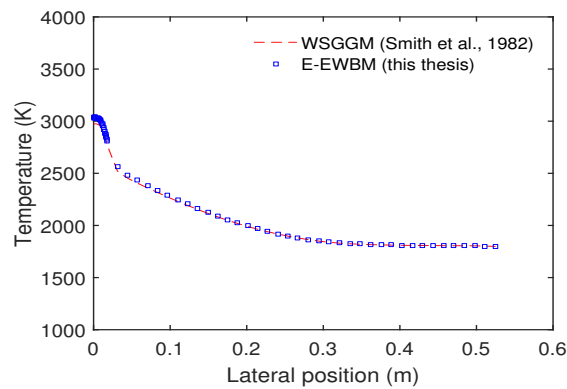
the lateral position of 0 m corresponds to the centerline, whereas the position of 0.525 m corresponds to the wall.

Figure 4.5 shows the absorption coefficient as a function of lateral distance (y axis) from the centerline at 82, 142 and 221 cm downstream of the burner exit. Some relative differences in the absorption coefficient can be observed because the E-EWBM accounts for the contribution of CH_4 and CO . Further, some discontinuities can be observed while using the WSGGM near the centerline. In the WSGGM small changes in gas composition may induce a sudden change in the calculated emissivity and then the absorption coefficient. The use of the E-EWBM eliminates such discontinuity, since this model can address the species variations naturally and smoothly.



(A) Location: 82 cm downstream of the burner exit

(B) Location: 142 cm downstream of the burner exit



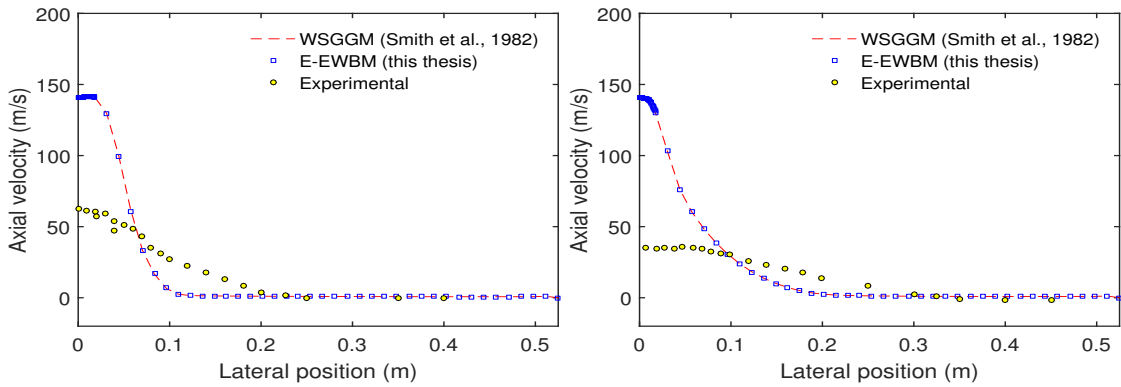
(C) Location: 221 cm downstream of the burner exit

FIGURE 4.6: Radial distribution profiles of temperature in oxy-fuel combustion

Figure 4.6 shows the temperature as a function of lateral distance from the centerline at 82, 142 and 221 cm downstream of the burner exit. The temperature predicted by

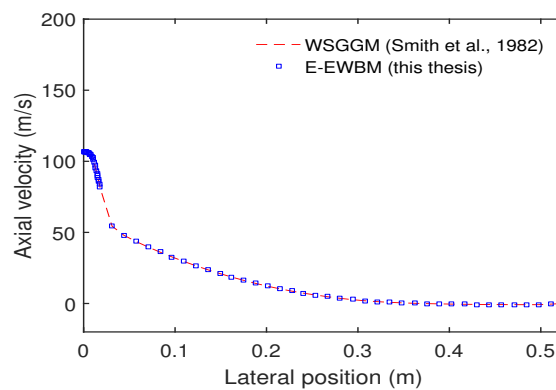
both E-EWBM and WSGGM is similar for this small-scale furnace with a beam length around 0.792 m.

Here it has to be mentioned that at axial positions 82 and 142 cm of the burner there is a temperature peak near the centerline, which leads to a quite high temperature. This is may be due to the fact that the solution is not fully converged. At this stage, the energy imbalance reported is quite high ($>5\%$). Further, one of the potential reasons can be that the mesh near the centerline is not of good quality. The cell growth ratio is found to be high. All these potential problems could have lead to variation in the temperature peak near the centerline. However, it can be seen from Figure 4.6 that at lateral positions beyond the near-centerline zone the temperature is in the order of magnitude expected.



(A) Location: 82 cm downstream of the burner exit

(B) Location: 142 cm downstream of the burner exit



(C) Location: 221 cm downstream of the burner exit

FIGURE 4.7: Radial distribution profiles of axial velocity in oxy-fuel combustion

Figure 4.7 shows the axial velocity as a function of lateral distance from the centerline at 82, 142 and 221 cm downstream of the burner exit. Simulations with the E-EWBM and WSGGM have the same axial velocity reading. This is due to the fact that the beam length of the furnace is quite small. Moreover, it can be observed that the axial velocity is high near the centerline, because of similar potential problems discussed above. However, axial velocity is in good agreement with the experimental data at lateral positions beyond the centerline zone.

Figure 4.8 shows the O_2 volume fraction as a function of lateral distance from the centerline at 82 and 142 cm downstream of the burner exit. There is a peak at the axial position 82 cm with same pattern as the experimental data.

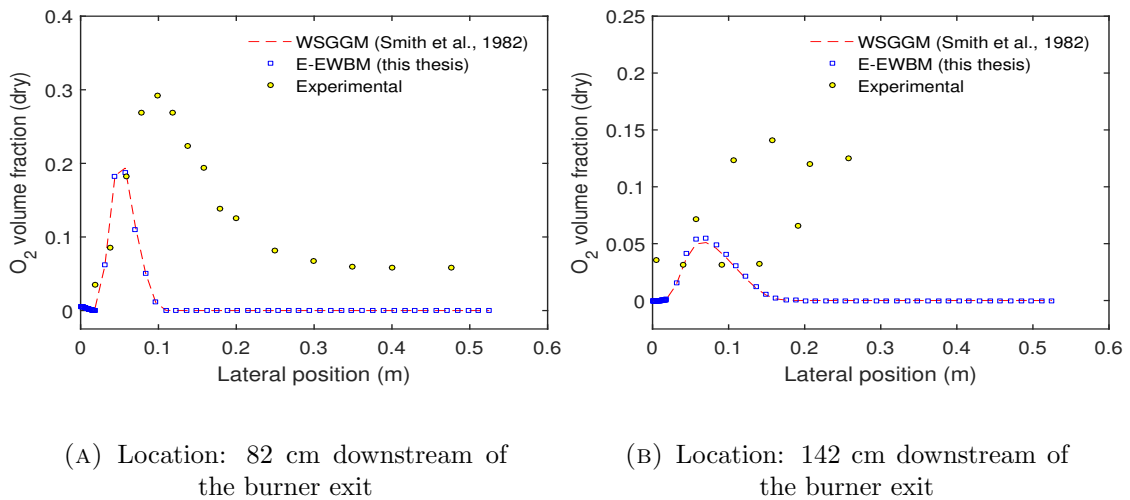
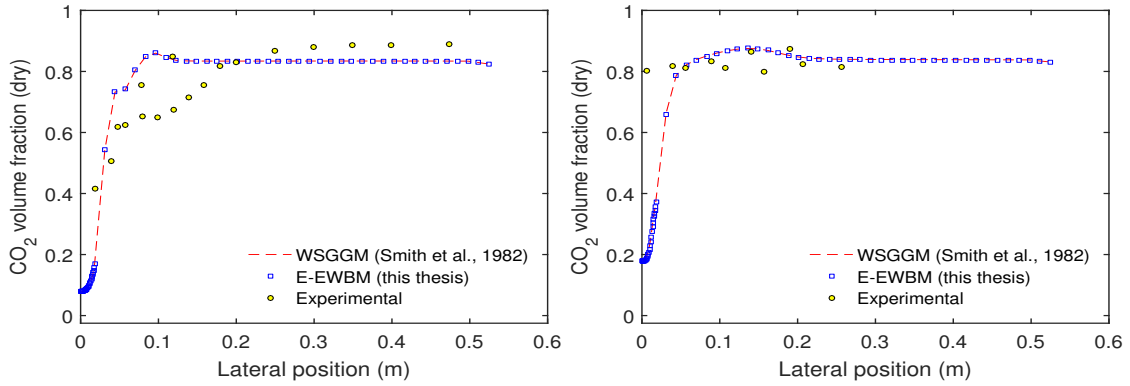


FIGURE 4.8: Radial distribution profiles of O_2 volume fraction in oxy-fuel combustion

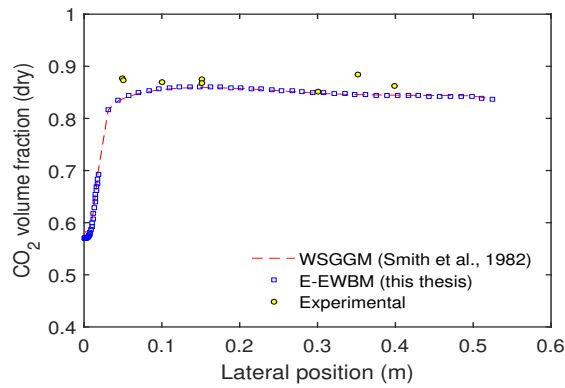
Figure 4.9 shows the CO_2 volume fraction as a function of lateral distance from the centerline at 82, 142 and 221 cm downstream of the burner exit. A reasonable agreement of both models with the experimental data is achieved.

As a conclusion, the applicability of the E-EWBM in oxy-fuel combustion is demonstrated. It is expected to make remarkable differences in industrial furnaces with large beam lengths.



(A) Location: 82 cm downstream of the burner exit

(B) Location: 142 cm downstream of the burner exit



(C) Location: 221 cm downstream of the burner exit

FIGURE 4.9: Radial distribution profiles of CO_2 volume fraction in oxy-fuel combustion

4.7 Conclusion

Simulations in oxy-fuel conditions have been performed. First, a mesh with 1033844 cells has been constructed in ICEM CFD. The computational time required is quite high, as given in Table 4.12, and thus the simulations have been restricted to a certain number of iterations. The E-EWBM (this thesis) and the default WSGGM have been simulated. The data for absorption coefficient, temperature, axial velocity, O_2 and CO_2 has been presented. Some differences have been found in the absorption coefficient.

Radiation model	Time (hours)	Iterations
WSGGM	1	64
E-EWBM	1	6

TABLE 4.12: Computational time of the WSGGM and E-EWBM in the oxy-fuel case

Chapter 5

Conclusion and future work

5.1 Conclusion

- The EWBM has been simplified to develop a more computationally efficient model (E-EWBM). The validation has been done by comparing the emissivity value with the one in literature for a particular gas mixture. The emissivity obtained with the E-EWBM is 0.167252356, while the emissivity reported in the literature is 0.167253. Thus, it can be concluded that the E-EWBM developed is reliable and well validated. Further, the plots of the gas emissivity as a function of temperature and beam length have been presented. The new E-EWBM shows a significant difference while comparing with the most widely used WSGGM, especially when the temperature decreases and the beam length increases. It signifies that the E-EWBM leads to more accurate result in the CFD simulations.

- CFD simulations have been performed in air-fuel combustion. The furnace is represented as a 2D axi-symmetric swirl problem of an inherently 3D problem. Experimental data is available in literature for this furnace. The realizable $k - \epsilon$ model has been chosen for turbulence. The discrete ordinates method has been used to solve the radiative transfer equation. The species transport method has been used to model reactions.

The effect of mesh has been evaluated to identify which of the meshes proposed lead to a mesh independent solution. According to this, the mesh with 9784 cells has been selected for the simulations.

Then, the effect of gas radiative property has been studied. Four models have been used and the CFD results are compared against the experimental data: the E-EWBM developed in this thesis, the default WSGGM (Smith et al., 1982), the refined WSGGM (Yin, 2013) and the recently developed E-EWBM (Yan et al., 2015). Near the centre line, the absorption coefficient calculated by the E-EWBM developed in this thesis is found to be higher than the WSGGM. The E-EWBM makes little impact in the prediction of temperature, axial velocity and O₂ mass fraction. This is because the beam length of the furnace is small. The effect of reaction mechanisms is quite remarkable. The temperature predicted by the 4-step reaction mechanism near the centre line zone is lower than that predicted by other reaction mechanisms such as 2-step and 1-step. At some partitions, relative differences can be seen in the axial velocity and O₂ mass fraction.

- CFD simulations have been performed in oxy-fuel combustion. A 3D mesh with 1033844 cells has been constructed in ICEM CFD. The computational time required is quite high and thus the simulations have been restricted to a certain number of iterations. The E-EWBM developed in this thesis and the default WSGGM have been simulated. The data for absorption coefficient, temperature, axial velocity, O₂ and CO₂ has been presented. Some differences have been found in the absorption coefficient.

5.2 Future work

- The computational efficiency of the developed E-EWBM model is acceptable but its computational efficiency is still slower than WSGGM by a factor of 11. So further efforts should be made in order to decrease the computational time of the E-EWBM.
- A 2D-mesh is used for the air-fuel simulations, as a result, some difference can be seen in the experimental data and simulation results. The next step will be to simulate the full 3D-problem along with the study of different radiation models and combustion models that are available.
- The oxy-fuel case is not a success in terms of the agreement between CFD results and the experimental data. The computational time could be reduced by using the furnace symmetry. In future a mesh with symmetrical planes will be created and the mesh quality can be largely improved. In this way, it could be possible to achieve faster

convergence and better accuracy. Finally, a mesh independent study and a comparison of the different radiative property models will be performed.

Appendix A

Appendix: WSGGM coefficients for emissivity

i	k_i	$b_{\epsilon,i,1} \cdot 10^1$	$b_{\epsilon,i,2} \cdot 10^4$	$b_{\epsilon,i,3} \cdot 10^7$	$b_{\epsilon,i,4} \cdot 10^{11}$
CO ₂ , $P_c \rightarrow 0[atm]$					
1	0.3966	0.4334	2.620	-1.560	2.565
2	15.64	-0.4814	2.822	-1.794	3.274
3	394.3	0.5492	0.1087	-0.3500	0.9123
H ₂ O, $P_w \rightarrow 0[atm]$					
1	0.4098	5.977	-5.119	3.042	-5.564
2	6.325	0.5677	3.333	-1.967	2.718
3	120.5	1.807	-2.334	1.008	-1.454
H ₂ O, $P_w \rightarrow 1[atm]$					
1	0.4496	6.324	-8.358	6.135	-13.03
2	7.113	-0.2016	7.145	-5.212	9.868
3	119.7	3.500	-5.040	2.454	-3.888
$\frac{P_w}{P_c} = 1, (where P_c = 0.1atm)$					
1	0.4303	5.150	-2.303	0.9779	-1.494
2	7.055	0.7749	3.399	-2.297	3.770
3	178.1	1.907	-1.824	0.5608	-0.5122
$\frac{P_w}{P_c} = 2, (where P_c = 0.1atm)$					
1	0.4201	6.508	-5.551	3.029	-5.553
2	6.516	-0.2504	6.112	-3.882	6.528
3	131.9	2.718	-3.118	1.221	-1.612

TABLE A.1: WSGGM coefficients for emissivity for Smith et al. (1982) WSGGM [1]

i	k_i	$b_{\epsilon,i,1}$	$b_{\epsilon,i,2}$	$b_{\epsilon,i,3}$	$b_{\epsilon,i,4}$
$\text{CO}_2, P_c \rightarrow 0[atm]$					
1	0.163233	0.204623	-0.378060	0.666639	-0.203453
2	13.096584	-0.020227	0.256006	-0.195201	0.040493
3	175.474735	0.044221	0.003850	-0.020175	0.004919
4	1310.847307	0.039311	-0.054832	0.025370	-0.003891
$\frac{P_w}{P_c}=0.05(P_c = 0.1 [atm])$					
1	0.352505	0.315106	0.023475	-0.057930	0.008408
2	8.210621	0.092474	0.109146	-0.121000	0.027145
3	137.410012	0.031702	0.037396	-0.040731	0.008742
4	1269.710976	0.046138	-0.061392	0.027164	-0.003996
$\frac{P_w}{P_c}=1(P_c = 0.1 [atm])$					
1	0.261021	0.500119	-0.447068	0.286878	-0.059165
2	3.147817	0.071592	0.508252	-0.384253	0.073477
3	54.265868	0.155320	-0.104294	0.014096	0.001643
4	482.900353	0.072615	-0.100601	0.046681	-0.007224
$\frac{P_w}{P_c} = 2, (P_c = 0.1atm)$					
1	0.179160	0.542458	-0.658411	0.466444	-0.100186
2	2.388971	0.101734	0.518429	-0.386151	0.073453
3	28.415805	0.146066	-0.008745	-0.058325	0.015984
4	253.059089	0.129511	-0.187993	0.09709	-0.014493
$P_w \rightarrow 0[atm]$					
1	0.085523	0.966357	-0.790165	-0.050144	-0.100186
2	2.388971	0.101734	0.518429	-0.386151	0.073453
3	8.549733	0.060870	0.436788	-0.395493	0.085146
4	201.906503	0.103568	-0.153135	0.074910	-0.012091
$P_w = 0.05[atm]$					
1	0.232724	0.340618	-0.105469	0.068051	-0.017828
2	2.134299	0.175818	-0.063466	0.086631	-0.026581
3	9.266065	0.044325	0.288376	-0.258205	0.054333
4	134.988332	0.126628	-0.186480	0.090755	-0.014569
$P_w = 1[atm]$					
1	0.065411	-0.077336	0.661776	-0.362515	0.053534
2	0.696552	0.506777	-0.758948	0.516146	-0.102909
3	4.862610	-0.079989	0.851078	-0.604264	0.113500
4	60.255980	0.373898	-0.540887	0.258923	-0.040957

TABLE A.2: WSGGM coefficients for emissivity for Yin (2013) refined WSGGM [4]

Appendix B

**Appendix: Look up table for
polynomial coefficients for
E-EWBM Yan et al. (2015)**

	b_0	b_1	b_2
$\alpha_{ij,\text{H}_2\text{O},140}$	1.49e+02	-5.46e-01	5.65e-04
$\alpha_{ij,\text{H}_2\text{O},1600}$	2.31e+04	-9.69e+01	1.03e-01
$\alpha_{ij,\text{H}_2\text{O},3760}$	2.49e+01	-2.60e-04	3.86e-07
$\alpha_{ij,\text{H}_2\text{O},5350}$	3.05e+00	-3.38e-04	6.01e-07
$\alpha_{ij,\text{H}_2\text{O},7250}$	2.50e+00	-3.53e-06	5.15e-09
$\alpha_{ij,\text{CO}_2,667}$	9.98e-01	2.32e-01	-4.19e-04
$\alpha_{ij,\text{CO}_2,960}$	1.33e-02	-1.02e-04	2.06e-07
$\alpha_{ij,\text{CO}_2,1060}$	1.34e-02	-1.04e-04	2.08e-07
$\alpha_{ij,\text{CO}_2,2410}$	9.06e+04	-3.87e+02	4.18e-01
$\alpha_{ij,\text{CO}_2,3660}$	4.11e+00	-7.91e-04	1.50e-06
$\alpha_{ij,\text{CO}_2,5200}$	6.95e-02	-2.55e-05	4.85e-08
$\alpha_{ij,\text{CO},2143}$	1.22e+02	-4.89e-01	5.43e-04
$\alpha_{ij,\text{CO},4260}$	1.42e-01	-1.10e-05	1.74e-08
$\alpha_{ij,\text{CH}_4,4220}$	2.97e+00	-5.56e-04	1.10e-06
$\alpha_{ij,\text{CH}_4,5861}$	4.39e-01	-1.41e-04	2.67e-07

TABLE B.1: Polynomial coefficients $\alpha_{ij}(T)$ for temperature range of 300-500 [K] [7]

	b_0	b_1	b_2
$\beta_{ij,\text{H}_2\text{O},140}$	1.37e-01	-2.34e-04	1.76e-07
$\beta_{ij,\text{H}_2\text{O},1600}$	8.75e-02	-1.55e-04	1.87e-07
$\beta_{ij,\text{H}_2\text{O},3760}$	2.24e-01	-4.00e-04	4.42e-07
$\beta_{ij,\text{H}_2\text{O},5350}$	7.62e-02	-1.37e-04	1.67e-07
$\beta_{ij,\text{H}_2\text{O},7250}$	1.10e-01	-1.96e-04	2.16e-07
$\beta_{ij,\text{CO}_2,667}$	5.59e-02	-8.18e-05	4.64e-07
$\beta_{ij,\text{CO}_2,960}$	5.02e-02	-1.42e-04	4.02e-07
$\beta_{ij,\text{CO}_2,1060}$	1.08e-01	-1.82e-04	8.53e-07
$\beta_{ij,\text{CO}_2,2410}$	2.38e-01	-4.18e-04	1.70e-06
$\beta_{ij,\text{CO}_2,3660}$	1.24e-01	-2.38e-04	1.06e-06
$\beta_{ij,\text{CO}_2,5200}$	4.53e-01	-1.30e-03	4.27e-06
$\beta_{ij,\text{CO},2143}$	7.20e-02	-1.31e-04	1.28e-07
$\beta_{ij,\text{CO},4260}$	1.61e-01	-3.00e-04	3.06e-07
$\beta_{ij,\text{CH}_4,1310}$	9.66e-02	-2.84e-04	5.89e-07
$\beta_{ij,\text{CH}_4,3020}$	7.64e-02	-2.17e-04	4.34e-07
$\beta_{ij,\text{CH}_4,4220}$	4.06e-01	-1.24e-03	2.53e-06
$\beta_{ij,\text{CH}_4,5861}$	8.30e-01	-2.72e-03	5.59e-06

TABLE B.2: Polynomial coefficients $\beta_{ij}(T)$ for temperature range of 300-500 [K] [7]

	b_0	b_1	b_2	b_3	b_4	b_5	b_6	b_7
$\alpha_{ij, \text{H}_2\text{O}, 3760}$	24.90321	-6.5e-05	4.75e-08	1.718e-10	-2.12e-13	1.141e-16	-3.1e-20	3.3613e-24
$\alpha_{ij, \text{H}_2\text{O}, 5350}$	3.104651	-0.00055	6.09e-07	7.648e-10	-9.68e-13	5.106e-16	-1.4e-19	1.4812e-23
$\alpha_{ij, \text{H}_2\text{O}, 7250}$	2.495858	-2.7e-05	3.03e-07	-8.77e-10	1.102e-12	-6.27e-16	1.74e-19	-1.929e-23
$\alpha_{ij, \text{CO}_2, 960}$	0.069745	-0.0005	1.24e-06	-1.25e-09	7.304e-13	-2.53e-16	4.83e-20	-3.91e-24
$\alpha_{ij, \text{CO}_2, 1060}$	0.070363	-0.005	1.25e-06	-1.25e-09	7.318e-13	-2.54e-16	4.87e-20	-3.97e-24
$\alpha_{ij, \text{CO}_2, 3660}$	4.162493	-0.00089	8.28e-07	2.395e-09	-2.8e-12	1.442e-15	-3.7e-19	3.968e-23
$\alpha_{ij, \text{CO}_2, 5200}$	0.072587	-4.2e-05	7.55e-08	-1.17e-11	-7.33e-15	7.894e-18	-2.7e-21	3.396e-25
$\alpha_{ij, \text{CO}, 4260}$	0.134803	5.227e-05	-1.97e-07	3.39e-10	-2.7e-13	1.206e-16	-2.9e-20	2.92e-24
$\alpha_{ij, \text{CH}_4, 4220}$	3.049165	-0.001	1.96e-06	-5.8e-10	-7.6e-14	1.25e-16	-4.1e-20	4.71e-24
$\alpha_{ij, \text{CH}_4, 5861}$	0.459851	-0.00025	4.75e-07	-1.4e-10	1.1e-14	2.23e-17	-1e-20	1.38e-24

TABLE B.3: Polynomial coefficients for $\alpha_{ij}(T)$ for temperature range 500-2000 [K] [7]

	b_0	b_1	b_2	b_3	b_4	b_5	b_6	b_7
$\beta_{0,\text{H}_2\text{O},140}$	0.143246	-0.00033	5.63e-07	-6.1e-10	4.222e-13	-1.77e-16	4.152e-20	-4.1e-24
$\beta_{ij,\text{H}_2\text{O},1600}$	0.087998	-0.00021	4.53e-07	-4.7e-10	3.452e-13	-1.49e-16	3.564e-20	-3.6e-24
$\beta_{ij,\text{H}_2\text{O},3760}$	0.224847	-0.00051	1.01e-06	-9.9e-10	6.943e-13	-2.83e-16	6.426e-20	-6.2e-24
$\beta_{ij,\text{H}_2\text{O},5350}$	0.077023	-0.00018	3.94e-07	-4e-10	2.98e-13	-1.26e-16	2.916e-20	-2.9e-24
$\beta_{ij,\text{H}_2\text{O},7250}$	0.113097	-0.00027	5.34e-07	-5.3e-10	3.879e-13	-1.62e-16	3.749e-20	-3.7e-24
$\beta_{ij,\text{CO}_2,960}$	2.60e-02	1.34e-05	1.06e-07	1.16e-10	-1.04e-13	-5.8e-17	1.46e-20	-1.5e-24
$\beta_{ij,\text{CO}_2,1060}$	7.93e-02	2.47e-05	3.54e-07	2.82e-10	3.6e-13	-2e-16	5.01e-20	-5.2e-24
$\beta_{ij,\text{CO}_2,2410}$	1.65e-01	7.43e-05	6.19e-07	6.63e-10	3.37e-13	-2.3e-16	6.4e-20	-6.9e-24
$\beta_{ij,\text{CO}_2,3660}$	8.74e-02	3.36e-05	3.8e-07	4.36e-10	4.31e-13	-2.7e-16	7.08e-20	-7.5e-24
$\beta_{ij,\text{CO}_2,5200}$	2.40e-01	1.88e-04	8.91e-07	1.95e-09	1.59e-12	-1e-15	2.78e-19	-3e-23
$\beta_{ij,\text{CO},2413}$	0.0796287	-0.000223	4.67e-07	-5.21e-10	3.58e-13	-1.5e-16	3.49e-20	-3.5e-24
$\beta_{ij,\text{CO},4260}$	0.1805136	-0.000522	1.12e-06	-1.23e-09	8.38e-13	-3.5e-16	8.06e-20	-8e-24
$\beta_{ij,\text{CH}_4,1310}$	0.081379	-0.00023	7.25e-07	-7.2e-10	8.13e-13	-1.7e-16	2.59e-20	-2e-24
$\beta_{ij,\text{CH}_4,3020}$	0.066498	-0.00019	5.68e-07	-5.7e-10	5.88e-13	-9e-17	8.44e-21	-2.8e-25
$\beta_{ij,\text{CH}_4,4220}$	0.340122	-0.001	3.01e-06	-2.8e-09	2.93e-12	-4.7e-17	-6.6e-20	9.28e-24
$\beta_{ij,\text{CH}_4,5861}$	0.683294	-0.00215	6.5e-06	-6.1e-09	6.23e-12	4.61e-16	-3.2e-19	-3.99e-23

TABLE B.4: Polynomial coefficients for $\beta_{ij}(T)$ for temperature range of 500-2000 [K] [7]

	b_0	b_1	b_2	b_3	b_4
$\alpha_{ij,\text{H}_2\text{O},140}$	-1.73e+05	2.98e+02	-1.91e-01	5.44e-05	-5.87e-09
$\alpha_{ij,\text{H}_2\text{O},1600}$	1.78e+03	-2.81e+00	1.73e-03	-4.81e-07	5.04e-11
$\alpha_{ij,\text{H}_2\text{O},3760}$	2.49e+01	3.20e-05	6.02e-08	-1.37e-11	1.25e-15
$\alpha_{ij,\text{H}_2\text{O},5350}$	2.83e+00	-9.59e-05	7.38e-07	-1.46e-10	1.19e-14
$\alpha_{ij,\text{H}_2\text{O},7250}$	2.50e+00	-7.76e-04	5.75e-07	-1.03e-10	7.71e-15
$\alpha_{ij,\text{CO}_2,667}$	-3.36e+05	5.95e+02	-3.93e-01	1.16e-04	-1.27e-08
$\alpha_{ij,\text{CO}_2,960}$	-1.13e-01	2.48e-04	-6.03e-08	1.11e-11	-8.33e-16
$\alpha_{ij,\text{CO}_2,1060}$	-1.19e-01	2.60e-04	-6.66e-08	1.29e-11	-1.04e-15
$\alpha_{ij,\text{CO}_2,2410}$	5.85e+04	-1.02e+02	6.74e-02	-1.98e-05	2.17e-09
$\alpha_{ij,\text{CO}_2,3660}$	3.31e+00	5.56e-04	1.11e-06	-2.37e-10	2.04e-14
$\alpha_{ij,\text{CO}_2,5200}$	5.29e-02	5.22e-06	3.22e-08	1.72e-12	-2.08e-16
$\alpha_{ij,\text{CO},2143}$	-9.29e+01	1.86e-01	-1.26e-04	3.75e-08	-4.17e-12
$\alpha_{ij,\text{CO},4260}$	1.31e-01	-1.44e-05	4.42e-08	-9.52e-12	8.33e-16
$\alpha_{ij,\text{CH}_4,4220}$	2.49e+00	3.36e-04	7.64e-07	-1.58e-10	1.33e-14
$\alpha_{ij,\text{CH}_4,5861}$	3.98e-01	-5.69e-05	2.32e-07	-8.24e-12	8.33e-16

TABLE B.5: Polynomial coefficients $\alpha_{ij}(T)$ for temperature range of 2000-2500 [K] [7]

	b_0	b_1	b_2	b_3	b_4
$\beta_{ij,\text{H}_2\text{O},140}$	6.51e-02	-2.81e-05	7.25e-09	-7.41e-13	-6.48e-27
$\beta_{ij,\text{H}_2\text{O},1600}$	1.09e-02	5.49e-05	-6.04e-10	2.83e-11	-2.08e-15
$\beta_{ij,\text{H}_2\text{O},3760}$	1.43e-01	-7.99e-05	1.11e-07	3.76e-11	2.01e-26
$\beta_{ij,\text{H}_2\text{O},5350}$	6.68e-02	-5.39e-05	6.05e-08	1.54e-11	-2.87e-26
$\beta_{ij,\text{H}_2\text{O},7250}$	-7.21e-02	2.17e-04	-1.26e-07	8.00e-11	-6.25e-15
$\beta_{ij,\text{CO}_2,667}$	1.24e-01	-1.67e-04	3.92e-07	1.17e-10	-4.17e-15
$\beta_{ij,\text{CO}_2,960}$	1.77e-02	1.48e-05	6.54e-08	2.30e-10	-1.25e-14
$\beta_{ij,\text{CO}_2,1060}$	3.09e-01	-4.13e-04	4.97e-07	5.91e-10	-2.71e-14
$\beta_{ij,\text{CO}_2,2410}$	6.22e-01	-9.42e-04	1.35e-06	7.04e-10	-3.13e-14
$\beta_{ij,\text{CO}_2,3660}$	5.88e-01	-1.01e-03	1.03e-06	6.11e-10	-2.71e-14
$\beta_{ij,\text{CO}_2,5200}$	2.21e+00	-4.09e-03	3.79e-06	2.36e-09	-1.10e-13
$\beta_{ij,\text{CO},2143}$	-8.29e-02	2.09e-04	-1.26e-07	3.73e-11	-4.17e-15
$\beta_{ij,\text{CO},4260}$	7.79e-02	-5.15e-06	5.21e-08	-1.79E-11	2.08e-15
$\beta_{ij,\text{CH}_4,1310}$	-8.64e-01	2.25e-03	-2.06e-06	1.02e-09	1.40e-13
$\beta_{ij,\text{CH}_4,3020}$	-9.42e-01	2.32e-03	-2.05e-06	9.16e-10	1.04e-13
$\beta_{ij,\text{CH}_4,4220}$	-7.30e+00	1.73e-02	-1.48e-05	5.84e-09	9.42e-13
$\beta_{ij,\text{CH}_4,5861}$	-1.87e+01	4.44e-02	-3.83e-05	1.48e-08	2.31e-12

TABLE B.6: Polynomial coefficients $\beta_{ij}(T)$ for temperature range of 2000-2500 [K] [7]

Appendix C

Appendix: Exponential wide band parameters

TABLE C.1: Exponential Wide Band Parameters									
Gas	Fundamental band and its degeneracy η [cm^{-1}] and g	Characteristic band wavelength λ [μm]	Band wave-number centre η_C [cm^{-1}]	Vibrational transition quantum step $\delta_1, \delta_2, \dots, \delta_m$	Pressure parameters ($T_0 = 100 \text{ K}$) n b	Band absorption parameters: α_0, β_0 and ω_0 α_0 [$\text{cm}^{-1}/(\text{g}/\text{m}^2)$] β_0 ω_0 [cm^{-1}]			
H_2O	$m=3, \eta_1=3652, g_1=1$	Rotational >10 ^(a)	140	0, 0, 0	1 $8.6(T_0/T)^{0.5} + 0.5$	44205 0.14311 63.9			
	$\eta_2=1595, g_2=1$	6.3	1600	0, 1, 0	1 $8.6(T_0/T)^{0.5} + 0.5$	41.2 0.09427 56.4			
	$\eta_3=3756, g_3=1$	2.7 ^(b)	3760	0, 2, 0	1 $8.6(T_0/T)^{0.5} + 0.5$	0.19 0.13219 60.0			
				1, 0, 0 0, 0, 1		2.3 22.4			
CO_2		1.87	5350	0, 1, 1	1 $8.6(T_0/T)^{0.5} + 0.5$	3.0 0.08169 43.1			
		1.38	7250	1, 0, 1	1 $8.6(T_0/T)^{0.5} + 0.5$	2.5 0.11628 32.0			
		15	667	0, 1, 0	0.7 1.3	19.0 0.06157 12.7			
	$m=3, \eta_1=1351, g_1=1$	10.4	960	-1, 0, 1	0.8 1.3	2.47×10^{-9} 0.04017 13.4			
	$\eta_2=667, g_2=2$	9.4	1060	0, -2, 1 ^(d)	0.8 1.3	2.48×10^{-9} 0.11888 10.1			
	$\eta_3=2396, g_3=1$	4.3	2410 ^(c)	0, 0, 1	0.8 1.3	110.0 0.24723 11.2			
CO		2.7	3660	1, 0, 1	0.65 1.3	4.0 0.13341 23.5			
		2.0	5200	2, 0, 1	0.65 1.3	0.66 0.39305 34.5			
		4.7	2143	1	0.8 1.1	20.9 0.07506 25.5			
	$m=1, \eta_1=2143, g_1=1$	2.35	4260	2	0.8 1.0	0.14 0.16758 20.0			
CH_4	$\eta_1=2914, g_1=1$	7.66	1310	0, 0, 0, 1	0.8 1.3	28.0 0.08698 21.0			
	$\eta_2=1526, g_2=2$	3.31	3020	0, 0, 1, 0	0.8 1.3	46.0 0.06973 56.0			
	$\eta_3=3020, g_3=3$	2.37	4220	1, 0, 0, 1	0.8 1.3	2.9 0.35429 60.0			
	$\eta_4=1306, g_4=3$	1.71	5861	1, 1, 0, 1	0.8 1.3	0.42 0.68598 45.0			

TABLE C.1: Exponential wide band parameters [1]

Appendix D

Appendix: C++ Source code for E-EWBM

```
/******The participating gases already defined in this code include*****/  
  
0) H2O  
  
1) CO2  
  
2) CO  
  
3) CH4  
  
4) NO  
  
5) SO2  
  
/*****  
  
# <udf.h>  
  
#include <surf.h>  
  
#include <stdio.h>  
  
#include <math.h>  
  
#define N_Species 6  
  
#define N_FundBand 4
```

```
#define N_CombBand 6

#define N_GasUsed 4

#define INFIN 100

const double PI = 3.1415926535798932;

const double T_0 = 100.0;

const double P_0 = 101325.0;

/* ----- Universal constants (p. A1-4, IFRF Doc No G 08/y/2, 1993)
& Global variables ----- */

const double c0 = 299792458;

const double h = 6.626176e-34;

const double R_u = 8.31441e3;

const double N_A = 6.022045e23;

const double k_B = 1.380662e-23;

const double SB_delta = 5.67032e-8;

const double C_Euler = 0.577215664;

/**** Molecular weight of different species, [kg/kmol]*****/

const double MW_H2 = 2.01594;

const double MW_H2O = 18.01534;

const double MW_O2 = 31.99880;

const double MW_NO = 30.00610;

const double MW_HCN = 27.02582;

const double MW_NH3 = 17.03061;

const double MW_CH4 = 16.04303;

const double MW_C3H8 = 44.09000;
```

```
const double MW_CO = 28.01055;

const double MW_CO2 = 44.00995;

const double MW_SO2 = 64.06480;

const double MW_N2 = 28.01340;

double C1, C2;

int N_v0;

double PBFF_0_LamdaT, total_emissivity;

double X[N_Species] = 0.0;

double Pe[N_Species][N_CombBand] = 0.0;

double omega[N_Species][N_CombBand] = 0.0;

double alpha[N_Species][N_CombBand] = 0.0;

double beta[N_Species][N_CombBand] = 0.0;

double A_tot[N_Species][N_CombBand] = 0.0;

/* -----END of Universal constants and Global variables
----- */

int main()

{

int i = 0;

double Tg = 1500.;

double Ts = 1200.;

double P_tot = 101325.;

double L = 0.5;

double x_mol[4] = 0.2, 0.1, 0.02, 0.005;

EWBM_TotalEmissivity_OneGasMixture(Tg, Ts, P_tot, L, x_mol) ;
```

```

}

/*****Key Subroutine: to calculate the total emissivity for ONE
single gas condition by using EWBM *****/

/*****PRECISELY OK: Validated line-by-line and data-
by-data *****/

void EWBM_TotalEmissivity_OneGasMixture(double Tg, double Ts, double P_tot, dou-
ble L, double x_mol[])

double MW[N_Species] = 0.0;

int m[N_Species] = 0;

double eta[N_Species][N_FundBand]= 0;

int g[N_Species][N_FundBand] = 0;

int Nband[N_Species] = 0;

double eta_c[N_Species][N_CombBand]= 0.0;

int delta[N_Species][N_CombBand][N_FundBand] = 0;

double P_n[N_Species][N_CombBand] = 0.0;

double P_b[N_Species][N_CombBand] = 0.0;

double alpha_0[N_Species][N_CombBand]=0.0;

double beta_0[N_Species][N_CombBand] =0.0;

double omega_0[N_Species][N_CombBand]=0.0;

double a[N_Species][N_CombBand][5] = 0.0;

int delta_overlap[3][3]= 0;

double alpha_0_overlap[3] =0.0;

int i, j, k, vk, inc, NL;

double temp, aa1, aa2,bb1,bb2;

```

```

double alpha_overlap[3], aa1_overlap, aa2_overlap, bb1_overlap, bb2_overlap;

double beta_overlap[3], phi_T_overlap, ps_T, ps_T_overlap;

double u[N_Species][N_FundBand], u0[N_Species][N_FundBand];

double tau_H[N_Species][N_CombBand], B[N_Species][N_CombBand], eta_u[N_Species][N_CombBand],
tau_g[N_Species][N_CombBand], delta_eta[N_Species][N_CombBand]; double eta_L[N_Species]
[N_CombBand], eta_U[N_Species][N_CombBand], beta_est[N_Species][N_CombBand]; dou-
ble eta_series[1000], TauB_series[1000], Emiss_series[1000];

double tau_overlap[10];

int I_overlap[10], J_overlap[10];

/***INITIALIZAION *****/

/*****CONSTANT BLOCKS (! No need to change unless other band mod-
els are used !)*****/

C1 = 2*PI*h*pow(c0,2); /* 1st radiation constant [W/m2] */

C2 = h*c0/k_B; /*2nd radiation constant [m * K] */

/* H2O (i==0): Wide band model parameters */

MW[0] = 18.015;

m[0] = 3;

eta[0][0] = 3652.0;

eta[0][1] = 1595.0;

eta[0][2] = 3756.0;

g[0][0] = 1;

g[0][1] = 1;

g[0][2] = 1;

Nband[0] = 5;

/*H2O (i==0): Rotational band (j==0) */

```

```
eta.c[0][0] = 140;

delta[0][0][0] = 0;

delta[0][0][1] = 0;

delta[0][0][2] = 0;

P_n[0][0] = 1.0;

P_b[0][0] = 8.6*sqrt(T_0/Tg)+0.5;

alpha_0[0][0] = 44205.0;

beta_0[0][0] = 0.14311;

omega_0[0][0] = 69.3;

/*H2O (i==0): 6.3 micrometers (j==1) */

eta.c[0][1] = 1600;

delta[0][1][0] = 0;

delta[0][1][1] = 1;

delta[0][1][2] = 0;

P_n[0][1] = 1.0;

P_b[0][1] = 8.6*sqrt(T_0/Tg)+0.5;

alpha_0[0][1] = 41.2;

beta_0[0][1] = 0.09427;

omega_0[0][1] = 56.4;

a[0][1][0] = 0.84230766;

a[0][1][1] = 3.797542e-4;

a[0][1][2] = 6.680344e-7;

a[0][1][3] = 1.232428e-9;
```

```
a[0][1][4] = 3.988783e-14;

/*H2O (i==0): 2.7 micrometers (j==2) - three overlapped bands */

eta_c[0][2] = 3760;

P_n[0][2] = 1.0;

P_b[0][2] = 8.6*sqrt(T_0/Tg)+0.5;

beta_0[0][2] = 0.13219;

omega_0[0][2] = 60.0;

a[0][2][0] = 1.5409553;

a[0][2][1] = 7.483624e-4;

a[0][2][2] = 3.480733e-7;

a[0][2][3] = 2.212542e-9;

a[0][2][4] = 1.589963e-13;

delta_overlap[0][0] = 0;

delta_overlap[0][1] = 2;

delta_overlap[0][2] = 0;

alpha_0_overlap[0] = 0.19;

delta_overlap[1][0] = 1;

delta_overlap[1][1] = 0;

delta_overlap[1][2] = 0;

alpha_0_overlap[1] = 2.3;

delta_overlap[2][0] = 0;

delta_overlap[2][1] = 0;

delta_overlap[2][2] = 1;
```

```
alpha_0_overlap[2] = 22.4;

/*H2O (i==0): 1.87 micrometers (j==3) */

eta_c[0][3] = 5350;

delta[0][3][0] = 0;

delta[0][3][1] = 1;

delta[0][3][2] = 1;

P_n[0][3] = 1.0;

P_b[0][3] = 8.6*sqrt(T_0/Tg)+0.5;

alpha_0[0][3] = 3.0;

beta_0[0][3] = 0.08169;

omega_0[0][3] = 43.1;

a[0][3][0] = 0.74454804;

a[0][3][1] = 9.025019e-4;

a[0][3][2] = -2.695318e-7;

a[0][3][3] = 1.884587e-9;

a[0][3][4] = 7.466476e-14;

/*H2O (i==0): 1.38 micrometers (j==4) */

eta_c[0][4] = 7250;

delta[0][4][0] = 1;

delta[0][4][1] = 0;

delta[0][4][2] = 1;

P_n[0][4] = 1.0;

P_b[0][4] = 8.6*sqrt(T_0/Tg)+0.5;
```

```
alpha_0[0][4] = 2.5;

beta_0[0][4] = 0.11628;

omega_0[0][4] = 32.0;

a[0][4][0] = 0.79549686;

a[0][4][1] = 7.588211e-4;

a[0][4][2] = -4.698487e-7;

a[0][4][3] = 1.655432e-9;

a[0][4][4] = 1.032703e-13;

/* CO2 (i==1):*/

MW[1] = 44.010;

m[1] = 3;

eta[1][0] = 1351.0;

eta[1][1] = 667.0;

eta[1][2] = 2396.0;

g[1][0] = 1;

g[1][1] = 2;

g[1][2] = 1;

Nband[1] = 6;

/*CO2 (i==1): 15 micrometers (j==0) */

eta.c[1][0] = 667;

delta[1][0][0] = 0;

delta[1][0][1] = 1;

delta[1][0][2] = 0;
```

```
P_n[1][0] = 0.7;

P_b[1][0] = 1.3;

alpha_0[1][0] = 19.0;

beta_0[1][0] = 0.06157;

omega_0[1][0] = 12.7;

a[1][0][0] = 0.1961354;

a[1][0][1] = 4.6026302e-3;

a[1][0][2] = -6.542622e-7;

a[1][0][3] = 1.937692e-8;

a[1][0][4] = 4.682619e-15;

/* CO2 (i==1): 10.4 micrometers (j==1) */

eta_c[1][1] = 960;

delta[1][1][0] = -1;

delta[1][1][1] = 0;

delta[1][1][2] = 1;

P_n[1][1] = 0.8;

P_b[1][1] = 1.3;

alpha_0[1][1] = 2.47e-09;

beta_0[1][1] = 0.04017;

omega_0[1][1] = 13.4;

a[1][1][0] = -1.6560576;

a[1][1][1] = 1.4951764e-2;

a[1][1][2] = -2.222106e-5;
```

```
a[1][1][3] = 3.341932e-8;

a[1][1][4] = 6.393986e-13;

/* CO2 (i==1): 9.4 micrometers (j==2) */

eta_c[1][2] = 1060;

delta[1][2][0] = 0;

delta[1][2][1] = -2;

delta[1][2][2] = 1; /* original delta's of this band */ P_n[1][2] = 0.8;

P_b[1][2] = 1.3;

alpha_0[1][2] = 2.48e-09;

beta_0[1][2] = 0.11888;

omega_0[1][2] = 10.1;

a[1][2][0] = -1.6428941;

a[1][2][1] = 1.4896056e-2;

a[1][2][2] = -2.215055e-5;

a[1][2][3] = 3.338594e-8;

a[1][2][4] = 6.445583e-13;

/*CO2 (i==1): 4.3 micrometers (j==3) */

eta_c[1][3] = 2410;

delta[1][3][0] = 0;

delta[1][3][1] = 0;

delta[1][3][2] = 1;

P_n[1][3] = 0.8;

P_b[1][3] = 1.3;
```

```
alpha_0[1][3] = 110.0;

beta_0[1][3] = 0.24723;

omega_0[1][3] = 11.2;

a[1][3][0] = -0.4652004;

a[1][3][1] = 8.6506412e-3;

a[1][3][2] = -1.092158e-5;

a[1][3][3] = 2.418113e-8;

a[1][3][4] = 6.129179e-14;

/*CO2 (i==1): 2.7 micrometers (j==4) */

eta_c[1][4] = 3660;

delta[1][4][0] = 1;

delta[1][4][1] = 0;

delta[1][4][2] = 1;

P_n[1][4] = 0.65;

P_b[1][4] = 1.3;

alpha_0[1][4] = 4.0;

beta_0[1][4] = 0.13341;

omega_0[1][4] = 23.5;

a[1][4][0] = -1.5631418;

a[1][4][1] = 1.4952999e-2;

a[1][4][3] = 3.807809e-8;

a[1][4][4] = 1.421920e-13;

/* CO2 (i==1): 2.0 micrometers (j==5) */
```

```
eta.c[1][5] = 5200;

delta[1][5][0] = 2;

delta[1][5][1] = 0;

delta[1][5][2] = 1;

P_n[1][5] = 0.65;

P_b[1][5] = 1.3;

alpha_0[1][5] = 0.066;

beta_0[1][5] = 0.39305;

omega_0[1][5] = 34.5;

a[1][5][0] = -2.3330982;

a[1][5][1] = 1.9693219e-2;

a[1][5][2] = -3.481327e-5;

a[1][5][3] = 5.023159e-8;

a[1][5][4] = 7.235694e-15;

/* CO (i==2) */

MW[2] = 28.011;

m[2] = 1;

eta[2][0] = 2143.0;

g[2][0] = 1;

Nband[2] = 2;

/* CO (i==2): 4.7 micrometers (j==0) */

eta.c[2][0] = 2143;

delta[2][0][0] = 1;
```

```
P_n[2][0] = 0.8;

P_b[2][0] = 1.1;

alpha_0[2][0] = 20.9;

beta_0[2][0] = 0.07506;

omega_0[2][0] = 25.5;

a[2][0][0] = 0.96845850;

a[2][0][1] = -3.194073e-4;

a[2][0][2] = 1.586938e-6;

a[2][0][3] = -4.954279e-10;

a[2][0][4] = 5.841911e-14;

/* CO (i==2): 2.35 micrometers (j==1) */

eta_c[2][1] = 4260;

delta[2][1][0] = 2;

P_n[2][1] = 0.8;

P_b[2][1] = 1.0;

alpha_0[2][1] = 0.14;

beta_0[2][1] = 0.16758;

omega_0[2][1] = 20.0;

a[2][1][0] = 0.98939747;

a[2][1][1] = -5.327946e-4;

a[2][1][2] = 2.139065e-6;

a[2][1][3] = -6.579432e-10;

a[2][1][4] = 7.632673e-14;
```

```
/* CH4 (i==3): */  
  
MW[3] = 16.043;  
  
m[3] = 4;  
  
eta[3][0] = 2914.0;  
  
eta[3][1] = 1526.0;  
  
eta[3][2] = 3020.0;  
  
eta[3][3] = 1306.0;  
  
g[3][0] = 1;  
  
g[3][1] = 2;  
  
g[3][2] = 3;  
  
g[3][3] = 3;  
  
Nband[3] = 4;  
  
/* CH4 (i==3): 7.66 micrometers (j==0) */  
  
eta_c[3][0] = 1310;  
  
delta[3][0][0] = 0;  
  
delta[3][0][1] = 0;  
  
delta[3][0][2] = 0;  
  
delta[3][0][3] = 1;  
  
P_n[3][0] = 0.8;  
  
P_b[3][0] = 1.3;  
  
alpha_0[3][0] = 28.0;  
  
beta_0[3][0] = 0.08698;  
  
omega_0[3][0] = 21.0;
```

```
a[3][0][0] = 1.5648427;
a[3][0][1] = -6.8944212e-3;
a[3][0][2] = 2.54499e-5;
a[3][0][3] = -2.844937e-8;
a[3][0][4] = 2.731267e-11;

/* CH4 (i==3): 3.31 micrometers (j==1) */

eta_c[3][1] = 3020;

delta[3][1][0] = 0;
delta[3][1][1] = 0;
delta[3][1][2] = 1;
delta[3][1][3] = 0;

P_n[3][1] = 0.8;
P_b[3][1] = 1.3;

alpha_0[3][1] = 46.0;
beta_0[3][1] = 0.06973;
omega_0[3][1] = 56.0;

a[3][1][0] = 1.4335916;
a[3][1][1] = -6.7502069e-3;
a[3][1][2] = 2.666333e-5;
a[3][1][3] = -3.183975e-8;
a[3][1][4] = 2.796224e-11;

/* CH4 (i==3): 2.37 micrometers (j==2) */

eta_c[3][2] = 4220;
```

```
delta[3][2][0] = 1;

delta[3][2][1] = 0;

delta[3][2][2] = 0;

delta[3][2][3] = 1;

P_n[3][2] = 0.8;

P_b[3][2] = 1.3;

alpha_0[3][2] = 2.9;

beta_0[3][2] = 0.35429;

omega_0[3][2] = 60.0;

a[3][2][0] = 4.5236603;

a[3][2][1] = -2.4705987e-2;

a[3][2][2] = 6.361541e-5;

a[3][2][3] = -6.608218e-8;

a[3][2][4] = 4.358251e-11;

/*CH4 (i==3): 1.71 micrometers (j==3)*/

eta_c[3][3] = 5861;

delta[3][3][0] = 1;

delta[3][3][1] = 1;

delta[3][3][2] = 0;

delta[3][3][3] = 1;

P_n[3][3] = 0.8;

P_b[3][3] = 1.3;

alpha_0[3][3] = 0.42;
```

```
beta_0[3][3] = 0.68598;

omega_0[3][3] = 45.0;

a[3][3][0] = 5.2699323;

a[3][3][1] = -3.0613825e-2;

a[3][3][2] = 8.013098e-5;

a[3][3][3] = -8.636448e-8;

a[3][3][4] = 5.610116e-11;

/* NO (i==4): */

MW[4] = 30.006;

m[4] = 1;

eta[4][0] = 1876.0;

g[4][0] = 1;

Nband[4] = 1;

/* NO (i==4): 5.3 micrometers (j==0)*/

eta_c[4][0] = 1876;

delta[4][0][0] = 1;

P_n[4][0] = 0.65;

P_b[4][0] = 1.0;

alpha_0[4][0] = 9.0;

beta_0[4][0] = 0.18050;

omega_0[4][0] = 20.0;

a[4][0][0] = 0.89600558;

a[4][0][1] = -6.343311e-5;
```

```
a[4][0][2] = 1.674182e-6;

a[4][0][3] = -5.349355e-10;

a[4][0][4] = 6.402298e-14;

/* SO2 (i==5) */

MW[5] = 64.065;

m[5] = 3;

eta[5][0] = 1151.0;

eta[5][1] = 519.0;

eta[5][2] = 1361.0;

g[5][0] = 1;

g[5][1] = 1;

g[5][2] = 1;

Nband[5] = 5;

/* SO2 (i==5): 19.27 micrometers (j==0) */

eta_c[5][0] = 519;

delta[5][0][0] = 0;

delta[5][0][1] = 1;

delta[5][0][2] = 0;

P_n[5][0] = 0.7;

P_b[5][0] = 1.28;

alpha_0[5][0] = 4.22;

beta_0[5][0] = 0.05291;

omega_0[5][0] = 33.08;
```

```
a[5][0][0] = 0.35841519;

a[5][0][1] = 4.264312e-3;

a[5][0][2] = -1.854302e-6;

a[5][0][3] = 3.893398e-8;

a[5][0][4] = -5.785739e-15;

/* SO2 (i==5): 8.68 micrometers (j==1) */

eta_c[5][1] = 1151;

delta[5][1][0] = 1;

delta[5][1][1] = 0;

delta[5][1][2] = 0;

P_n[5][1] = 0.7;

P_b[5][1] = 1.28;

alpha_0[5][1] = 3.674;

beta_0[5][1] = 0.05952;

omega_0[5][1] = 24.83;

a[5][1][0] = 0.23458589;

a[5][1][1] = 5.1324164e-3;

a[5][1][2] = -7.295804e-6;

a[5][1][3] = 4.034948e-8;

a[5][1][4] = -5.677245e-14;

/*SO2 (i==5): 7.35 micrometers (j==2) */

eta_c[5][2] = 1361;

delta[5][2][0] = 0;
```

```
delta[5][2][1] = 0;

delta[5][2][2] = 1;

P_n[5][2] = 0.65;

P_b[5][2] = 1.28;

alpha_0[5][2] = 29.97;

beta_0[5][2] = 0.49299;

omega_0[5][2] = 8.78;

a[5][2][0] = 0.12411054;

a[5][2][1] = 5.941862e-3;

a[5][2][2] = -9.349168e-6;

a[5][2][3] = 4.056027e-8;

a[5][2][4] = -6.92483e-14;

/*SO2 (i==5): 4.34 micrometers (j==3) */

eta_c[5][3] = 2350;

delta[5][3][0] = 2;

delta[5][3][1] = 0;

delta[5][3][2] = 0;

P_n[5][3] = 0.6;

P_b[5][3] = 1.28;

alpha_0[5][3] = 0.423;

beta_0[5][3] = 0.47513;

omega_0[5][3] = 16.45;

a[5][3][0] = 0.33478312;
```

```

a[5][3][1] = 5.5456959e-3;

a[5][3][2] = -1.230914e-5;

a[5][3][3] = 5.306223e-8;

a[5][3][4] = -2.709801e-13;

/*SO2 (i==5): 4.0 micrometers (j==4) */

eta_c[5][4] = 2512;

delta[5][4][0] = 1;

delta[5][4][1] = 0;

delta[5][4][2] = 1;

P_n[5][4] = 0.6;

P_b[5][4] = 1.28;

beta_0[5][4] = 0.58937;

omega_0[5][4] = 10.91;

a[5][4][0] = -0.79547401;

a[5][4][1] = 1.2556243e-2;

a[5][4][2] = -2.762971e-5;

a[5][4][3] = 6.52692e-8;

a[5][4][4] = -2.25453e-13;

/* if more absorbing gases need to be considered, please add their model
parameters HERE! Other absorbing species 1; Other absorbing species 2;
.....; Other absorbing species N; */

/*————— END of CONSTANT BLOCKS —————*/

/*****STEP 1: For each gas, calculate *****/

/***** (1) the mass path length product X[i], [g/m2] *****/

```

```

for(i=0; i<N_GasUsed; i++)

{

X[i] = (x_mol[i]*P_tot*MW[i])/((R_u/1000.)*Tg)*L;

}

/***** STEP 2: For each band of each gas, calculate *****/

/***** (1) dimensionless equivalent broadening pressure, Pe [-],*****/

/*****(2) band width parameter, omega [cm-1]; *****/

/***** (3) integrated band intensity, alpha [1/(cm2 * atm)]*****/;

/*****(4) mean line-width to spacing ratio, beta [-]* *****/

/* (1-2) Pe [-], omega [cm-1]: Effective broadening pressure and Band width
parameter, of species i, band j*/

for(i=0; i<N_GasUsed; i++)

{

for (j=0; j<Nband[i]; j++)

{

Pe[i][j] = pow(((P_tot/P_0)*(1+x_mol[i]*(P_b[i][j]-1))), P_n[i][j]);

omega[i][j] = omega_0[i][j]*sqrt(Tg/T_0);

}

}

/* (3) alpha[i][j] in unit of [cm-2 * atm-1]: Integrtaed band intensity of species i, band
j */

for(i=0; i<N_GasUsed; i++)

{

for (k=0; k< m[i]; k++)

```

```

{
u[i][k] = C2*(100.0*eta[i][k])/Tg;

u0[i][k] = C2*(100.0*eta[i][k])/T_0;

}

}

alpha[0][0]= alpha_0[0][0]*exp(-9.0*sqrt(T_0/Tg));

/*calculation of integrated band intensity for > 10 micro of water*/

alpha[0][1]=alpha_0[0][1]; /*calculation of integrated band intensity for band
6.3 micro of water */

/*calculation of integrated band intensity for band 2.7 micro of water*/

i=0;

j=2;

aa1_overlap=0;

aa2_overlap=0;

alpha[0][2]=0;

for(j=0;j<1;j++)

{

for(k=0;k<m[0];k++)

{

aa1_overlap=aa1_overlap+u[0][k]*delta_overlap[j][k];

aa2_overlap=aa2_overlap+u0[0][k]*delta_overlap[j][k];

}

}

/*calculation of PSI(T) and PSI(T0) */

bb1_overlap=2*(1/(1-(exp(-(eta[0][1]*C2*100.0)/Tg))))*(1/(1-(exp(-(eta[0][1]*C2*100.0)/Tg))));

```

```

bb2_overlap=2*(1/(1-(exp(-(eta[0][1]*C2*100.0)/T_0))))*(1/(1-(exp(-(eta[0][1]*C2*100.0)/T_0))));

ps_T_overlap = bb1_overlap/bb2_overlap;

/*refer to look up table 2.1 and Appendix C, the value of band intensity
alpha_0_overlap for water for 2 and 3 overlapping band of 2.7 micro =inte-
grated band intensity for 2 and 3 overlapping band of 2.7 micro for water*/

/* Total integrated band intensity for overlapping band band at 2.7 micro
is*/

alpha[0][2]=alpha_0_overlap[0]*((1-exp(-aa1_overlap))/(1-exp(-aa2_overlap)))*ps_T_overlap+
alpha_0_overlap[1]+alpha_0_overlap[2];

}

/* calculation of integrated band intensity for 1.87 micro for water */

i=0;

j=3;

aa1=0;

aa2=0;

for(k=0;k<m[i];k++)

{

aa1=aa1+u[i][k]*delta[i][j][k];

aa2=aa2+u0[i][k]*delta[i][j][k];

}

/*calculation of PSI(T) and PSI(T0)*/

bb1 = (1./(1-(exp(-(eta[0][1]*C2)/Tg))))*(1./(1-(exp(-(eta[0][2]*C2)/Tg))));

bb2 = (1./(1-(exp(-(eta[0][1]*C2)/T_0))))*(1./(1-(exp(-(eta[0][2]*C2)/T_0))));

ps_T= bb1/bb2;

alpha[0][3]= ps_T*alpha_0[0][3]*(((1-exp(-aa1)))/(1-exp(-aa2)));

```

```

/*calculation of integrated band intensity for 1.38 micro of water*/

/* for water band of 1.38 micro (i==0;j==4) */

i=0;

j=4;

aa1=0;

aa2=0;

for (k=0;k<m[i];k++)

{

aa1=aa1+u[i][k]*delta[i][j][k];

aa2=aa2+u0[i][k]*delta[i][j][k];

}

/*calculation of PSI(T) and PSI(T0) */

bb1= (1/(1-(exp(-(eta[0][0]*C2)/Tg))))*(1/(1-(exp(-(eta[0][2]*C2)/Tg))));

bb2=(1/(1-(exp(-(eta[0][0]*C2)/T_0))))*(1/(1-(exp(-(eta[0][2]*C2)/T_0))));

ps_T=bb1/bb2;

alpha[0][4]=alpha_0[0][4]*((1-exp(-aa1))/(1-exp(-aa2)))*ps_T;

/*calculation of integrated band intensity for carbon dioxide*/

/*calculation of integrated band intensity for band 15 of CO2*/

i=1;

j=0;

alpha[1][0]=alpha_0[1][0];

/*refer to look up table 2.1 and Appendix C, the value of band absorption
parameter alpha_0=integrated band intensity*/

/*calculation of integrated band intensity for band 10.4 of CO2*/

```

```

i=1;

j=1;

aa1=0;

aa2=0;

for(k=0;k<m[i];k++)

{

aa1=aa1+u[i][k]*delta[i][j][k];

aa2=aa2+u0[i][k]*delta[i][j][k];

}

/*calculation of PSI(T) and PSI(T0)*/

bb1=(exp(-(eta[1][0]*C2)/Tg))*(2-(exp(-(eta[1][0]*C2)/Tg)))*(1/(1-(exp(-(eta[1][0]*C2)/Tg))))
*(1/(1-(exp(-(eta[1][2]*C2)/Tg))));

bb2=(exp(-(eta[1][0]*C2)/T_0))*(2-(exp(-(eta[1][0]*C2)/T_0)))*(1/(1-(exp(-(eta[1][0]*C2)/T_0))))
*(1/(1-(exp(-(eta[1][2]*C2)/T_0))));

ps_T=bb1/bb2;

alpha[1][1]=alpha_0[1][1]*((1-exp(-aa1))/(1-exp(-aa2)))*ps_T;

/*calculation of integrated band intensity for band 9.4 of CO2*/

i=1;

j=2;

aa1=0;

aa2=0;

for(k=0;k<m[i];k++)

{

aa1=aa1+u[i][k]*delta[i][j][k];

```

```

aa2=aa2+u0[i][k]*delta[i][j][k];

}

/*calculation of PSI(T) and PSI(T0)*/

bb1=(exp(-(eta[1][0]*C2)/Tg))*(2-(exp(-(eta[1][0]*C2)/Tg)))*(1/(1-(exp(-(eta[1][0]*C2)/Tg))))
*(1/(1-(exp(-(eta[1][2]*C2)/Tg))));

bb2=(exp(-(eta[1][0]*C2)/T_0))*(2-(exp(-(eta[1][0]*C2)/T_0)))*(1/(1-(exp(-(eta[1][0]*C2)/T_0))))
*(1/(1-(exp(-(eta[1][2]*C2)/T_0))));

ps_T=bb1/bb2;

alpha[1][2]=alpha_0[1][2]*((1-exp(-aa1))/(1-exp(-aa2)))*ps_T;

/*calculation of integrated band intensity for band 4.3 of CO2*/

i=1;

j=3;

alpha[1][3]=alpha_0[1][3];

/*refer to look up table 2.1 and Appendix C, the value of band absorption
parameter alpha_0=integrated band intensity*/

/* calculation of integrated band intensity for band 2.7 of CO2 */

i=1;

j=4;

aa1=0;

aa2=0;

for(k=0;k<m[i];k++)

{

aa1=aa1+u[i][k]*delta[i][j][k];

aa2=aa2+u0[i][k]*delta[i][j][k];

```

```

}

/*calculation of PSI(T) and PSI(T0) */

bb1= (1/(1-(exp(-(eta[1][0]*C2)/Tg))))*(1/(1-(exp(-(eta[1][2]*C2)/Tg))));

bb2= (1/(1-(exp(-(eta[1][0]*C2)/T_0))))*(1/(1-(exp(-(eta[1][2]*C2)/T_0))));

ps_T=bb1/bb2;

alpha[1][4]=alpha_0[1][4]*((1-exp(-aa1))/(1-exp(-aa2)))*ps_T;

/* calculation of integrated band intensity for band 2.0 of CO2*/

i=1;

j=5;

aa2=0;

for(k=0;k<m[i];k++)

{

aa1=aa1+u[i][k]*delta[i][j][k];

aa2=aa2+u0[i][k]*delta[i][j][k];

}

/*calculation of PSI(T) and PSI(T0) */

bb1= ((1/(1-(exp(-(eta[1][0]*C2*100.0)/Tg))))*(1/(1-(exp(-(eta[1][0]*C2*100.0)/Tg))))*(1/(1-
(exp(-(eta[1][2]*C2*100.0)/Tg))));

bb2= ((1/(1-(exp(-(eta[1][0]*C2*100.0)/T_0))))*(1/(1-(exp(-(eta[1][0]*C2*100.0)/T_0))))*(1/(1-
(exp(-(eta[1][2]*C2*100.0)/T_0))));

ps_T=bb1/bb2;

alpha[1][5]=alpha_0[1][5]*((1-exp(-aa1))/(1-exp(-aa2)))*ps_T;

/*calculation of integrated band intensity for band 4.7 of CO */

i=2;

```

```

j=0;

alpha[2][0]=alpha_0[2][0];

/*refer to look up table 2.1 and appendix C, the value of band absorption
parameter alpha_0=integrated band intensity*/

/*calculation of integrated band intensity for band 2.35 of CO*/

i=2;

j=1;

aa1=0;

aa2=0;

for(k=0;k<m[i];k++)

{

aa1=aa1+u[i][k]*delta[i][j][k];

aa2=aa2+u0[i][k]*delta[i][j][k];

}

/*calculation of PSI(T) and PSI(T0) */

bb1= 2*((1/(1-(exp(-(eta[2][0]*C2*100.0)/Tg))))*(1/(1-(exp(-(eta[2][0]*C2*100.0)/Tg)))));

bb2= 2*((1/(1-(exp(-(eta[2][0]*C2*100.0)/T_0))))*(1/(1-(exp(-(eta[2][0]*C2*100.0)/T_0)))));

ps_T=bb1/bb2;

alpha[2][1]=alpha_0[2][1]*((1-exp(-aa1))/(1-exp(-aa2)))*ps_T;

/*calculation of integrated band intensity for band CH4 7.66*/

i=3;

j=0;

alpha[3][0]=alpha_0[3][0];

```

```

/*refer to look up table 2.1 and appendix C, the value of band absorption
parameter alpha_0=integrated band intensity*/

/*calculation of integrated band intensity for band CH4 3.31*/

i=3;

j=1;

alpha[3][1]=alpha_0[3][1];

/*refer to look up table 2.1 and appendix C, the value of band absorption
parameter alpha_0=integrated band intensity*/

/*calculation of integrated band intensity for band CH4 2.37*/

i=3;

j=2;

aa1=0;

aa2=0;

for(k=0;k<m[3];k++)

{

aa1=aa1+u[i][k]*delta[i][j][k];

aa2=aa2+u0[i][k]*delta[i][j][k];

}

/*calculation of PSI(T) and PSI(T0) */

bb1= 3*((1/(1-(exp(-(eta[3][0]*C2*100.0)/Tg))))*(1/(1-(exp(-(eta[3][3]*C2*100.0)/Tg))));

bb2= 3*((1/(1-(exp(-(eta[3][0]*C2*100.0)/T_0))))*(1/(1-(exp(-(eta[3][3]*C2*100.0)/T_0))));

ps_T=bb1/bb2;

alpha[3][2]=alpha_0[3][2]*((1-exp(-aa1))/(1-exp(-aa2)))*ps_T;

/*calculation of integrated band intensity for band CH4, 1.71*/

```

```

i=3;

j=3;

aa1=0;

aa2=0;

for(k=0;k<m[i];k++)

{

aa1=aa1+u[i][k]*delta[i][j][k];

aa2=aa2+u0[i][k]*delta[i][j][k];

}

/*calculation of PSI(T) and PSI(T0) */

bb1= 6*(1/(1-(exp((-eta[3][0]*C2*100.0)/Tg))))*(1/(1-(exp((-eta[3][3]*C2*100.0)/Tg))))*(1/(1-
(exp(-(eta[3][1]*C2*100.0)/Tg))));

bb2= 6*(1/(1-(exp((-eta[3][0]*C2*100.0)/T_0))))*(1/(1-(exp((-eta[3][3]*C2*100.0)/T_0))))*(1/(1-
(exp((-eta[3][1]*C2*100.0)/T_0))));

ps_T=bb1/bb2;

alpha[3][3]=alpha_0[3][3]*((1-exp(-aa1))/(1-exp(-aa2)))*ps_T;

/* ——— Approximate estimate of the Line-Width To Spacing Ratio, beta_est[i][j]:
——— */

for(i=0; i<N_GasUsed; i++)

{

for (j=0; j<Nband[i]; j++)

{

if ((i==0)&&(j==0))

{

```

```

beta[i][j] = beta_0[i][j]*sqrt(T_0/Tg);

continue;

}

beta[i][j] = beta_0[i][j]*sqrt(T_0/Tg)*(a[i][j][0]+a[i][j][1]*Tg+a[i][j][2]*pow(Tg,2)
+a[i][j][3]*pow(Tg,3)+a[i][j][4]*pow(Tg,4));

}

}

/***** STEP 3-4: For each band of each gas, calculate*****/

/***** (1) total band absortance, A_tot[i][j], [g/m2]; *****/

/***** (2) band transmissivity, tau_g[i][j] *****/

/***** (3) then the band width, delta_eta [cm-1]; and the Upper and Lower
limits of each band *****/

for(i=0; i<N_GasUsed; i++)

{

for (j=0; j<Nband[i]; j++)

{

tau_H[i][j] = (alpha[i][j]*X[i])/omega[i][j]; B[i][j] = beta[i][j]*Pe[i][j];

eta_u[i][j] = 1/sqrt(B[i][j]/tau_H[i][j]*(1.+B[i][j]/tau_H[i][j]));

if ((i==0) && (j==0))

{

A_tot[i][j] = omega[i][j] * BandAbsorp_Aij(beta[i][j], Pe[i][j], eta_u[i][j]);

if (B[i][j]<1.)

{

if ((tau_H[i][j]>=0.)&&(tau_H[i][j]<=B[i][j])) tau_g[i][j] = 0.9;

```

```

else if

((tau_H[i][j]>=B[i][j])&&(tau_H[i][j]<=(1./B[i][j])))

tau_g[i][j] = 0.5*(1+omega[i][j]*B[i][j]/A_tot[i][j]);

else tau_g[i][j] = omega[i][j]/A_tot[i][j];

}

else

{

if ((tau_H[i][j]>=0.) &&(tau_H[i][j]<=1.)) tau_g[i][j] = 0.9;

else tau_g[i][j] = omega[i][j]/A_tot[i][j];

}

}

else

{

if (B[i][j]<1.)

{

if ((tau_H[i][j]>=0.) &&(tau_H[i][j]<=B[i][j]))

{

A_tot[i][j] = omega[i][j]*tau_H[i][j]; tau_g[i][j] = 0.9;

}

else if ((tau_H[i][j]>=B[i][j]) && (tau_H[i][j]<=(1./B[i][j])))

{

A_tot[i][j] = omega[i][j]*(sqrt(4*B[i][j]*tau_H[i][j])-B[i][j]);

tau_g[i][j] = 0.5*(1+omega[i][j]*B[i][j]/A_tot[i][j]);

```

```
}  
  
else  
  
{  
  
A_tot[i][j] = omega[i][j]*(log(tau_H[i][j]*B[i][j])+2-B[i][j]);  
  
tau_g[i][j] = omega[i][j]/A_tot[i][j];  
  
}  
  
}  
  
else  
  
{  
  
if ((tau_H[i][j]>=0.) &&(tau_H[i][j]<=1.))  
  
{  
  
A_tot[i][j] = omega[i][j]*tau_H[i][j]; tau_g[i][j] = 0.9;  
  
}  
  
else  
  
{  
  
A_tot[i][j] = omega[i][j]*(log(tau_H[i][j])+1.);  
  
tau_g[i][j] = omega[i][j]/A_tot[i][j];  
  
}  
  
}  
  
}  
  
if (tau_g[i][j]>0.9) tau_g[i][j] = 0.9;  
  
if (x_mol[i]==0.0) A_tot[i][j]=0.0;  
  
delta_eta[i][j] = A_tot[i][j]/(1-tau_g[i][j]);
```

```

eta.L[i][j] = eta.c[i][j]-0.5*delta_eta[i][j];

eta.U[i][j] = eta.c[i][j]+0.5*delta_eta[i][j];

if (eta.L[i][j]<0.) eta.L[i][j]=0.0;

}

}

/* The only special band: CO2, 4.3micro (i=1,j=3) is an assymmetric band,
and the given eta_c[1][3]=2410 is actually the upper head wavenumber!! */

eta.U[1][3] = eta.c[1][3];

eta.L[1][3] = eta.U[1][3] - delta_eta[1][3];

if (eta.L[1][3]<0.) eta.L[1][3]=0.0;

/*****STEP 5: Sort the band limits and arrange in increasing order*****/

/**the Lower limit of block (or interval) i+1 being same as the Upper limit
of block i***/

NL = 0;

for(i=0; i<N_GasUsed; i++)

{

for (j=0; j<Nband[i]; j++)

{

eta_series[NL] = eta.L[i][j];

NL = NL+1;

eta_series[NL] = eta.U[i][j];

NL = NL+1;

}

}

}

```

```
inc=1;

do {

inc *= 3;

inc++;

}

while (inc < NL);

do {

inc /= 3;

for (i=inc+1; i<NL; i++)

{

temp=eta_series[i];

j=i;

while (eta_series[j-inc] > temp)

{

eta_series[j] = eta_series[j-inc];

j -= inc;

if (j <= inc) break;

}

eta_series[j]=temp;

}

}

while (inc > 1);

eta_series[NL] = 100000.0;
```

```

/***** STEP 6: By comparing whether the limits of a given block belongs
to none, one or several absorption bands, *****/

/**** compute the block transmissivity as the product of the band transmis-
sivity to which the block belongs. ****/

/***** STEP 7: Multiply each block emissivity by the fraction of blockbody
radiation within the block limits, and */

/***** sum over all the blocks, gives the total emissivity. – the last step!
*****/

total_emissivity = 0.0;

for(k=0; k<NL; k++)

{

TauB_series[k] = 1.0;

for(i=0; i<N_GasUsed; i++)

{ for (j=0; j<Nband[i]; j++)

{

if ((eta_series[k]>=eta_L[i][j]) & (eta_series[k+1]<=eta_U[i][j])) TauB_series[k] = TauB_series[k]
*tau_g[i][j];

}

}

Emiss_series[k] = (1-TauB_series[k]) * (PBFF(eta_series[k],Tg)-PBFF(eta_series[k+1],Tg));

total_emissivity = total_emissivity + Emiss_series[k];

}

}

/***** Other Subroutines *****/

/***** All validated! *****/

```

```
/* (1) OK ** Subroutine to calculate the Factorial of an integer up to 170!
(ref: c6_1.pdf) *****/

double FACTORIAL(int n)

/* Returns the value n! as a floating-point number.*/

{

double gammln(double xx);

static int ntop=4;

static double a[33]=1.0,1.0,2.0,6.0,24.0;

int j;

if (n < 0)

{

printf("Error: Negative factorial in routine FACTORIAL!");

}

if (n > 32)

{

return exp(gammln(n+1.0));

}

while (ntop<n)

{

j=ntop++;

a[ntop]=a[j]*ntop;

}

return a[n];

}
```

```

double gammln(double xx)
{
double x,y,tmp,ser;

static double

cof[6]={76.180091,-86.50532, 24.0140982 -1.2317395,0.1208650e-2,-0.539523e-5};

int j;

y=x=xx;

tmp=x+5.5;

tmp -= (x+0.5)*log(tmp);

ser=1.000000000190015;

for (j=0;j<=5;j++) ser += cof[j]/++y;

return -tmp+log(2.5066282746310005*ser/x);
}

/* (2) OK ** Subroutine to calculate Planck Blackbody Fractional Function
(PBFF) *****/

double PBFF(double wavenumber, double GasTemp)
{ double lamda, y, sum;

int nn;

lamda = 1/(wavenumber*100.0);

y = C2/(lamda*GasTemp);

sum = 0.0;

if (y>=2)
{
for (nn=1; nn<50; nn++)

```

```

{
sum = sum + (exp(-nn*y)/nn) * (pow(y,3) + 3.*pow(y,2)/nn + 6.*y/(pow(nn,2)) +
6./((pow(nn,3))));
}

PBFF_0_LamdaT = sum * (15./pow(PI,4));

} else

{

PBFF_0_LamdaT= 1-((15./pow(PI,4))*(pow(y,3))*((1./3)-(y/8)+(pow(y,2)/60)-(pow(y,4)/5040)
+(pow(y,6)/272160)-(pow(y,8)/13305600)));

}

return PBFF_0_LamdaT;

}

/* (3) OK ** Subroutine to calculate Exponential Integral Of Order One for
double x, E1(x) *****/

double E1(double xx)

{

double AE1[6] = -0.57721566, 0.99999193, -0.24991055, 0.05519968, -0.00976004, 0.00107857;

double BE1[4] = 8.5733287401, 18.0590169730, 8.6347608925, 0.2677737343;

double CE1[4] = 9.5733223454, 25.6329561486, 21.0996530827, 3.9584969228;

double sum;

if (xx<0.0) sum=-1.0e-20;

else if (xx<1.0e-15) sum = 1.0e+20;

else if (xx<=1.0) sum = (AE1[0]+AE1[1]*xx+AE1[2]*pow(xx,2.)+AE1[3]*pow(xx,3.)
+AE1[4]*pow(xx,4.)+AE1[5]*pow(xx,5.)) - log(xx);

else sum = ((BE1[3]+BE1[2]*xx+BE1[1]*pow(xx,2.) +BE1[0]*pow(xx,3.)

```

```

+pow(xx,4.))/(CE1[3]+CE1[2]*xx
+CE1[1]*pow(xx,2.) +CE1[0]*pow(xx,3.)+pow(xx,4.))/(xx*exp(xx));

return sum;

}

/* (4) OK: Analytical expression for Theoretical Band Absorptance, A_ij
(Eqn (10.124) in Modest) */

double BandAbsorp_Aij(double betax, double Pex, double eta_ux)

{

double E1(double xx);

double x1,x2,x3,x4,x5;

x1 = betax*Pex*eta_ux;

x2 = eta_ux/2.0;

x3 = x2*(1.0+2.0*betax*Pex);

x4 = pow(x1,2)*x2/x3;

x5 = 2.0*E1(x1) + E1(x2) - E1(x3) + log(x4) + 2.0*C_Euler;

return x5;

}

```

Bibliography

- [1] C. Yin. Advanced modeling of oxy-fuel combustion of natural gas, January 2011. Department of Energy Technology, Aalborg University.
- [2] N. Lallemand R. Weber. Radiative property models for computing non-sooty natural gas flames. Part 1: Report on Radiation Modelling. IFRF Doc No G08/y/2, December 1993. International Flame Research Foundation.
- [3] U. Bollettini F. Breussin N. Lallemand, R. Weber. Mathematical modelling of oxy-natural gas flames. IFRF Doc. No. F85/y/6, May 1997. International Flame Foundation Research.
- [4] C. Yin. Refined weighted sum of gray gases model for air-fuel combustion and its impacts. *Energy and fuels*, 27:6287–6294, 2013.
- [5] R. Nair. Simulation of the BERL 300 kW Natural Gas flame using FLUENT/UNS. URL <http://content.lib.utah.edu/utis/getfile/collection/AFRC/id/11213/filename/image>. Accessed: 10/04/2016.
- [6] ANSYS Inc. *ANSYS Fluent tutorial, Chapter 17: Using the Non-Premixed Combustion Model*. November 2013.
- [7] L. Yan G. Yue, B. He. Application of an efficient exponential wide band model for the natural gas combustion simulation in a 300 kW BERL burner furnace. *Applied Thermal Engineering*, 94:209–220, 2016.
- [8] J. Braz. Thermal Radiation in Combustion Systems. URL http://www.scielo.br/scielo.php?script=sci_arttext&pid=S0100-73861999000300014. Accessed: 28/04/2016.
- [9] T. Kangwanpongpan F.H.R. Franca R.C. da Silva P.S. Schneider, H.J. Krautz. New correlations for the weighted-sum-of-gray-gases model in oxy-fuel conditions based

on HITEMP 2010 database. *International Journal of Heat and Mass Transfer*, 55: 7419–7433, 2012.

- [10] ANSYS Inc. *ANSYS Fluent Theory Guide v15.0*. November 2013.
- [11] L.C.R. Johansen. RANS Simulation of Oxy-Natural Gas Combustion, Master Thesis, June 2010. Department of Energy Technology, Aalborg University.
- [12] ANSYS Inc. *ANSYS ICEM CFD Help Manual*. January 2015.